DOT/FAA/TC-14/43

Federal Aviation Administration
William J. Hughes Technical Center
Aviation Research Division
Atlantic City International Airport
New Jersey 08405

Development of a Generic Gas Turbine Engine Fan Blade-out Full-Fan Rig Model

August 2015

Final Report

U.S. Department of Transportation
Federal Aviation Administration

NOTICE

This report is available at the Federal Aviation Administration William J. Hughes Technical Center's Full-Text Technical Reports page: actlibrary.tc.faa.gov in Adobe Acrobat portable document format (PDF).

Technical Report Documentation Page

1. Report No.	2. Government Accession No.	3. Recipient's Catalog No.
DOT/FAA/TC-14/43		

4. Title and Subtitle	5. Report Date
DEVELOPMENT OF A GENERIC GAS-TURBINE ENGINE FAN BLADE-OUT FULL-FAN RIG MODEL	August 2015
	6. Performing Organization Code

7. Author(s)	8. Performing Organization Report No.
Kivanc Sengoz, Steve Kan, and Azim Eskandarian	

9. Performing Organization Name and Address	10. Work Unit No. (TRAIS)
The George Washington University FHWA/NHTSA National Crash Analysis Center 45085 University Drive Ashburn, VA 20147 USA	
	11. Contract or Grant No. 11-G-015

12. Sponsoring Agency Name and Address	13. Type of Report and Period Covered
U.S. Department of Transportation Federal Aviation Administration New England Regional Office—Aircraft Certification Service Engine & Propeller Directorate 12 New England Executive Park Burlington, MA 01803	
	14. Sponsoring Agency Code ANE-111

15. Supplementary Notes

The Federal Aviation Administration William J. Hughes Technical Center Aviation Research Division COR was William Emmerling.

16. Abstract

This report describes the development of a generic fan blade-off (FBO) full-fan rig model that could be used to assess modeling approaches for whether the case will contain the fan blade and simulate the initial and post-containment interactions that occur during the three revolutions following blade release. Though the model includes the level of detail necessary to evaluate continued rotation and post-containment interactions between the fully bladed disk and fan case, it does not represent a fully installed engine and, therefore, would not have all the system dynamics characteristics necessary to assess full rundown. The initial containment event includes the initial blade release, release blade contact with the case, and release blade impact with the trail blade. The model uses a hard-mount fan bearing and operates below the first shaft bending critical; therefore, if running with the full fan (all blades represented), the model can assess initial contact (rubs) of the heavy side fan blades with the case, but if running with the counter-balanced three-blade fan, there will be no trail blade tip rubs—they are on the light side of the disk—unless a fragment from the release blade is caught between the blades and case. With the modeling assumptions and simplifications incorporated in this model, it is possible to capture the relevant physics of the fan blade-out event from release through initial and post-containment. The LS-DYNA was used as a nonlinear explicit dynamics finite element code for the simulations. Simulation results were consistent with reported results of actual FBO rig tests.

17. Key Words	18. Distribution Statement
Fan blade-out, Containment, Initial containment, Post-containment, Impact, Finite element analysis, Fan blade fragmentation	This document is available to the U.S. public through the National Technical Information Service (NTIS), Springfield, Virginia 22161. This document is also available from the Federal Aviation Administration William J. Hughes Technical Center at actlibrary.tc.faa.gov.

19. Security Classif. (of this report)	20. Security Classif. (of this page)	21. No. of Pages	22. Price
Unclassified	Unclassified	100	

TABLE OF CONTENTS

LIST OF FIGURES

LIST OF TABLES

LIST OF ACRONYMS

CG	Center of gravity
FAA	Federal Aviation Administration
FBO	Fan blade-off
FE	Finite element
FEA	Finite element analysis
LLNL	Lawrence Livermore National Laboratory
MPP	Massively parallel processing

EXECUTIVE SUMMARY

This report describes the development of a generic fan blade-off (FBO) full-fan rig model that could be used to asses modeling approaches for the initial and post-containment interactions for the three revolutions following blade release. It includes the level of detail necessary to evaluate continued rotation and post-containment interactions between the fully bladed disk and fan case. The initial containment event includes the blade release, initial blade contact with the case, release blade impact with the trail blade, and determination of whether the case will contain the released blade. With the modeling assumptions and simplifications incorporated in this model, it is possible to capture the relevant physics of the FBO event from release through initial and post-containment. LS-DYNA was used as a nonlinear explicit dynamics finite element code for the simulations. Simulation results were consistent with reported results of actual FBO rig tests.

1. INTRODUCTION

In accordance with Federal Aviation Administration (FAA) certification requirements, any new commercial turbofan engine must successfully demonstrate, by engine test, the ability to contain a blade from the stage with the highest blade-release energy. For typical high-bypass turbofan engines, the fan blade is the highest energy blade in the engine. The possibility of an uncontained fan blade during engine operation is a flight safety concern that must be addressed during the design and certification phases of engine development. A typical fan blade-off (FBO) event is very complex, involving nonlinear transient dynamics with large deflection of the release and trailing blades, as well as large nonlinear deflections of the engine structure and progressive failure and fragmentation of some components. A fan blade release event, though rare in service, might be initiated by any number of causes including, but not limited to, material failure following bird strike or foreign object ingestion; fatigue; or manufacturing defect.

The current trend in the aerospace industry is to use analysis where appropriate to reduce test variables, uncertainties, and cost. For FBO testing, the certification agencies may allow demonstration of the containment capability of a derivative engine using a combination of component rig tests and full system analytical simulations when the engine manufacturer has adequate test and analysis experience with the engine family in which the derivative is being developed. At present, there is no well-established, industry-wide standard analytical modeling procedure to simulate events such as FBO; therefore, to pursue the analytical route for a derivative program, each engine manufacturer has to demonstrate to their certification authority their ability to perform such analysis. Currently, the explicit nonlinear transient finite element analysis (FEA) approach has proven to be the most robust of the numerical approaches available for FBO analysis. However, significant research is still required to overcome difficulties with numerical stability, material modeling (pre- and post-failure), and standardizing modeling methods to achieve accurate simulation of the complex interactions between individual components during these high-speed events.

This work was initiated under an FAA research grant aimed at enhancing the safety of civil air travel by reducing the likelihood of a catastrophic accident following an engine blade or rotor failure. The George Washington University National Crash Analysis Center was tasked under an FAA funded program to develop a generic explicit finite element (FE) model for simulating the FBO event for the initial and post-containment interactions for the three revolutions following blade release.

1.1 PURPOSE

The generic gas turbine engine fan blade-out rig model developed in this project is intended to be used to assess modeling approaches for the initial and post-containment events; compare material models; and assess how variations in design details influence containment. The model is useful for analyzing the three revolutions following blade release to assess initial containment (i.e., the initial blade contact with the case, impact with the trail blade, and whether the case will contain the fan blade) and post-containment interactions between the other fan blades and fan case, and the bearings and fan case. It includes sufficient detail to evaluate continued rotation and

post-containment interactions between the other blades and the fan case for the rig, but it is not a full-engine model and does not contain all the hardware necessary to assess full-engine continued rotation and rundown. The model developed in this work will be provided to the LS-DYNA Aerospace Working Group as a test case for validating installation and operation of the code.

1.2 BACKGROUND

Computational modeling of the fan blade-out event for aircraft gas turbine engine fan containment systems is a challenging task involving complex nonlinear transient dynamics with large deflections. In a typical event, the released fan blade impacts the containment case, slides on the inner diameter of the case, and is in turn impacted by the trailing blade. The released blade experiences significant plastic deformation and may fragment. The trailing blade experiences large deformations and may also fragment. The fan containment case experiences large deflections, plastic deformation, and—depending on the specific containment design—may be holed, allowing the released blade to be captured in an external containment wrap. The combination of large deformations, elastoplastic material behavior, progressive material failure, and fragmentation under high strain rates creates a difficult problem requiring advanced modeling methods. Nonlinear transient (explicit) FEA has the greatest potential of any numerical approach available to industry for analysis of these events. Recently, Sinha [1] showed that FE simulation results were consistent with reported results of actual FBO rig tests. A number of researchers [2–5] have created analytical models for the simulation of the FBO event and have identified the important aspects of the numerical simulation. Significant research is still required to overcome difficulties with numerical stability, material modeling (pre- and post-failure), and standardizing modeling methods to achieve accurate simulation of the complex interactions between individual components during these high-speed events.

The fan rig model presented here simulates the type of testing an engine manufacturer might perform to assess initial and post-containment behavior of a new fan or containment case design. Since the rig model uses a fully bladed fan rotor, it fully represents the bladed fan rotor interaction with the containment structure. Therefore, both blade-containment and blade-rubbing events can be studied using the model developed in this work.

The rig model uses solid titanium Ti6-4 fan blades and an aluminum 2024 hardwall containment case. Model geometry and dimensions are representative of a business-jet-size engine and are not intended to represent any specific engine in service or known to be under current development. The objective is to capture typical geometric characteristics consistent with modern engines.

2. MODEL DEVELOPMENT

2.1 MODEL DEVELOPMENT APPROACH

The full-fan rig model development had two phases. In phase 1, a three-bladed fan rig model was developed to study the initial blade-containment event. The primary focus of phase 1 was to develop a model that could be used to assess modeling approaches for the initial containment event, to compare material models, and to assess how variations in design details influence

containment. The three-blade fan and structural isolation of the rotor and case were used to eliminate fan shaft flexibility and structural interaction between the fan shaft and fan case, and to prevent post-release blade tip rubs by the trailing blades. In phase 2, the full-fan rig model was developed by adding the full fan, core case, and associated structure to the three-blade rig model in phase 1, ensuring that there would be full dynamic interaction between the fan and the containment case. The full-fan rig model is useful for evaluation of post-containment interactions between the fan and containment case, as well as system dynamics of the connecting structure.

2.2 PHASE 1 THREE-BLADE MODEL DEVELOPMENT

The fan rig developed for the first phase of the project consisted of a three-blade fan rotor and an isolated hardwall fan case. The Phase 1 model was intended to capture only the initial release and containment phases of an FBO event; there was no secondary contact between the remaining blades and the case, and there were no structural connections between the fan shaft bearings and the fan containment case. The Phase 1 model (three-blade fan rig model) is not a fully bladed fan rotor and it does not fully represent the bladed fan rotor interaction with the containment structure.

Development of the generic three-blade fan rig model was performed in several phases (see figure 1). In the first phase, a fan diameter of 40″ was established. This diameter was used to set a redline maximum operating speed of 7830 rpm. Next, the dynamic characteristics of the bladed fan disk were tuned to ensure that the lower-order bending and torsional modes of the fan blades were representative of reasonable engine characteristics. The ANSYS v11.0 and DYROBES v12.5 FE implicit codes were used to analyze dynamic behavior of the generic fan blade rotor system for rotor critical speeds and modes, and to ensure that the system was operating subcritically prior to the blade release. The initial studies conducted as part of the fan design tuning included:

- Fan blade Campbell diagram, critical speeds and modes (isolated blade)
- Fan rotor Campbell diagram, critical speeds and modes (bladed fan disk)
- Dynamic response of the fan rotor due to mass unbalance excitation without interaction with the containment structure

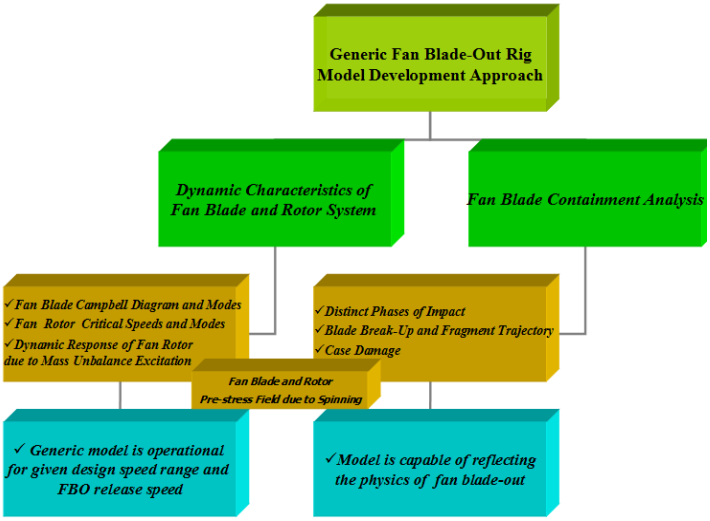

Figure 1. Model Development Approach

To meet the objective of a preliminary design model focusing on blade release; initial fan case contact; trailing blade interaction; blade deformation and fragmentation; and primary containment, the model needed to minimize complications arising from secondary post-release fan-case rub dynamics. To accomplish this, the fan was designed to operate subcritically, the fan case was isolated from the fan shaft supports, and the fan blades were designed with appropriate modal characteristics. A design margin of 10% was placed on the shaft and fan blade first bending modes. Once the model geometry was tuned to achieve the desired modal characteristics, synchronous forced response and transient analyses were conducted to ensure that system dynamics characteristics were appropriate.

When running a rotating model in LS-DYNA, the first task is to initialize rotating component internal stresses to account for centrifugal forces. The ANSYS baseline model was used as the secondary check case to confirm that the LS-DYNA model had been initialized correctly. Any errors in the centrifugal prestressing would affect the accuracy of subsequent FBO model predictions, so it was critical that model initiation be performed correctly. Details for the model development and verification are presented in section 2.4.

The second phase of model development involved verification that the blade release through containment phases of the event are represented accurately. The following aspects of the release event simulation were evaluated to make sure that the generic fan rig model is capable of capturing the physics of a fan blade-out event. Details for this phase of the work are contained in section 3:

- Phases of the blade case interaction
- Blade deformation, breakup, and fragment trajectory
- Case damage

Since the model in phase 1 is not intended to study post-containment fan-case interaction, it was not necessary to include more than three fan blades or the structural connections between the fan support bearings and the fan case. The elimination of the engine core to fan-case structure simplifies the model and helps isolate the post-release fan from the fan case so that studies can focus on the initial containment event. The fan shaft was designed to operate well below its first bending critical speed, which, when combined with stiff bearings, further helps to ensure unintended fan-case interactions are avoided. Since the fan shaft and bearing support responses are not the focus of this work, the ball and roller bearing stiffnesses are assumed to be linear and constant with speed, further simplifying the model.

2.3 PHASE 1—THREE-BLADE FAN RIG MODEL PROPERTIES

The generic three-blade fan rig model represents typical geometry that could be found in a modern high-bypass business-jet-sized engine: 40″ fan diameter, wide chord fan blades, and integral bladed fan disk. Aluminum 2024 was specifically chosen as the fan case material because it has extensive material data available. The fan case includes generic typical engine details, such as redundant engine mounts and stiffening ribs to control shell modes. The redline mechanical rotor speed for the model was set at 7830 rpm, based on fan tip speed. The basic fan rig for this study consists of a three-blade fan rotor and an isolated hardwall fan case. The purpose of this model is to capture the initial release, the released blade impact with the case, sliding of the release blade tip, impact with the trail blade, blade fragmentation, and containment. Model geometry and dimensions are representative of a business-jet-size engine and are not intended to represent any specific engine in service or known to be under current development. The objective is to capture typical geometric characteristics consistent with modern engines.

The rotor shaft developed for this rig is a flexible hollow stainless steel shaft supported on three rolling element bearings. The fan is a one-piece bladed disk design, also known as a blisk or integrally bladed rotor. For the purpose of this rig, only three of the solid titanium wide chord blades are represented and the disk is counter-weighted for balance. Each blade weighs 1.4 pounds, the blade root chord is 4.5″, the tip chord is 5.2″, and the length of the blade leading edge is 14″. Fan blade design details are provided in table 1 and figure 2.

Table 1. Fan Blade Properties

Component	Feature
Weight of one blade	1.4 lb_f
Blade-tip radius	20″
Blade-root radius	6″
Blade-root area	0.9 $in.^2$
Blade-root stagger angle	17^o
Blade-tip stagger angle	40^o
Blade chord at tip	5.2″
Blade chord at root	4.5″
Number of rotorblades	20
Fan blade redline tip speed	1350 ft/sec
Fan redline speed	7830 rpm

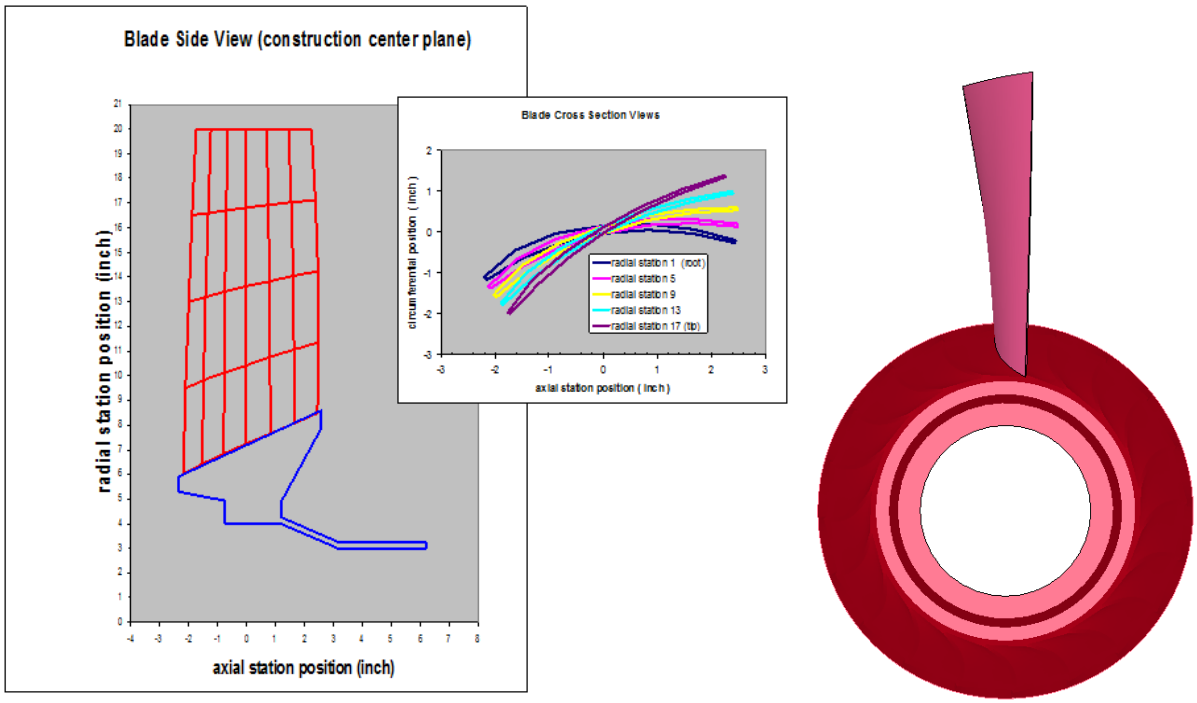

Figure 2. Generic Fan Blade Geometric Details

The fan shaft is 51″ long and has an average wall thickness of 0.2″. Figure 3 shows the shaft supported on one ball and two roller bearings. The ball bearing reacts to thrust and radial loads, whereas the two roller bearings react only to radial loads. The fan rotor shaft does not include any squeeze film dampers. Table 2 lists properties for the fan shaft.

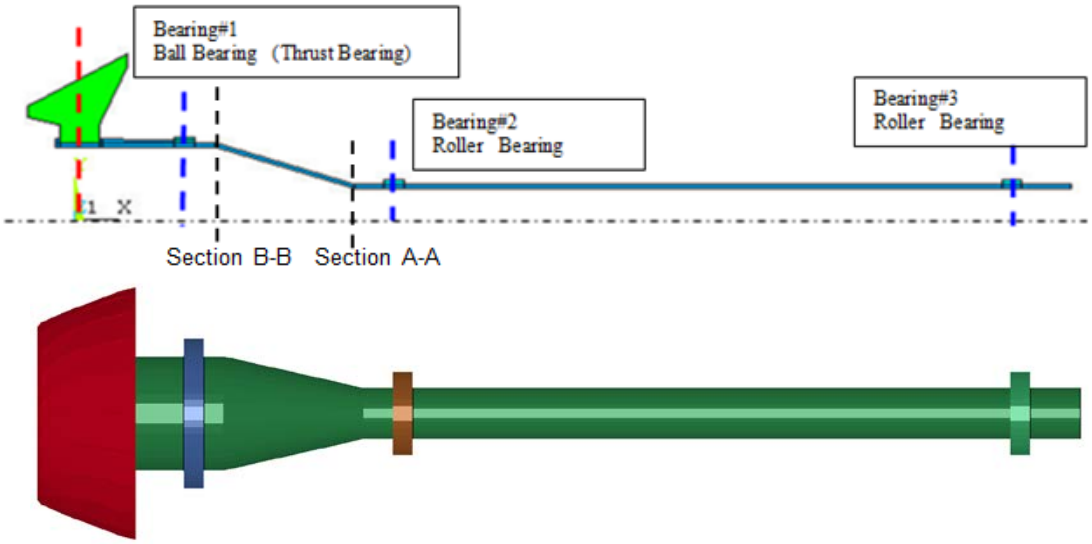

Figure 3. Generic Rotor and Bearing Configuration

Table 2. Fan Shaft Properties

Component	Feature
Shaft length	51"
Shaft inner diameter at section A-A	3.3"
Shaft outer diameter at section A-A	3.7"
Shaft inner diameter at section B-B	7.6"
Shaft inner diameter at section B-B	8.0"
Bearing #1 axial position (ball bearing)	5.5"
Bearing #2 axial position (roller bearing)	16"
Bearing #3 axial position (roller bearing)	47"
Bearing #1 (ball bearing) axial stiffness	6 E+6 lb/in
Bearing #1 (ball bearing) radial stiffness	8 E+6 lb/in
Bearing #2 and #3 (roller bearings) radial stiffness	8 E+6 lb/in
Mass of the disk	0.166 lbm

Since the model is not intended to study post-containment fan-case interaction, it was not necessary to include more than three fan blades or the structural connections between the fan support bearings and the fan case. The elimination of the engine core to fan-case structure simplifies the model and helps isolate the post-release fan from the fan case so that studies can focus on the initial containment event. The fan shaft was designed to operate well below its first bending critical speed, which, when combined with stiff bearings, further helps to ensure unintended fan-case interactions are avoided. Since the fan-shaft and bearing-support responses

are not the focus of this work, the ball and roller-bearing stiffnesses are assumed to be linear and constant with speed, further simplifying the model.

The fan containment case is of hardwall design and is constructed from 2024-T3/T351 aluminum. Circumferential stiffening ribs forward and aft of the fan plane are included to minimize shell modes. Because the fan does not include a full complement of blades, it does not capture the post-containment rubs by the blades opposite the release blade. To further reduce the potential for rotor dynamics to induce interactions, the fan case is not connected to the fan shaft support bearings through intermediate structure. Figure 4 shows geometric details of the hardwall fan case.

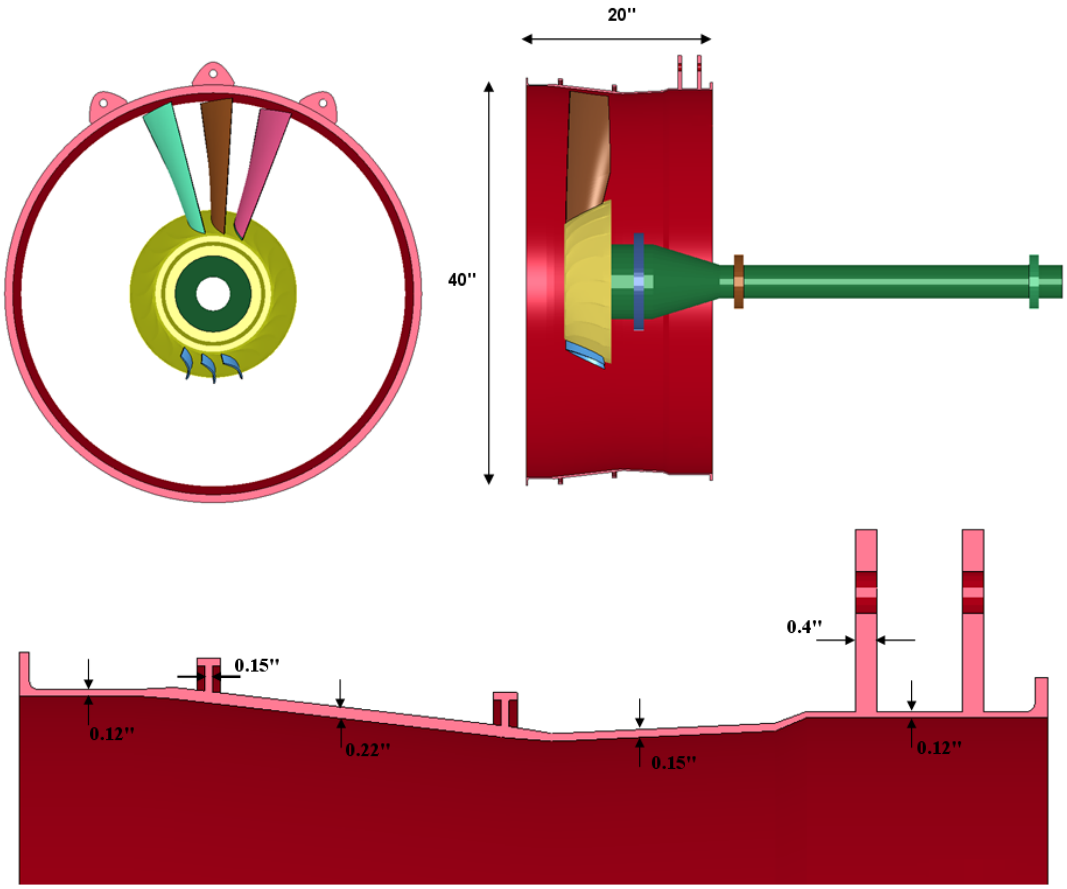

Figure 4. Geometry of the Containment Case

2.4 THREE-BLADE MODEL CHECKOUT BASED ON DYNAMIC CHARACTERISTICS OF THE FAN BLADE AND ROTOR SYSTEM

Model checkout was performed in several phases to confirm the dynamic characteristics of the fan blade and rotor system (see figure 5). In the first phase, the fan blade Campbell diagram was used to identify critical speeds and ensure that the fan exhibited dynamic characteristics consistent with typical wide chord fan engines. The fan-rotor system critical speeds were assessed using both beam models and a 3-D shaft model to ensure that the resulting 3-D

LS-DYNA model was correctly assembled and consistent with intended dynamics characteristics. The baseline beam model was run in the DYROBES and ANSYS Rotordynamics analysis programs to ensure that the baseline against which the LS-DYNA model was developed was accurate. The next step was to analyze the synchronous mass unbalance response of the fan-rotor system to ensure that element loads and deflections were consistent across the baseline and LS-DYNA models. In this study, shaft displacements at the fan and bearing centerlines and bearing forces were compared between analysis programs. Because the baseline comparison included both beam and shell shaft models, care had to be exercised when assessing responses for high-load conditions that could result in 3-D shell deflections not being fully represented in the simpler beam models.

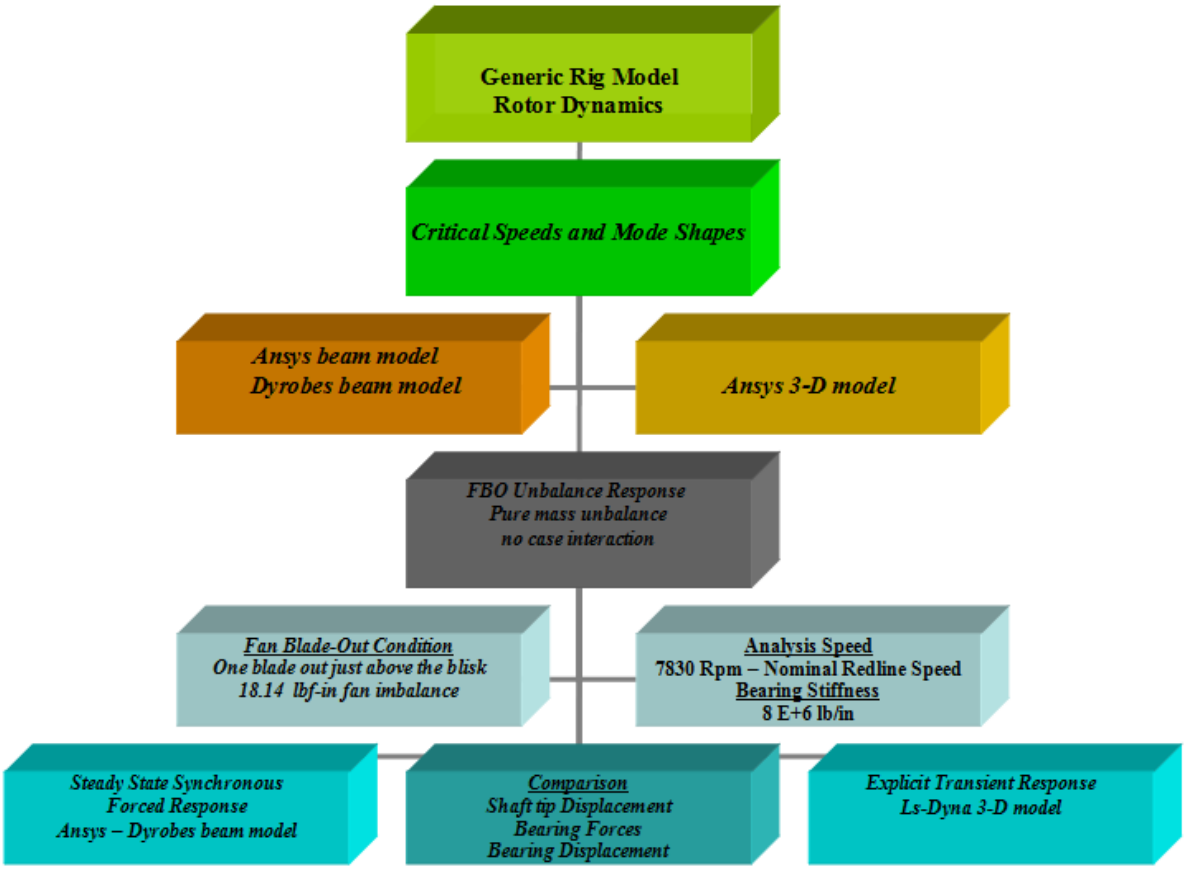

Figure 5. Model Checkout Stages Based on Generic Rig Model Rotor Dynamics

2.4.1 Fan Blade Campbell Diagram—Critical Speeds and Modes

ANSYS was used to perform modal analysis of a single fan blade with centrifugal prestress to develop the data necessary to construct the fan blade Campbell diagram. A preliminary study assessing the use of shells and various numbers of solid elements through the thickness was used to determine the necessary mesh density required to achieve an accurate solution. In the study, acceptable results were achieved when the blade was modeled using 0.1″ in-plane solid elements with four elements through the thickness. The blade root displacements were constrained in all

directions (fixed root). The Campbell diagram was used to identify critical speeds and ensure that the fan exhibited dynamic characteristics consistent with typical wide chord fan designs. For illustration purposes, the modal analysis results for the first three modes at redline are shown in figure 6. The first bending mode occurs at 171 Hz, the first torsion at 305 Hz, and the second bending at 603 Hz. Figure 7 shows that the first bending has adequate margin on first-order excitation and the other modes exhibit Campbell crossings consistent with industry design practices. Table 3 shows fan blade frequencies for selected points on the Campbell diagram.

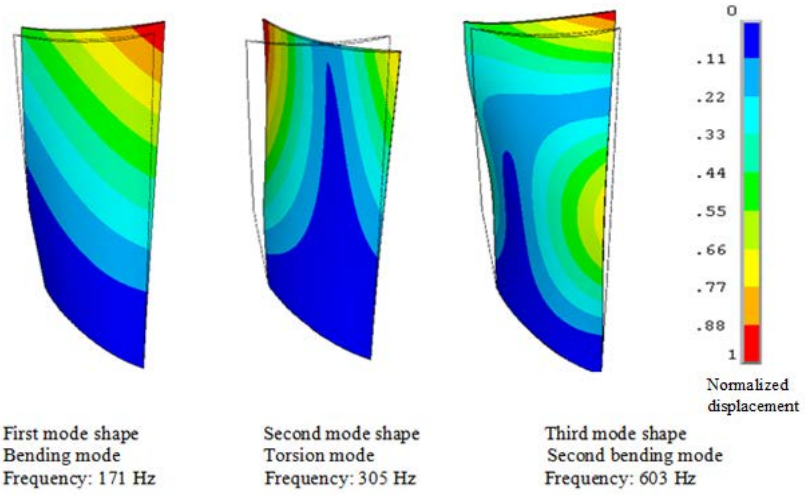

Figure 6. Mode Shapes and Natural Frequencies at Redline Speed, 7830 RPM

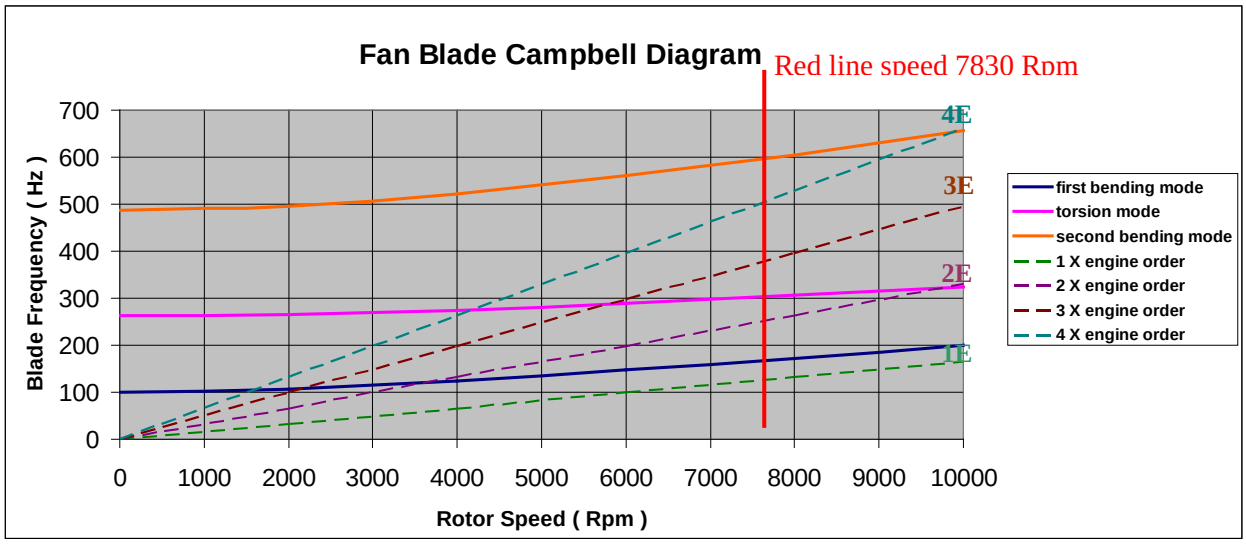

Figure 7. Fan Blade Campbell Diagram

Table 3. Fan Blade Frequencies for Campbell Diagram

Speed (RPM)	0	2000	4000	6000	Redline Speed 7830	8000	10,000
First Bending Mode (Hz)	101	107	124	147	171	172	196
Torsion Mode (Hz)	262	265	275	289	305	292	324
Second Bending Mode (Hz)	487	495	521	560	603	604	657

Fan rotation induces centrifugal forces that prestress the rotor and fan blades, and in turn modify the fundamental blade frequencies and mode shapes as a function of rotor speed. The centrifugal prestresses were calculated using the implicit solver for 3-D models. Fan blade stress and deflection validation runs were performed at redline speed by comparing the ANSYS and LS-DYNA solutions for the centrifugal prestress fields (see figures 8 and 9). The geometric nonlinear implicit static analysis with centrifugal body load option was used to compare both validation cases. The calculated prestresses using the LS-DYNA implicit solver were used to generate the initial state, and the initial velocity field was imposed at each node of the rotor, including the released blade for the 3-D LS-DYNA model.

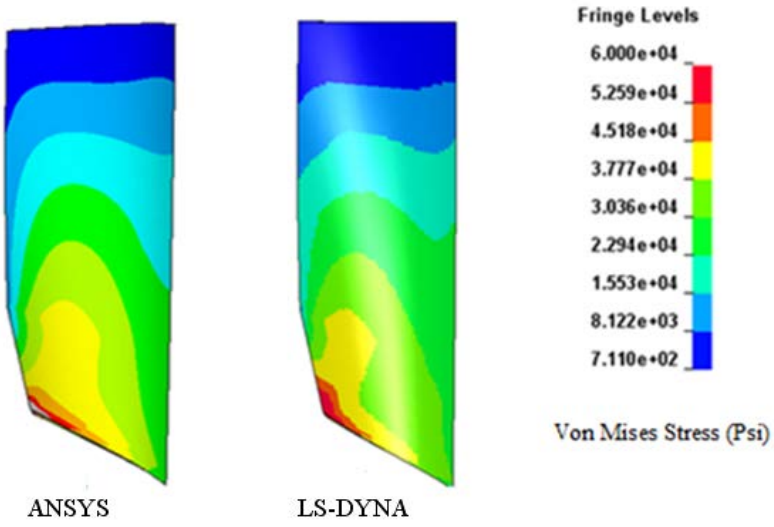

Figure 8. Fan Blade Prestress Field With ANSYS and LS-DYNA Implicit Solver

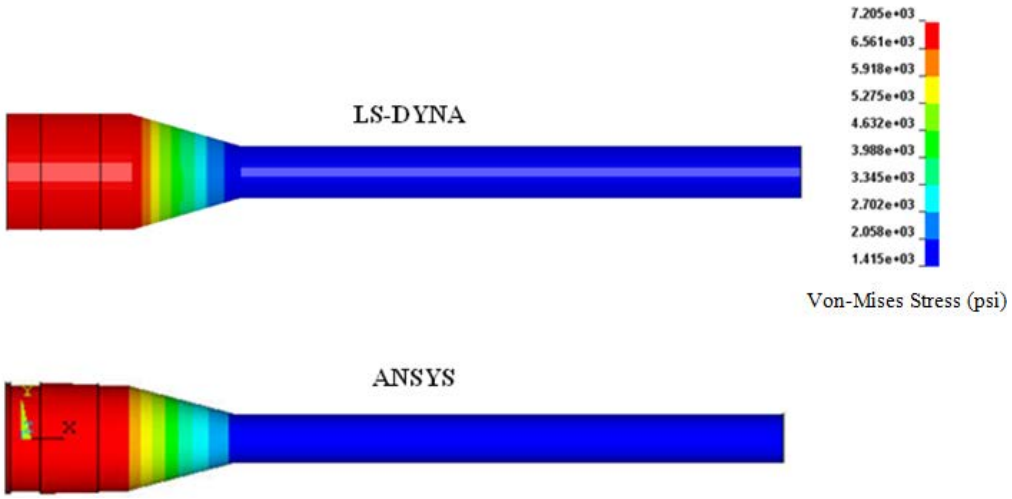

Figure 9. Rotor Shaft Prestress Field With LS-DYNA and ANSYS Implicit Solvers

2.4.2 Fan Shaft Campbell Diagram—Critical Speeds and Modes

The fan shaft Campbell diagram and critical speeds are generated using the ANSYS Rotordynamics module and DYROBES software. To ensure that an accurate consistent model was developed, the following models are compared for critical speeds and mode shapes:

- ANSYS beam model
- DYROBES beam model
- ANSYS 3-D model

The QR damp eigensolver with complex eigenvalue solutions was used in the ANSYS Rotordynamics module to generate data for the fan shaft Campbell diagram. Total mass and inertia of the blisk was modeled using mass elements with the rotary inertia option (rigid bladed disk). Bearings were modeled with COMBI214 2-D spring-damper bearing elements for which the first node was connected to the shaft and the second node was grounded (the grounded node displacements were constrained to zero in all degrees of freedom).

For the 3-D rotor model, the shaft and disk were modeled explicitly and sets of dummy elements were used to represent the total blade mass and inertia attached to the disk. The bearings were modeled using classic spring elements. The first node of the spring elements was placed at the center of the bearings and linked to the bearing surface nodes using multipoint constraint elements. The second node of the spring element was grounded (displacements are constrained in all degrees of freedom). Four elements were used through the thickness of the shaft to capture the correct bending stiffness of the shaft. Figure 10 shows the Campbell diagram obtained in the ANSYS Rotordynamics beam model. Table 4 shows fan shaft system frequencies for the beam model.

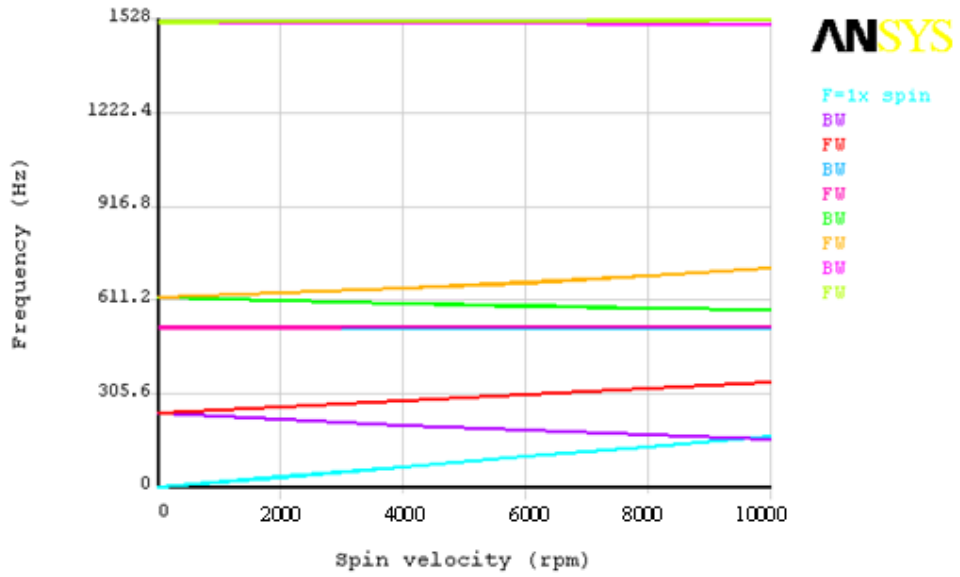

Figure 10. Fan Shaft System Campbell Diagram

Table 4. Fan Shaft System Frequencies

Spin (Rpm)	0	2000	4000	6000	7830	8000	10,000
1 x Spin (Hz)	0	33	66	100	130.5	133	166
1 BW (Hz)	241	221	203	186	173	171	157
1 FW	241	261	282	302	320	322	342
2 BW	521	521	520	520	519	519.5	519
2 FW	521	522	523	523.5	524	524	525
3 BW	620	609	600	592	586	585	579
3 FW	620	634	649	668	687	690	715
4 BW	1519	1518	1517	1525	1514	1514.5	1513
4 FW	1519	1521	1522	1524	1525	1525.5	1526

FW = forward whirl mode; BW = backward whirl mode

Comparisons between DYROBES and ANSYS show good correlation in terms of critical speeds and mode shapes of the fan shaft system (see figure 11 and table 5). Differences are a function of the assumptions for shear flexibility and beam versus shell modeling, and are within expected tolerances for the modeling methods used. The model was predicted to have greater than 10% margin on the first critical speed throughout the operating speed range. This ensures that the rotor will operate well below its first bending critical speed and minimize undesired rotor dynamics characteristics during FBO simulations.

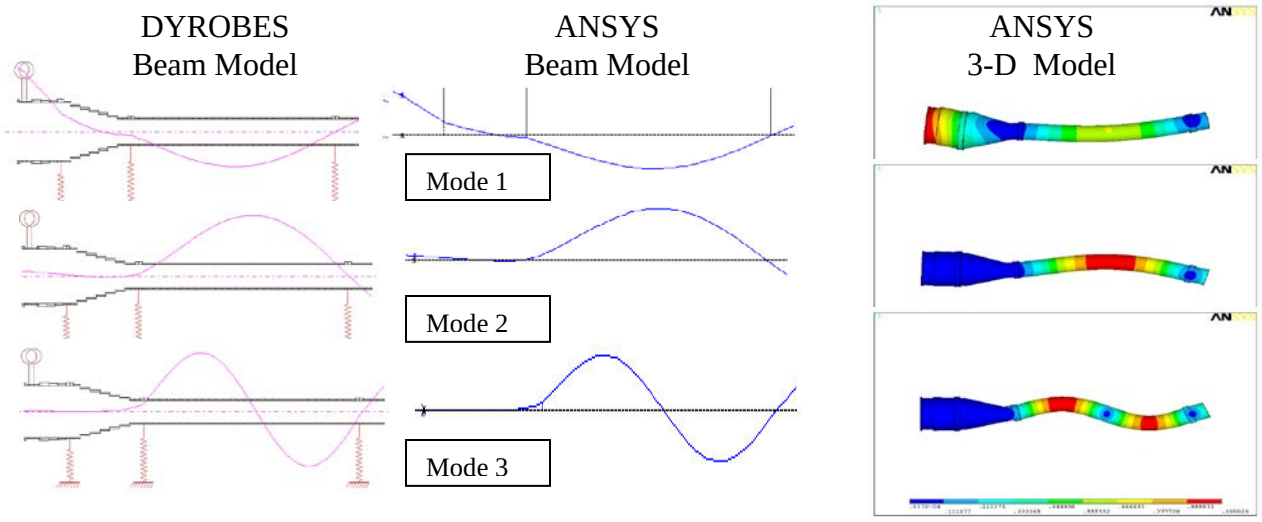

Figure 11. Critical Speed Mode Shapes of the Fan Shaft System

Table 5. Fan Shaft System Critical Speeds

	DYROBES (beam)	ANSYS (beam)	ANSYS 3-D
Mode 1	442 Hz	437 Hz	433 Hz
Mode 2	518 Hz	507 Hz	495 Hz
Mode 3	1532 Hz	1496 Hz	1498 Hz

2.4.3 Dynamic Response of the Fan Shaft System Due to Mass Unbalance Excitation Without Interaction With the Containment Structure

Synchronous forced response checkout cases were run by comparing LS-DYNA, ANSYS, and DYROBES results for the dynamic response of the fan-shaft system supported on grounded bearings. Because there is no structural connection between the bearings and the fan case, and because this analysis did not include fan rubs, the containment structure was not included. Displacements of the fan shaft at the fan centerline and bearings, as well as bearing forces, were compared for three models excited by mass imbalance. The responses for the three models compared well for all cases. Next, transient analyses were compared, and it was shown that the LS-DYNA 3-D solid model transient explicit analysis gave similar results to the implicit beam model results from DYROBES and ANSYS. The models also predicted similar bearing responses, thus assuring that the dynamic response model should be ready for fan blade-out studies. The unbalance excitation used for the correlation was 18.14 lbf-in., corresponding to the loss of one blade just above the blisk. The radial stiffness used for all bearings was 8 million pounds per inch. The analysis was conducted at the nominal redline speed of 7830 rpm, and no blade-case interaction was considered.

2.4.3.1 Steady State Synchronous Unbalance Response Due to Mass Unbalance Excitation Using ANSYS and DYROBES

Synchronous unbalance response analysis cases were also run using ANSYS and DYROBES beam models. The unbalance force (eccentric mass x offset radius x rotational speed [rad/sec] squared) was applied to the shaft beam model at the node where blade center of gravity (CG) would have been located. Linear spring elements were used to simulate bearing stiffness. The first node of the spring was connected to the shaft and the second node was grounded (ground side displacements were constrained in all degrees of freedom). System responses were compared at the nominal redline speed of 7830 rpm. Figures 12 and 13 show imbalance response orbits for the ANSYS and DYROBES models.

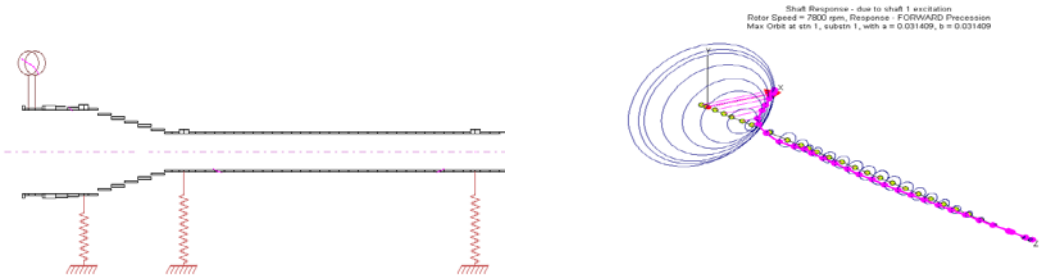

Figure 12. Imbalance Orbit of the DYROBES Beam Model

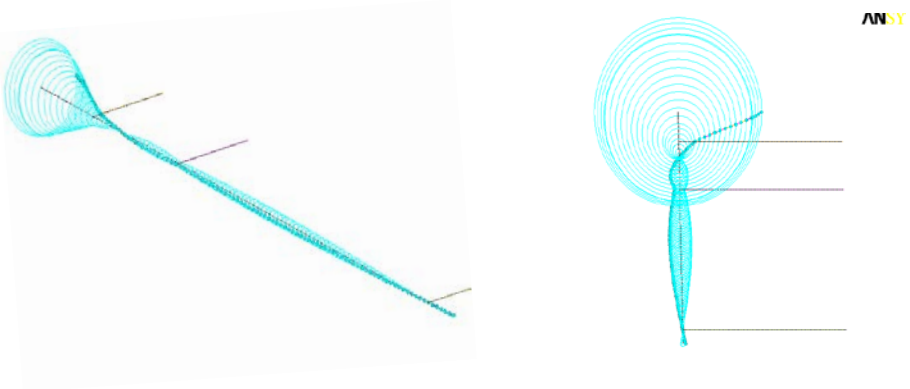

Figure 13. Imbalance Orbit of the ANSYS Rotordynamics Beam Model (isometric and plan view)

2.4.3.2 Explicit Transient Response Due to Mass Unbalance Excitation Using LS-DYNA

In the LS-DYNA explicit transient model, the 18.14 lbf-in. fan imbalance was created by the release of a single blade. In this model, the released blade was disconnected from the disk at 1.1 ms. The model was run at the nominal redline speed of 7830 rpm. Bearing 1, the ball bearing, was modeled with a spherical joint; bearings 2 and 3, the roller bearings, were modeled with cylindrical joints. Bearing stiffness was modeled with the joint stiffness card in LS-DYNA.

No damping was applied to the bearings. Figure 14 shows the LS-DYNA model. Transient displacement response of shaft tip and three bearings was obtained for the first three rotation cycles (see figures 15 and 16). The transient response oscillates during the first cycle because of the effect of the sudden imbalance application (step function) and then settles down during the second cycle, eventually setting on the classic harmonic unbalance response for the rest of the analysis. Figure 17 shows the orbit of the fan disk center during this transient. The dashed line depicts the orbit during the first cycle. The solid line depicts the second and third cycles.

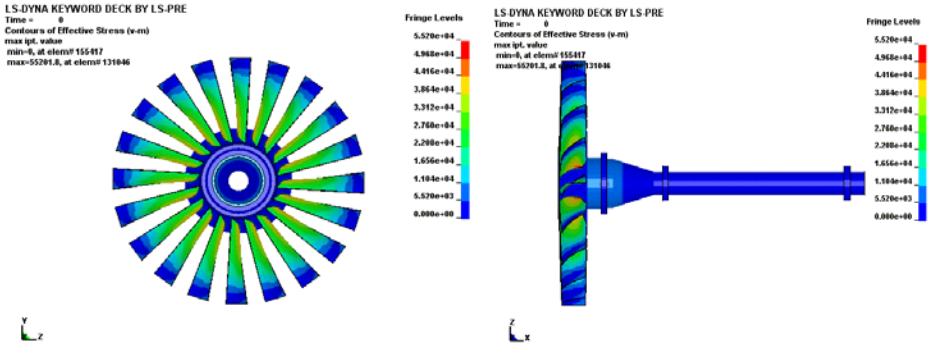

Figure 14. Imbalance Analysis of the Fan Rotorblade System in LS–DYNA

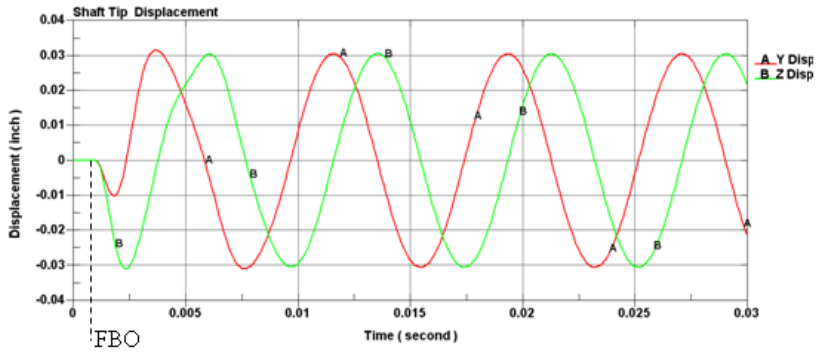

Figure 15. Shaft Centerline Displacement Due to Imbalanced Load

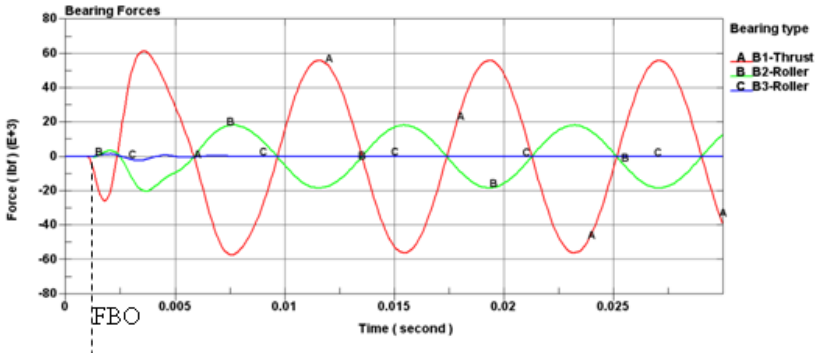

Figure 16. Bearing Forces Due to Imbalanced Load

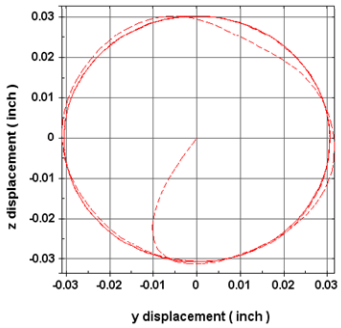

Figure 17. Disk Center Orbit Due to Imbalanced Load

Displacements at the fan and bearing centerlines, as well as bearing forces, are compared for all three models and shown to agree well for the three cases (tables 6–8). It was also shown that the 3-D transient explicit fan blade-rotor model in LS-DYNA predicts similar displacement and bearing force results to the implicit model.

Table 6. Fan–Rotor System Displacement Response Under Imbalance Load

Location	DYROBES-beam	ANSYS-beam	LS-DYNA 3-D
Fan centerline displacement (inch)	0.0314	0.0308	0.0324
Bearing 1 displacement (inch)	0.0066	0.0065	0.0068
Bearing 2 displacement (inch)	0.0020	0.0020	0.0021

Table 7. Fan–Rotor System Normalized Displacement Response Under Imbalance Load

Location	Normalize Each Case to Bearing 1 Displacements		
	DYROBES-beam	ANSYS-beam	LS-DYNA 3D
Fan centerline displacement	477%	476%	476%
Bearing 1 displacement	100%	100%	100%
Bearing 2 displacement	30%	30%	30%

Table 8. Bearing Forces Under Imbalance Load

	Force (DYROBES-beam)	Force (ANSYS-beam)	Force (LS-DYNA 3-D)
Bearing 1	52,600 lb	52,014 lb	55,000 lb
Bearing 2	16,100 lb	15,913 lb	18,100 lb
Bearing 3	134 lb	173 lb	142 lb

2.5 PHASE 2 FULL-FAN RIG MODEL DEVELOPMENT APPROACH

The full-fan rig model developed in phase 2 is a continuation of modeling work from phase 1 and includes a fully bladed (20 fan blades) fan rotor and hardwall fan case having structural connections between the fan shaft bearings and fan containment case, a core case, and strut connection to ground. The model is a fully coupled rotor-core case-fan frame-strut model. Four fan struts connect the fan case to the core case; the core case supports the bearings in which the fan shaft rotates and the strut takes rig reaction loads to ground, therefore providing a good representation of the initial fan/case response during an FBO event.

Figures 18 and 19, and table 9, show the components that were added to the phase 1 model for phase 2.

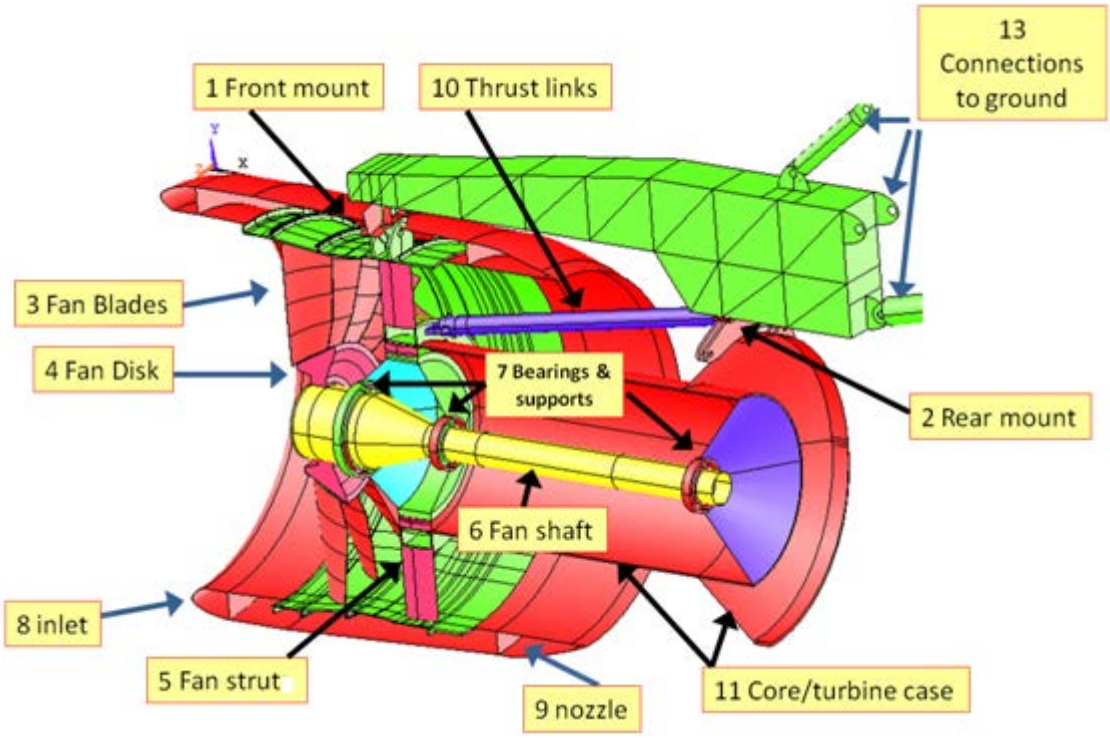

Figure 18. Components of Full-Fan Rig Model

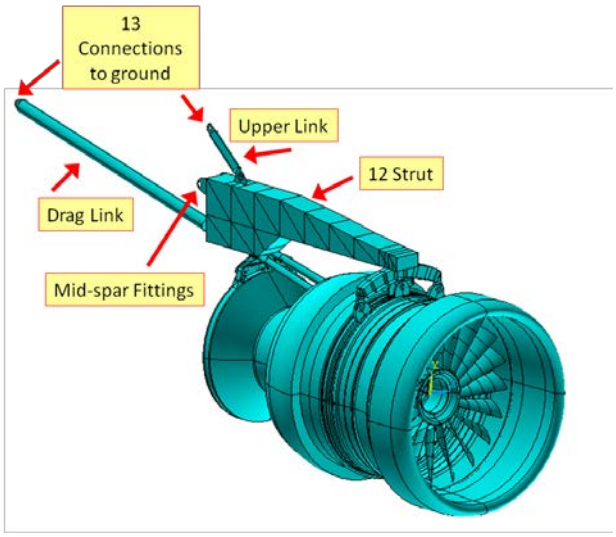

Figure 19. Ground Connections and Links of Rig Model

Table 9. Properties of Full-Fan Rig Model Components

Component Number	Full-fan Rig Model Components	Thickness	Material
1	Front mount	0.3″	Ti-64
2	Rear mount	0.5″	Inconel 718
3	Fan blades		Ti-64
4	Fan disk		Ti-64
5	Fan strut	0.15″	
6	Fan shaft		SS-304
7	Bearing support 1&2	0.25″	Ti-64
7	Bearing support 3	0.25″	SS-304
8	Fan inlet	0.3″	Al-2024
9	Fan nozzle	0.3″	Al-2024
10	Thrust links	0.25″	SS-304
11	Core case	0.25″	SS-304
12	Wing strut skin	0.1″	Al-2024
	Wing strut ribs	0.15″	Al-2024
	Wing strut fittings	0.4″	Al-2024
13	Connections to ground		
	Upper link	0.2″	SS-304
	Drag link	0.2″	SS-304
	Mid-Spar fittings	0.4″	Al-2024

SS = stainless steel

The inlet; nozzle; fan frame; front and rear mount; core turbine case; bearing supports; thrust links; upper link; drag link; mid-spar fittings; wing strut; and 20 fan blades added in phase 2 were developed and included in several subphases. In the first subphase, geometric properties of phase 2 components were established. Model geometry and dimensions are representative of a business-jet-size engine and are not intended to represent any specific engine in service or known to be under current development.

The objective was to capture typical geometric characteristics consistent with modern engines. Front- and aft-mount geometry was tuned to achieve system natural frequencies and mode shapes representative of a full-fan rig model. Natural frequency and specific mode shapes corresponding to local deformation of front and aft mount establish a reference regarding the stiffness of these mounts; therefore, final geometric properties of these mounts were determined based on the stiffness response. Next, the static displacement of the full-fan rig model was checked out by running 1g static load cases in vertical, lateral, and axial directions. These runs provided information regarding the static stiffness of the full system in vertical, lateral, and axial

directions. Additionally, 1000-lb static load cases on A-flange and fan centerline were run to evaluate the linear static stiffness and deformation behavior of the system. The ANSYS v11.0 implicit FE software was used to analyze the dynamic behavior of the FBO full-fan rig model for rotor natural frequencies and mode shapes through operating range. Model geometric properties were tuned to ensure that the first six rig rigid body modes were representative of engine characteristics (taking into account that many engine details are not included in a rig). The initial studies conducted as part of the design-tuning included:

- Static analysis of the FBO full-fan rig model: providing directional displacement behavior of the full system to unit g loading excitation in the vertical, lateral, and axial directions.
- Modal analysis of the FBO full-fan rig model: providing natural frequencies and corresponding mode shapes through the operating range of the system.

2.6 PHASE 2 FULL-FAN RIG MODEL PROPERTIES

The generic rig model represents typical geometry that could be found in the fan module of a modern high-bypass business-jet-sized engine: 40″ fan diameter, wide chord fan blades, integral bladed fan disk, and an aluminum 2024 hardwall fan case. Aluminum 2024 was specifically chosen as a fan case material because of the extensive data available for this material. The fan case includes generic details, such as redundant engine mounts and stiffening ribs to control shell modes. The redline mechanical rotor speed for the model was set at 7830 rpm, based on fan tip speed. The full-fan rig for this study consists of 20 blades, a fan rotor, and a hardwall fan case. The purpose of this model is to capture the pre- and post-containment events of typical FBO events. These events are initial release, release blade impact with the case, sliding of the release blade tip, impact with the trail blade, blade fragmentation, containment as a part of blade containment analysis, blade tip rubbing, and fan rotor orbiting because of a rotating unbalance vector as a part of the transient dynamic response of the fan rotor analysis. Model geometry and dimensions are representative of a business-jet-size engine and are not intended to represent any specific engine in service or known to be under current development. The objective is to capture typical geometric characteristics consistent with modern engines. Figure 20 shows the main dimensions of the full-fan rig core and struts. Figure 21 shows the inlet and nozzle.

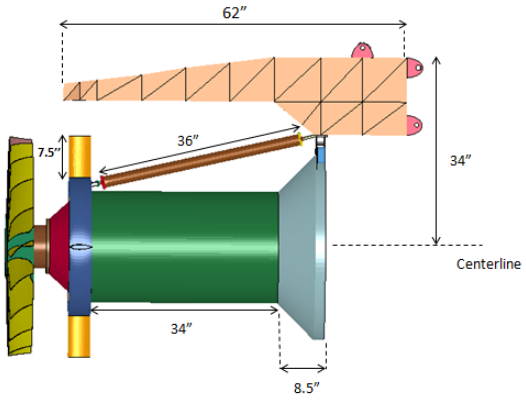

Figure 20. Major Dimensions for the Full-Fan Rig Core and Strut Models

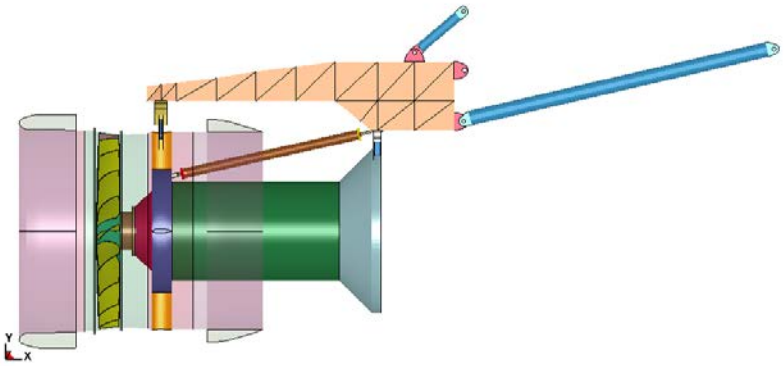

Figure 21. Side View, Full-Fan Rig Model With Inlet and Nozzle

The rotor shaft developed for this rig is a flexible, hollow, stainless steel shaft supported on three rolling element bearings. The fan is a one-piece bladed disk design, also known as a blisk or integrally bladed rotor. For the current phase 2 rig model, 20 solid titanium wide chord blades are represented. Each blade weighs 1.4 lb, the blade root chord is 4.5″, the tip chord is 5.2″, and the length of the blade leading edge is 14″. Table 1 and figure 2 show the fan blade design details.

The fan case is connected to the core case and the fan-shaft support bearings through the fan frame (see figures 22 and 23). The fan frame consists of four hollow airfoil-shaped struts connected at their inner radius to the core case.

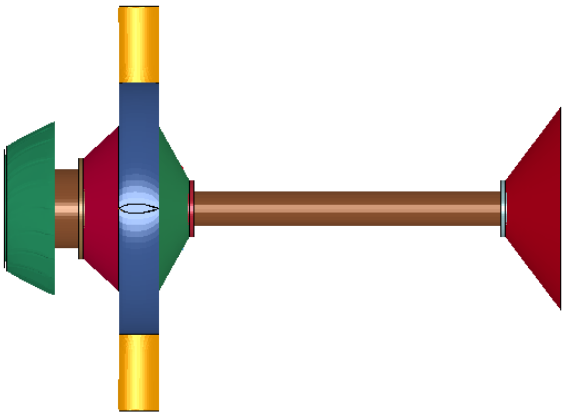

Figure 22. Fan Struts, Fan Strut Core Base, Bearing Supports, and Fan Shaft Side View

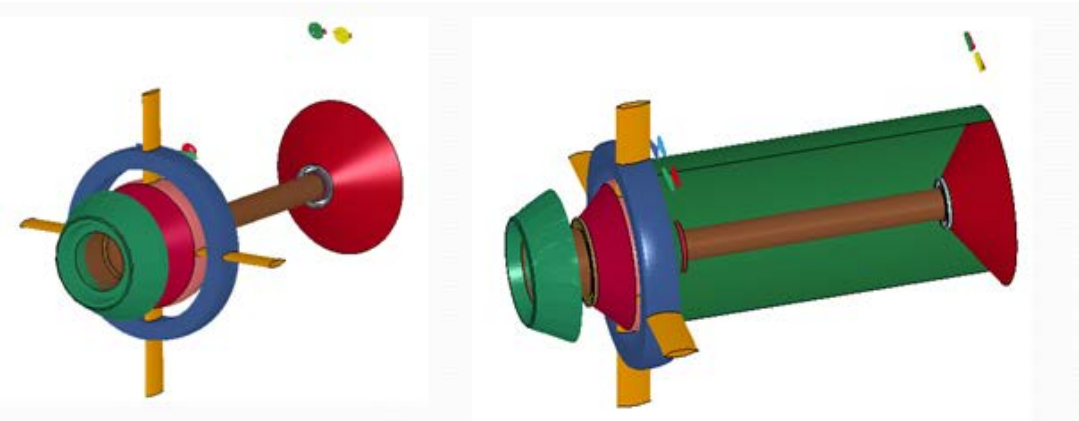

Figure 23. Fan Frame Struts, Core Case, Bearing Supports, and Fan Shaft Isometric View

The fan containment case is of hardwall design and is constructed from 2024-T3/T351 aluminum. Circumferential stiffening ribs forward and aft of the fan plane are included to minimize shell modes. The fan includes a full complement of blades and the fan case is connected to the fan shaft support bearings through intermediate structure to be able to simulate system-dynamics-induced interactions so it can capture the post-containment rubs on the blades opposite the release blade. Figure 24 shows geometric details of the hardwall fan case.

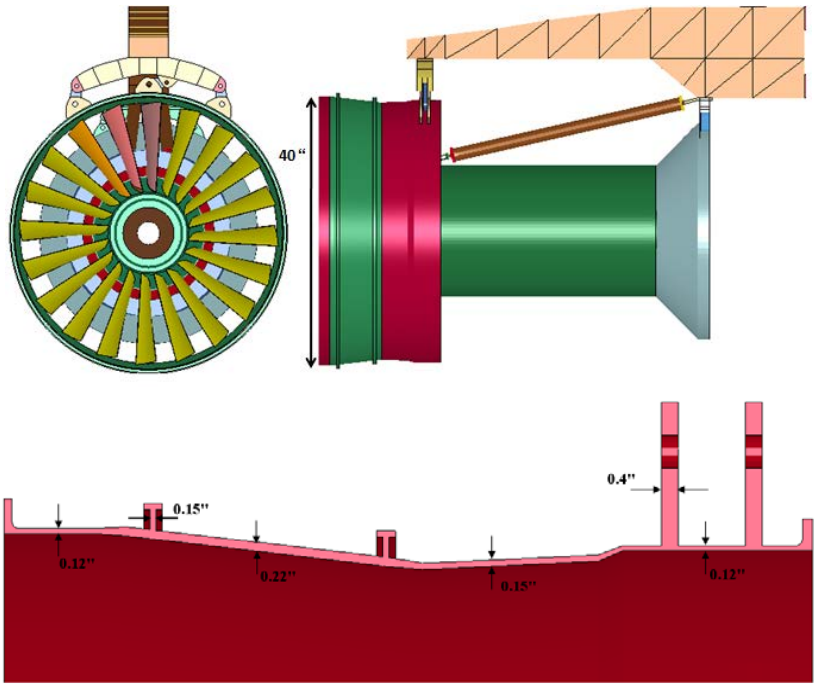

Figure 24. Geometric Details of the Containment Case

A gas turbine engine may be mounted at various points on an aircraft, such as on a strut under a wing or on a pylon integrated with the empennage (aft) aircraft structure. In this model, a strut representative of a wing-mounted engine is used. The engine mounting configuration ensures the transmission of loads between the engine and aircraft structure. The loads typically include the weight of the engine, thrust, aerodynamic loads, and rotary torque about the engine axis. The engine mounting configuration modeled includes a wing strut having a forward mount and an aft mount with two stainless steel thrust links, which extend forward from the aft mount to the engine core case structure (see figure 25). The front mount is basically an I-beam stiffened with ribs and carries a pair of laterally spaced links. At the outer ends of the mount, each link extends outwardly in opposite lateral directions relative to the engine longitudinal axis (see figure 26(a)). The front mount is connected to the engine containment case through these links. The rear engine mounts include a rear mount member, which is an arc-shaped element that carries a pair of laterally spaced links. The links each extend outwardly in opposite lateral directions relative to the engine longitudinal axis (see figure 26(b)). Both front mount and aft mount also have a third link at the center, which is a fail-safe link that provides backup in the case of failure of one of the lateral links.

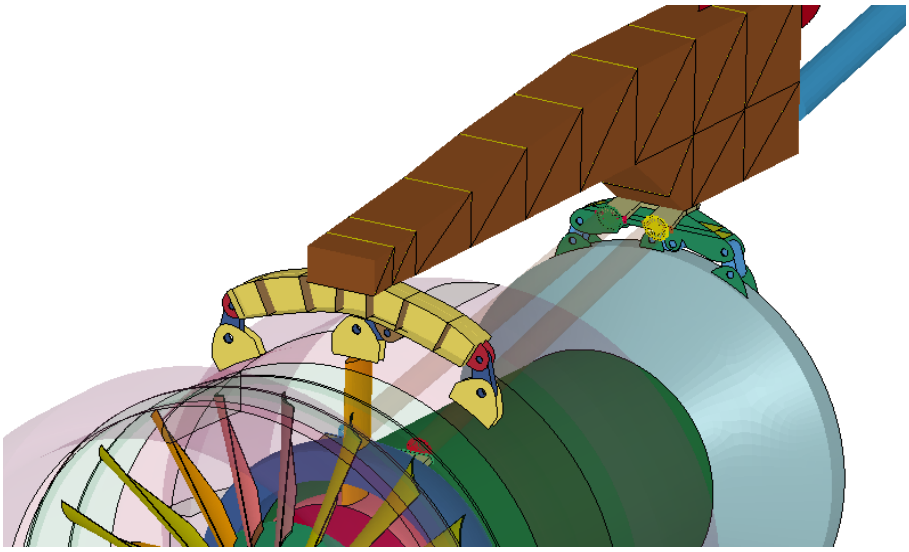

Figure 25. Front and Aft Mount Isometric View

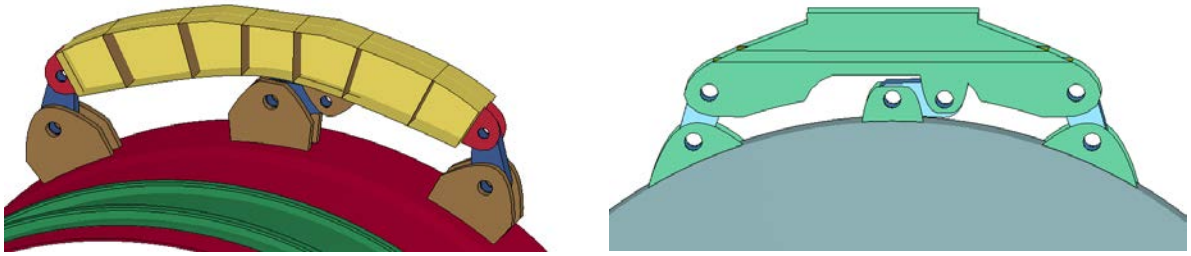

(a) (b)

Figure 26. Closeup View of the (a) Front Mount and (b) Aft Mount

The strut model is attached to the wing at three points: the drag-link lug, the upper-link lugs, and the mid-spar fitting lugs (see figure 27). The wing itself has not been modeled and is assumed to have infinite stiffness. Therefore, these three attachment points can be thought of as the ground connection points for the rig model.

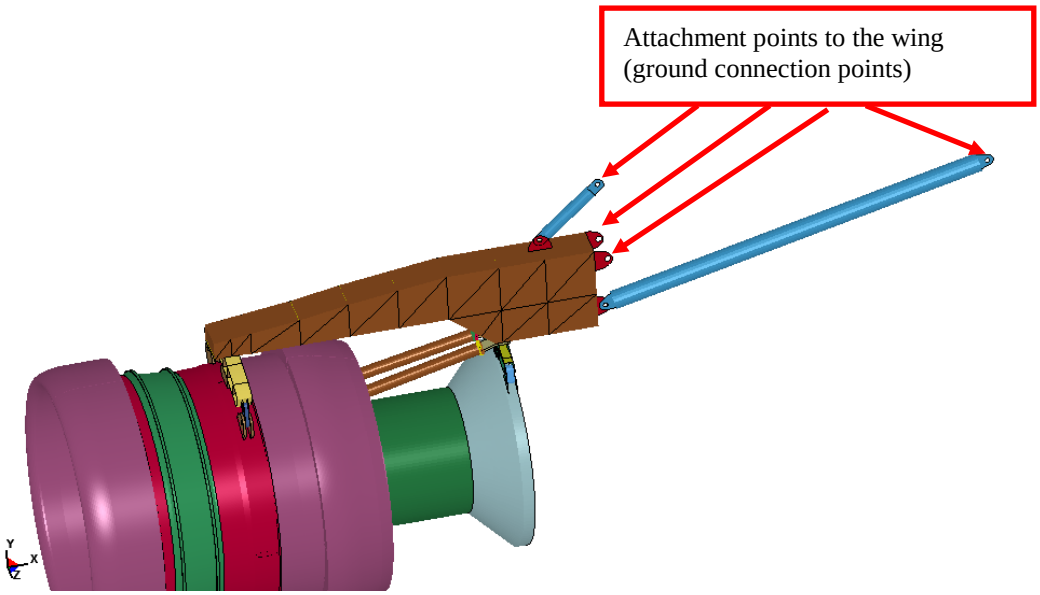

Figure 27. Wing Strut Attachment Points

2.7 MODEL CHECKOUT BASED ON STATIC ANALYSIS OF THE FBO FULL-FAN RIG MODEL

Static load cases have been run using ANSYS v11.0 FE implicit code to ensure component connections are correct load paths and system weights are validated using reaction force checks. The following static load cases have been run:

- Vertical 1 g loading
- Lateral 1 g loading
- Axial 1 g loading
- Vertical 1000-lb load on A-flange
- Lateral 1000-lb load on A-flange
- Vertical 1000-lb load at fan disk centerline
- Lateral 1000-lb load at fan disk centerline

Figure 28 shows geometry for the full-fan rig model as created in ANSYS. In the ANSYS model, the containment case was modeled using shell elements with a mesh size that is relatively coarse compared to what is typically used in LS-DYNA transient impact dynamics models (see figure 29). Though the mesh is not fine enough for impact modeling, it is more than sufficient for static and modal analysis, therefore saving CPU time without compromising the accuracy for this analysis. In LS-DYNA, a finer mesh containment case model is used for penetration and impact dynamics simulation. The fan disk and blades were modeled using 3-D eight-node structural solid-element type SOLID185 with enhanced strain option to prevent shear locking in bending-dominated problems. All other components have been modeled using shell element type SHELL181 with the bending and membrane stiffness option turned on. SHELL181 is suitable for analyzing thin to moderately thick shell structures. It is a four-node element with 6 degrees

of freedom at each node: translations in the x, y, and z directions, and rotations about the x, y, and z axes. Pinned boundary conditions are applied at the ground connection points of the model (see figure 29). This condition constrains only the displacement degree of freedom of the lug central node in the x, y and z directions and allows rotation about the x, y, and z degree of freedom of the node.

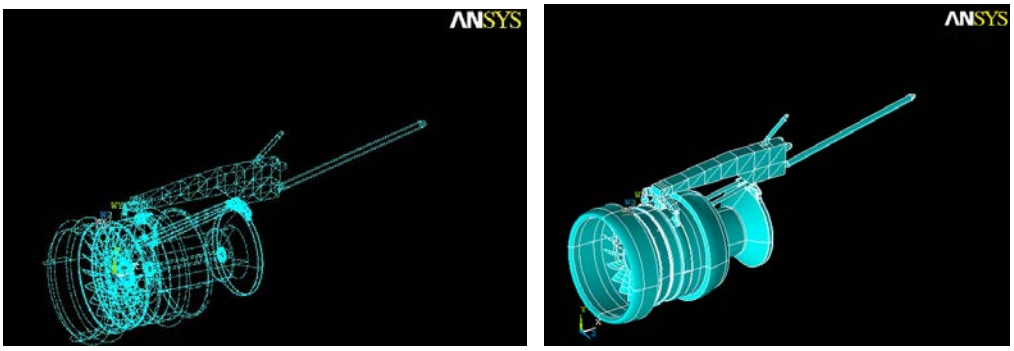

Figure 28. The ANSYS CAD Data of the Full-Fan Rig Model

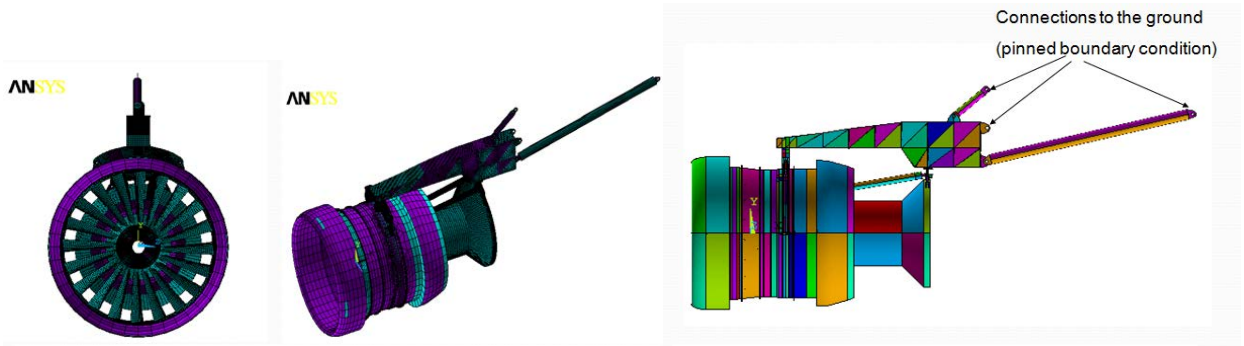

(a) (b)

Figure 29. The (a) Mesh and (b) Boundary Conditions for the FBO Full-Fan Rig Model in ANSYS

2.7.1 Static Analysis Load Case 1: 1 g Loading in Vertical, Lateral, and Axial Directions

Reaction forces at the grounded nodes were used to check system weight. Table 11 shows the rig reaction loads resulting from a 1 g vertical loading case. The total system weight is equal to the sum of the vertical (y direction) reaction forces *Ry*. Since the model CG is offset relative to the centroid of the reaction points, the sum of axial and lateral reaction forces does not equal zero, but is a function of the resulting reaction moment. Maximum vertical displacement under 1 g vertical loading is -0.54″ at the tip of the inlet (see figure 30). Table 10 shows connection link forces, and table 11 shows reaction forces.

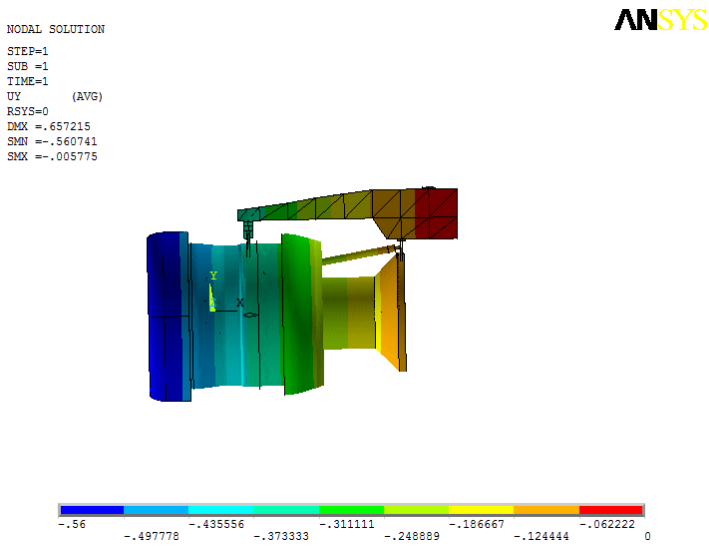

Figure 30. Vertical Displacement (inches) of the FBO Full-Fan Rig Model Under 1g Vertical Loading

Table 10. Connection Link Axial Forces—1g Vertical Loading

Connection Link Axial Forces	Faxial (lbf)
Forward mount link force	374
Aft mount link force	69
Drag link force	-2868
Upper link force	1659

Table 11. Reaction Forces—1g Vertical Loading

Grounded Reaction Forces	*Rx*(lbf)	*Ry*(lbf)	*Rz*(lbf)
Upper link grounded node	1442	1237	0
Drag link grounded node	-2591	-580	-6
Mid-spar fitting 1 grounded node	601	204	1.22
Mid-spar fitting 2 grounded node	601	204	1.22
Total reaction force	53	1065	-3.56

For the axial 1 g loading case, the maximum longitudinal displacement is at the lower side of the containment casing and the magnitude of the maximum displacement is 0.28″ (see figure 31). Connection link axial forces and reaction forces at grounded points corresponding to axial 1g loading are shown in tables 12 and 13, respectively.

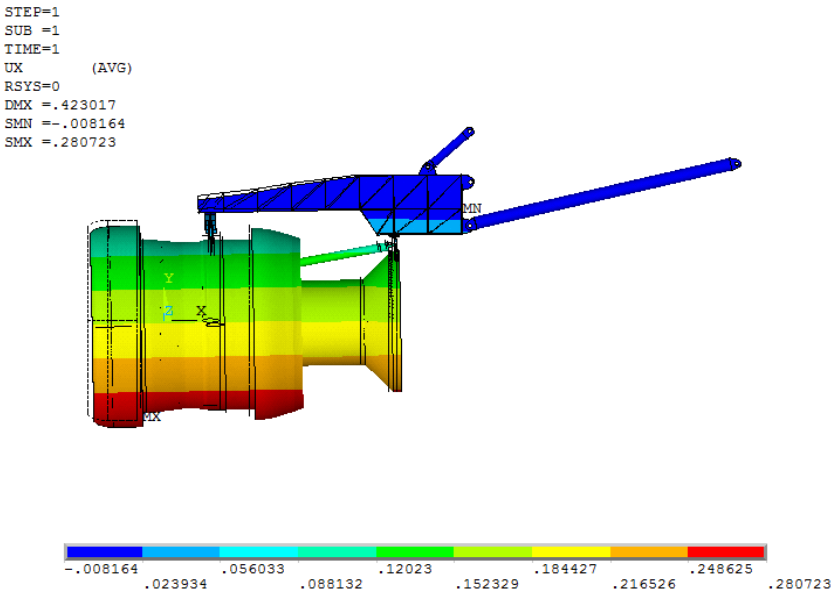

Figure 31. Longitudinal Displacement (inch) of the FBO Full-Fan Rig Model Under 1g Axial Loading

Table 12. Connection Link Axial Forces—1g Axial Loading

Connection Link Axial Forces	Faxial (lbf)
Drag link force	-1703
Upper link force	979

Table 13. Reaction Forces—1g Axial Loading

Grounded Reaction Forces	*Rx*(lbf)	*Ry*(lbf)	*Rz*(lbf)
Upper link grounded node	741	637	0
Drag link grounded node	-1691	-388	-3
Mid-spar fitting 1 grounded node	-42	-104	0
Mid-spar fitting 2 grounded node	-42	-104	0
Total reaction force	-1044	41	-3

The maximum lateral displacement under the 1g lateral loading is -1.19″ at the lower side of the inlet (see figure 32).

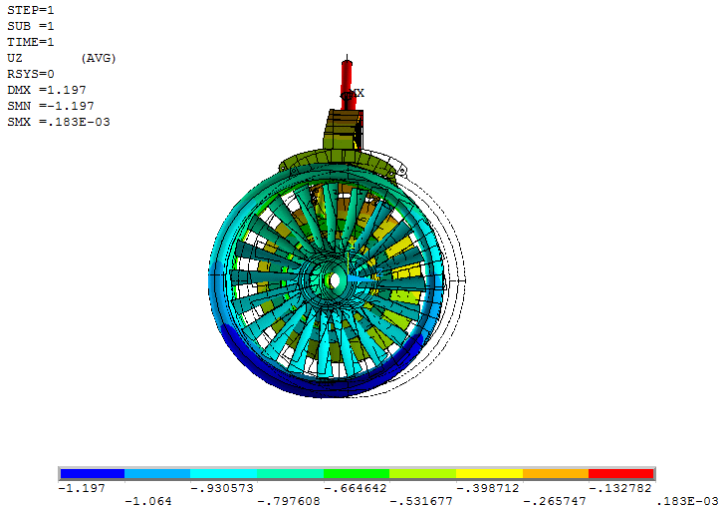

Figure 32. Lateral Displacement of the FBO Full-Fan Rig Model Under 1g Lateral Loading

2.7.2 Static Analysis Load Case 2: 1000-lb Load on A-Flange in Lateral and Vertical Directions

In this load case, the A-flange of the casing was subjected to a 1000-lb load in the vertical and lateral directions. The load was applied at the center of rigid links, which were attached to nodes at the A-flange (see figure 33).

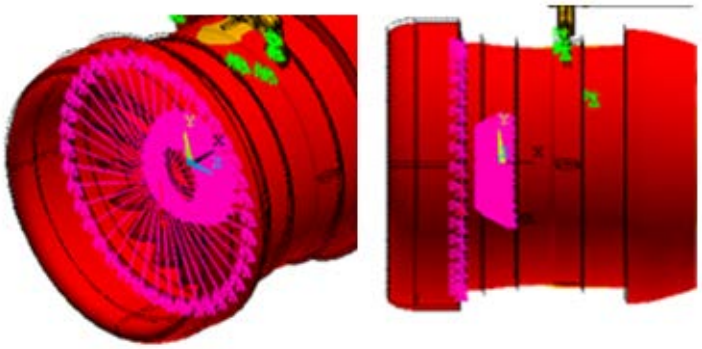

Figure 33. Details of Static Fan Disk Centerline Loading

The maximum displacement under the 1000-lb vertical loading is -0.9″ (see figure 34). For 1000-lb lateral loading, the maximum displacement is -1.75″ at the lower side of the inlet (see figure 35).

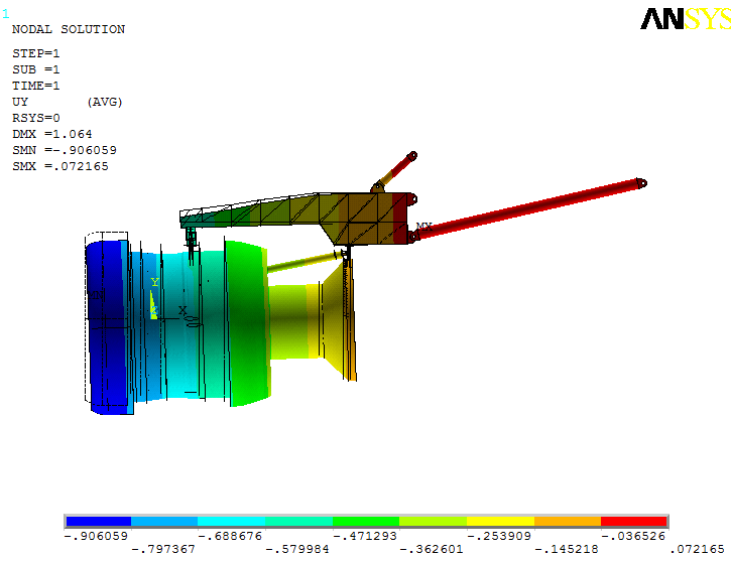

Figure 34. Vertical Displacement of the FBO Full-Fan Rig Model Under Vertical 1000-lb Loading on A-Flange

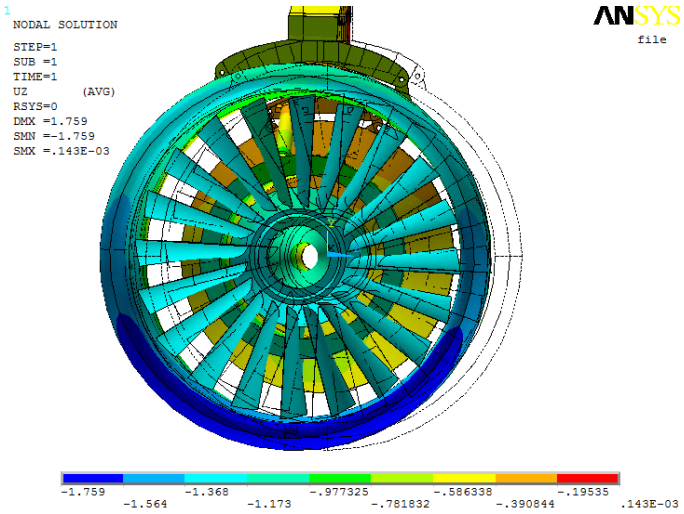

Figure 35. Lateral Displacement of the FBO Full-Fan Rig Model Under Lateral 1000-lb Loading on A-Flange

2.7.3 Static Analysis Load Case 3: 1000-lb Load on Fan Disk Centerline in Lateral and Vertical Directions

In this load case, a 1000-lb load has been applied to the fan disk-rotor CG (see figure 36). The load has been applied at the center of rigid links, which are attached to a group of nodes at the CG section of the fan disk-rotor system.

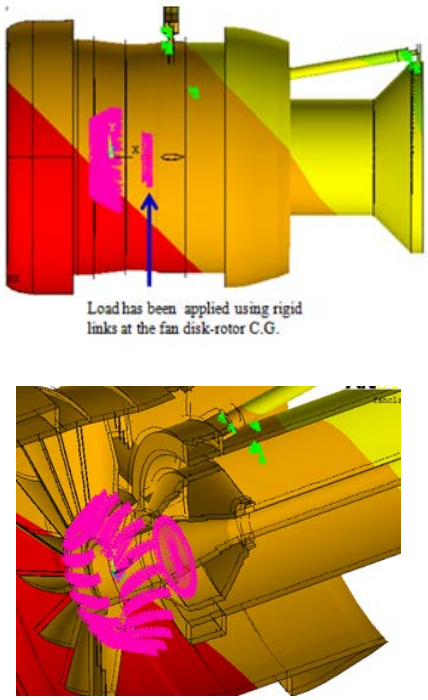

Figure 36. Details of Static Fan Disk Centerline Loading

For the 1000-lb load on fan disk-rotor centerline in the lateral direction, the maximum lateral displacement is 1.54″ at the lower side of the inlet (see figures 37 and 38).

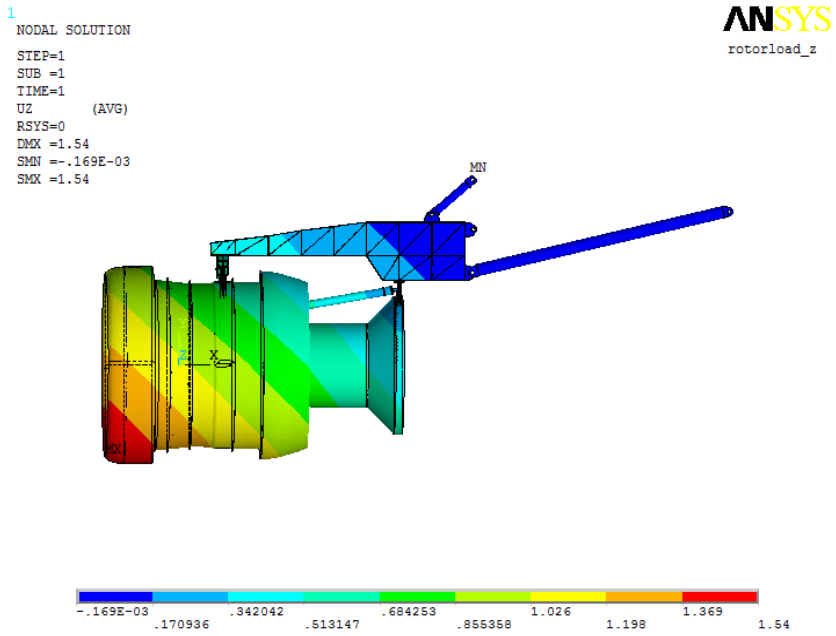

Figure 37. Lateral Displacement of the FBO Full-Fan Rig Model Under Lateral 1000-lb Loading on Fan Disk Centerline

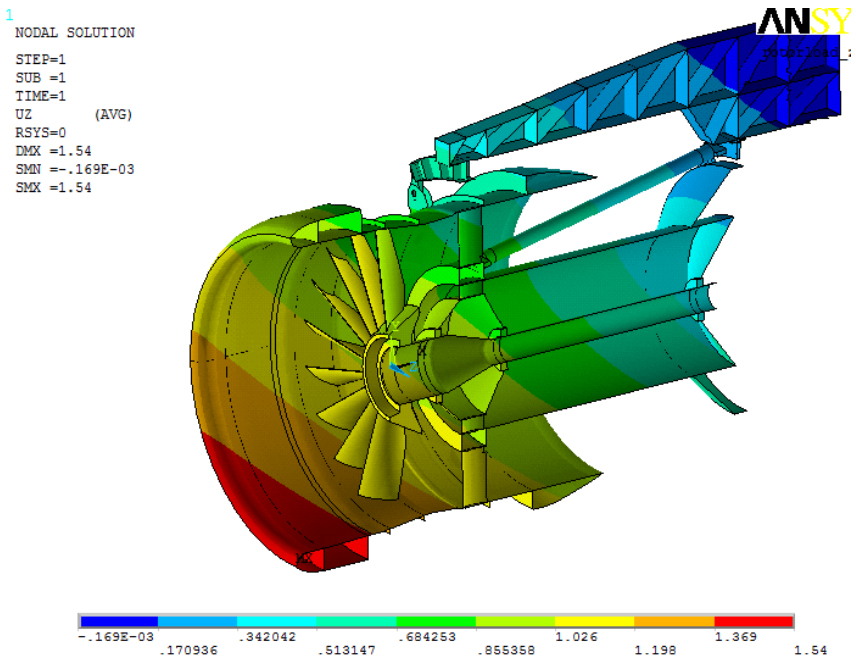

Figure 38. Lateral Displacement of the FBO Full-Fan Rig Model Under Lateral 1000-lb Loading on Fan Disk Centerline

Maximum vertical displacement under 1000-lb vertical loading on fan disk-rotor centerline is -0.7″ (see figures 39 and 40).

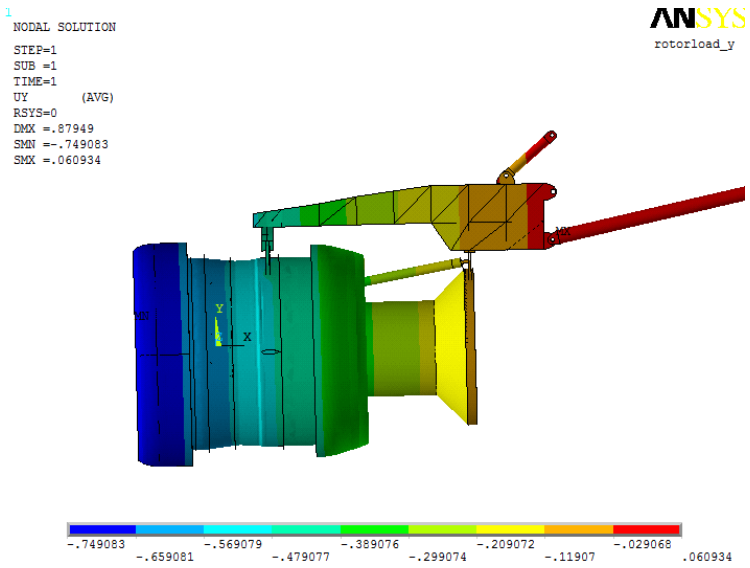

Figure 39. Vertical Displacement of the FBO Full-Fan Rig Model Under Vertical 1000-lb Loading on Fan Disk Centerline

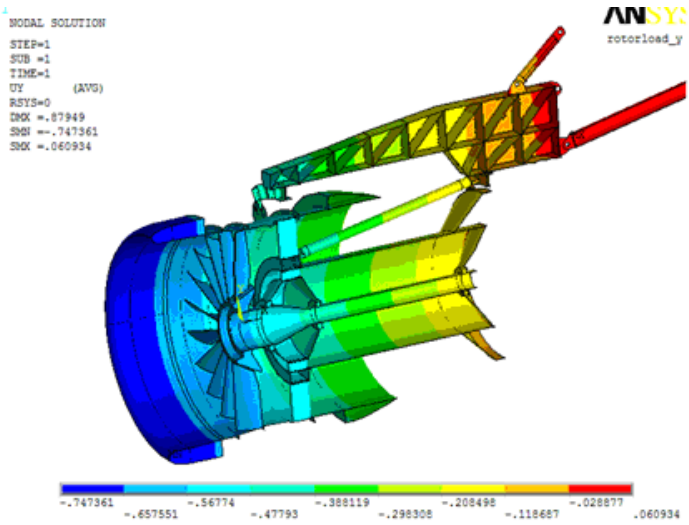

Figure 40. Vertical Displacement of the FBO Full-Fan Rig Model Under Vertical 1000-lb Loading on Fan Disk Centerline

2.8 MODEL CHECKOUT BASED ON DYNAMIC CHARACTERISTICS OF THE FBO FULL-FAN RIG MODEL

2.8.1 Natural Frequency Analysis and Corresponding Mode Shapes Through the Operating Range of Full-Fan Rig Model

The ANSYS v11.0 FE implicit code was used to perform modal analysis of the FBO full-fan rig model. The modal analysis was run using double precision; figure 41 shows the mesh. The Block Lancoz option was used to extract the 21 modes within the 0–200 Hz operating range. Pinned boundary conditions were applied at the ground connection points, as was done for the static analysis (see figure 42). The first six modes are low-frequency engine-rigid-body modes between 0–45 Hz. The remainder of the modes, 45–200 Hz, consisted of system and local component modes.

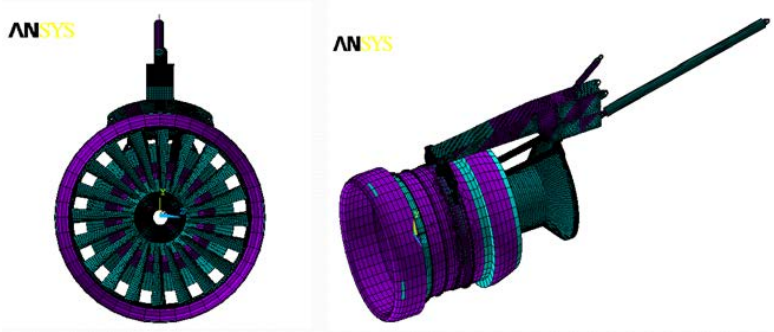

Figure 41. Mesh of the FBO Full-Fan Rig Model in ANSYS

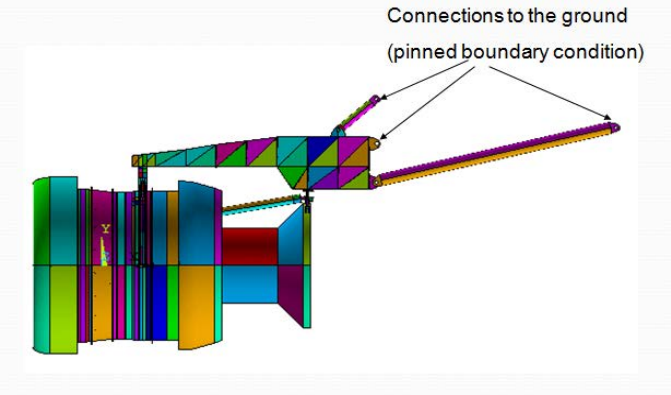

Figure 42. Modal Analysis Boundary Conditions

The first mode of the full-fan rig model is the rig rigid body rocking mode in the horizontal plane or yaw direction at 3.9 Hz. Figure 43 shows the yaw mode shape plotted against the undisplaced position of the engine. This mode corresponds to yaw motion of rig resulting from lateral bending of the strut. In addition, distribution of the sum of the normalized displacements has been shown in a contour plot for the yaw mode in figure 43.

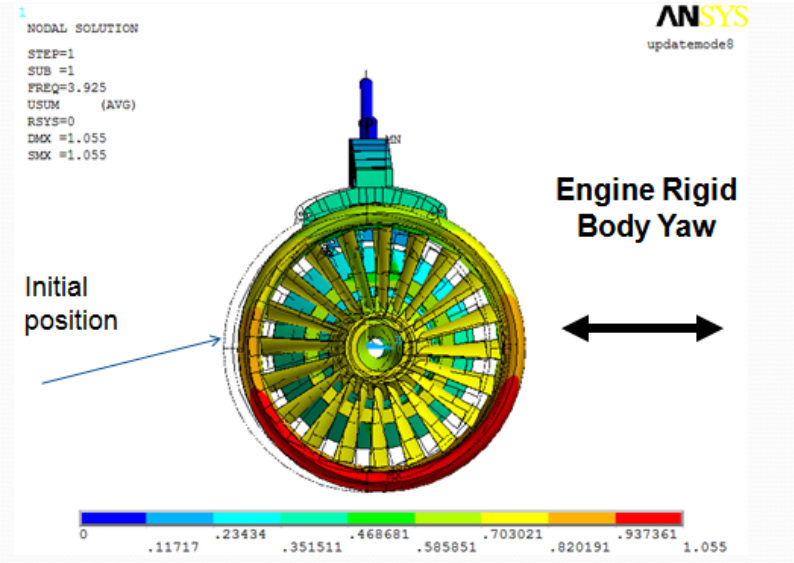

Figure 43. Mode 1—Engine Rigid Body Yaw Mode—3.9 Hz

The second mode of the full-fan rig model is the rig rigid body rocking mode in the vertical plane at 4.3 Hz. This mode is a function of strut vertical bending and corresponds to pitching motion in the vertical plane. Figure 44 shows the pitch mode shape compared to the initial position of the engine. Also, distribution of the sum of the normalized displacements has been shown in a contour plot with respect to pitch mode in figure 44.

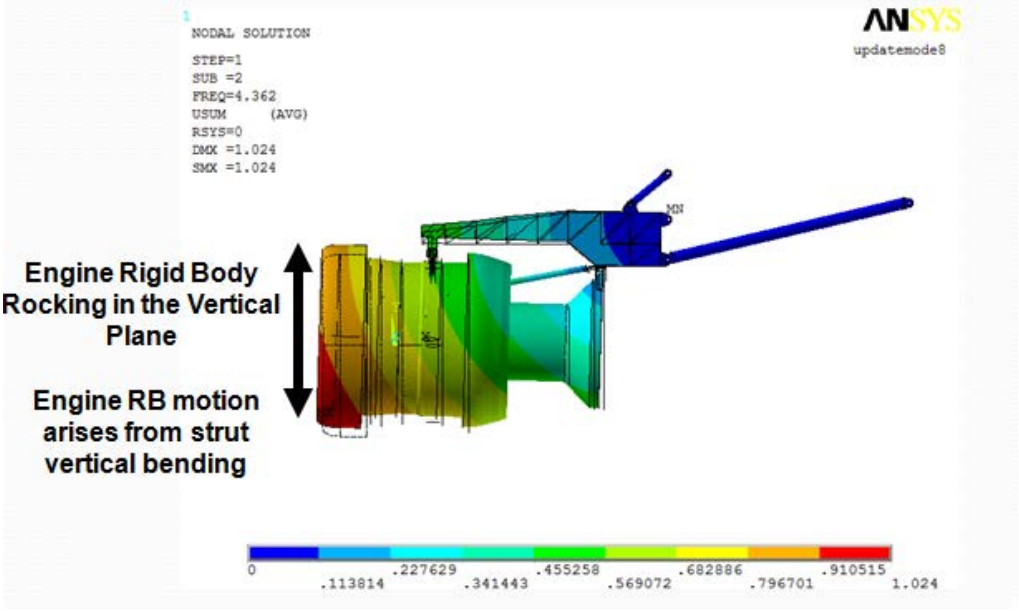

Figure 44. Mode 2—Engine Rigid Body Rocking in the Vertical Plane 4.3 Hz

The third mode of the full-fan rig model is the rig rigid body torsional mode at 10.4 Hz. This mode arises from the rolling motion of the whole structure. Because the strut is located off the engine centerline and its flexibility is significantly different at the front and rear mounts, the reaction to rig torsion introduces out-of-plane motion. Figure 45 shows the torsional mode shape compared to initial position of the engine.

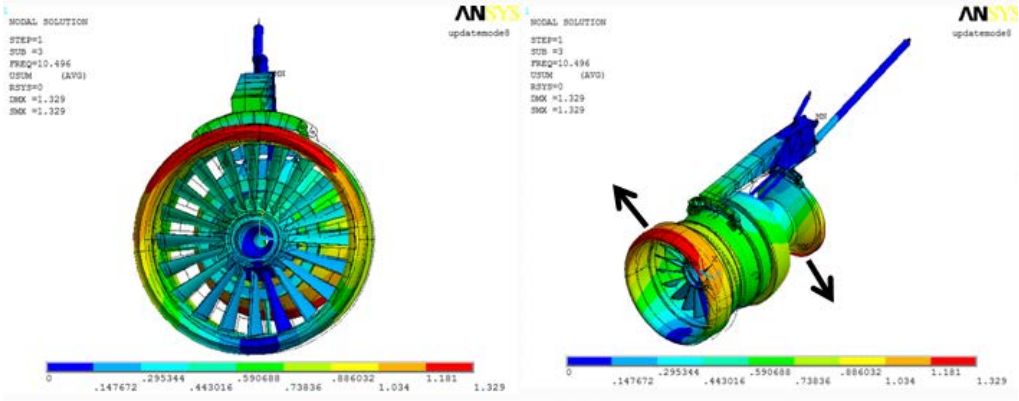

Figure 45. Mode 3—Engine Rigid Body Roll Mode 10.4 Hz

The fourth mode of the full-fan rig model is the second strut lateral bending mode at 19.3 Hz. This mode produces yaw motion of the engine with the front and rear mounts out of phase corresponding to the second lateral bending shape of the strut. Figure 46 shows the lateral bending mode shape compared to initial position of the engine.

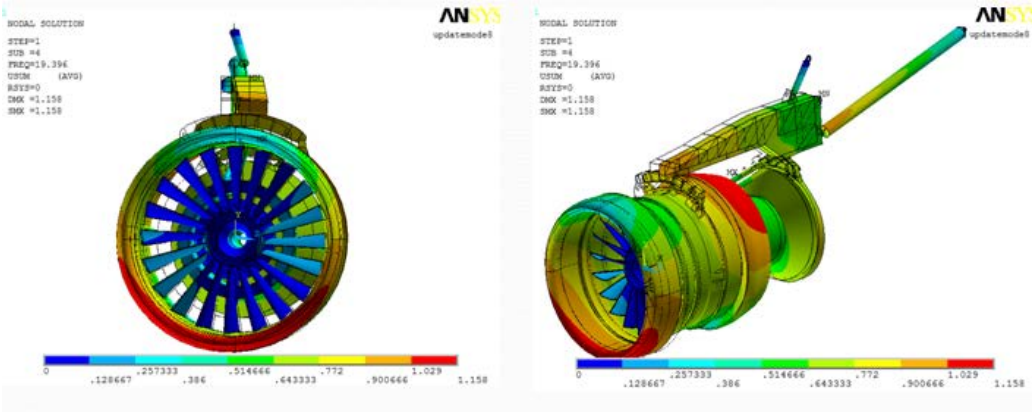

Figure 46. Mode 4—Strut Second Lateral Bending Mode—19.3 Hz

The fifth and sixth modes of the full-fan rig model are related to the fan case rocking. The fifth mode is the fan case rocking with the core case and front mount flexure at 32 Hz (see figure 47). The sixth mode is the fan case rocking with the strut at 42 Hz (see figure 48). Table 14 shows other mode characteristics between 0–200 Hz, including the frequency and the identification of the modes.

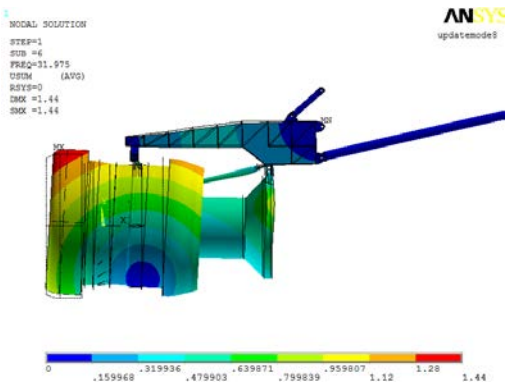

Figure 47. Mode 5—Fan Case Rocking With Core Case and Front Mount Flexure—32 Hz

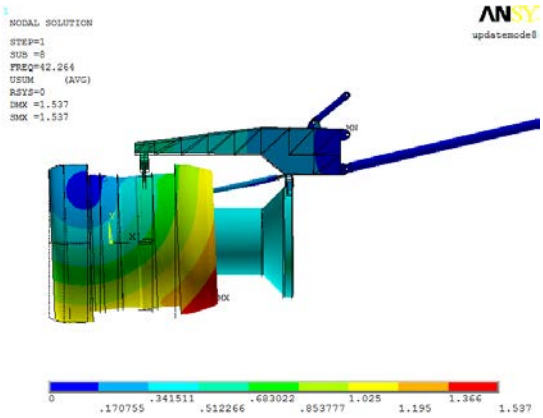

Figure 48. Mode 6—Fan Case Rocking With Strut—42 Hz

Table 14. The FBO Full-Fan Rig Model Mode Identification

Mode	Frequency (Hz)	Identification
1	3.9	Engine rigid body—yaw mode
2	4.3	Engine rigid body rocking in the vertical plane-pitch mode
3	10	Engine roll mode—torsional mode
4	19	Strut second lateral bending mode
5	32	Fan case rocking with core case and front mount flexure
6	42	Fan case rocking with strut
7	52	Fan case + core/turbine casing shell modes
8	59	Rear mount—strut yaw coupling
9	69	Fan frame flexure—vertical plane
10	70.5	Fan frame flexure—lateral plane
11	80	Drag link primary bending mode
12	85	Drag link secondary bending mode
13	90	Engine rocking in the longitudinal plane—axial mode
14	97	Front mount first bending mode
15	104	Nozzle local shell mode
16	115	Fan bladed disk modes (zero speed)
17	138	Front mount secondary excitation mode
18	171	Front mount link mode
19	179	Thrust link—pogo mode
20	194	Front mount connection link excitation mode—left link
21	197	Front mount connection link excitation mode—right link

2.9 THE FE MODEL OF FULL-FAN RIG MODEL IN LS-DYNA

The fan blades and containment structure were modeled using eight-noded, reduced integration constant stress brick elements in LS-DYNA. Viscous-based hourglass control was applied for both the blades and containment structure. The rotor shaft was modeled using four-noded, reduced integration Belytschko-Tsay shell elements with four integration points through the thickness. To initialize the rotating parts, first the translational velocities for all node points need to be established, and then the corresponding centrifugal prestress needs to be calculated for all elements. The translational velocities for all rotating parts were established using INITIAL_VELOCITY cards. Stress initialization due to steady-state spinning was done using

the LS-DYNA implicit solver, and then the resulting centrifugal stresses were used to initialize the rotating part with the INITIAL_STRESS_SOLID card for blades and the INITIAL _STRESS_SHELL card for shaft elements. MAT_ADD_EROSION, with failure time option, was used for the first two rows of elements at the released blade root to initiate the blade release. Bearing number 1, a ball bearing, takes axial and radial loads and was modeled using the CONSTRAINED_JOINT_SPHERICAL card. Bearings 2 and 3 are roller bearings and carry only radial load. The roller bearings were modeled using CONSTRAINED_JOINT_CYLINDRICAL cards. Bearing stiffness values were input using the CONSTRAINED_JOINT_STIFFNESS_TRANSLATIONAL card.

The contact interface between the blades and containment case was defined using the CONTACT_ERODING_SURFACE_TO_SURFACE card with options soft=2 (pinball segment-based contact) and sbopt=5 (warped segment and sliding checking) options. Segment-versus-segment-based force transfer algorithms are used in segment-based contact (soft=2). Self-contact of the released blade was modeled using the CONTACT_ERODING_SINGLE_SURFACE card in LS-DYNA. The eroding contact option allows erosion within a body and subsequent treatment of contact with new surfaces. A static friction coefficient of 0.1 is used for contact interfaces. The CONTROL_ACCURACY card was activated to improve computational accuracy. Objective stress update (osu=1) and invariant node-numbering (inn=4) options were invoked because they are required for the rotation of the stress tensor (spinning bodies) during the analysis. Boundary conditions on the fan casing were applied using the *BOUNDARY_SPC card in LS-DYNA at phase 1 for the three blade fan rig model. In the phase 1 fan rig model, the fan case was isolated from the fan rotor, so zero displacement constraints were applied in the axial direction (*Dx*) to the node set on the back surface of the fan casing and the vertical and horizontal displacements (*Dy* and *Dz*) of the right and left fan case mounting lugs were constrained using sets of nodes around the bracket holes (see figure 49). This allowed the fan case to deform during the blade-impact event, but did not allow rigid body inertial translation of the case.

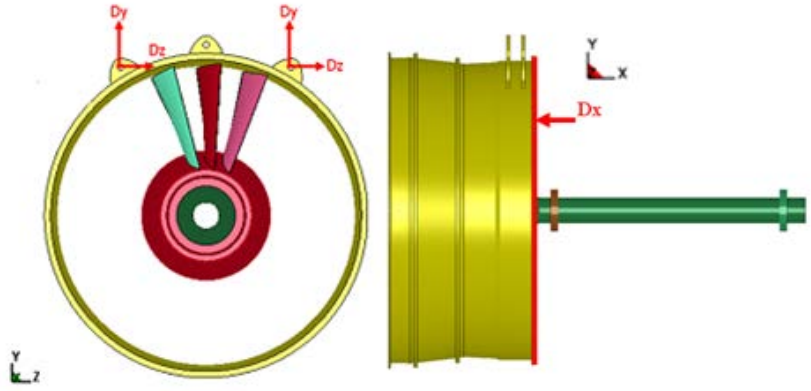

Figure 49. Boundary Conditions on the Fan Case Mounting Lugs of the Three-Blade Rig Model

In phase 2, the full-fan rig model incorporated the fan frame and core case to connect the fan shaft to the fan case. The fan case was connected to the strut front mount at the fan case lugs. As a result, the displacement constraints applied to the fan case in phase 1 were not applied in

phase 2. Figures 50 and 51 show the phase 2 connections between the fan case and adjoining structure.

Figure 50. Fan Case Mounting Lugs—Front Mount Connection (phase 2)

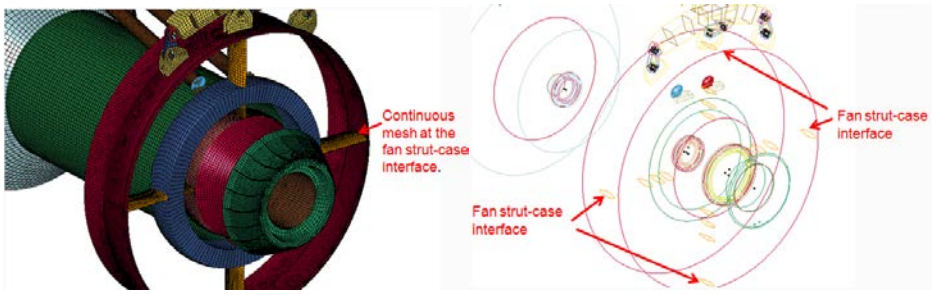

Figure 51. Fan Strut-Fan Case Interface (phase 2)

The full-fan rig model is attached to the wing through the pylon at three points. These points are drag-link bracket, upper-link bracket, and the mid-spar fitting clevis. The wing itself has not been modeled and is assumed to have infinite stiffness. Therefore, three attachment points are treated as ground connection points of the rig model (see figure 52). For each connection point, zero displacement boundary conditions in x, y, and z directions were applied to the bracket hole central node, which was connected to the nodes around the hole of brackets using the nodal rigid body card. This type of boundary condition is representative of a spherical joint because only zero displacement boundary conditions were applied and x, y, and z rotations were left free at these four connection points.

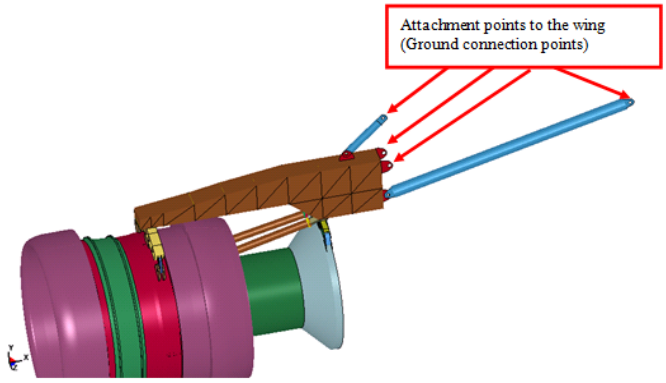

Figure 52. Ground Connection Points of the Rig Model (phase 2)

In phase 1, the released blade was modeled using solid elements nominally 0.075″ on a side (in-plane) in the zones where the blade typically breaks (see figure 8), and 0.10″ on a side (in-plane) over the remainder of the blade. Four elements were used through the thickness of the released blade. The trailing blades were modeled with 0.15″ elements (in-plane element size) and three elements through the thickness. The fan case was modeled with 0.08″ elements (in-plane element size) and six elements through the thickness in the main damage zones of the fan casing. Away from the main damage zones, two elements were used through the thickness with a 0.2″ in-plane element size. Table 15 shows the total number of elements for each component.

Table 15. Number of Elements Used in Each Model Component, Phase 1

Component	Total Number of Elements - Element Type
Containment case	1,222,704 - Solid
Released blade	30,240 - Solid
Trailing blade#1	9072 - Solid
Trailing blade#2	9072 - Solid
Shaft	3780 - Shell

In phase 2, the full-fan rig model released blade, trailing blade 1, and trailing blade 2 were modeled using solid elements, nominally 0.14″ in-plane element size and three elements through the thickness of the fan blade. The larger mesh size is a tradeoff between accuracy and running time. The other 17 blades were modeled using nominally 0.2″ in-plane element size and three elements through the thickness. Fan casing and blade meshes are shown in figures 53 and 54. Table 16 shows the total number of elements for each component in the model, and table 17 shows the total number of elements for the full-fan rig model. Figure 55 shows mesh details regarding the other components of the full-fan rig model.

Table 16. Number of Elements Used in Each Model Component, Phase 2

Component	Total Number of Elements - Element Type
Containment case	822,704 - Solid
Released blade	10,545 - Solid
Trailing blade#1	10,545 - Solid
Trailing blade#2	10,545 - Solid
17 fan blades	5148 - Solid
Shaft	3780 - Shell

Table 17. Full-Fan Rig Model FE Data

Model	Number of Elements	Element Type
FBO full-fan rig model (fan casing, brick elements)	1,309,165	944,676(brick) + 364,489(shell)
FBO full-fan rig model (fan casing, shell elements)	330,882	123,904(brick) + 206,978(shell)

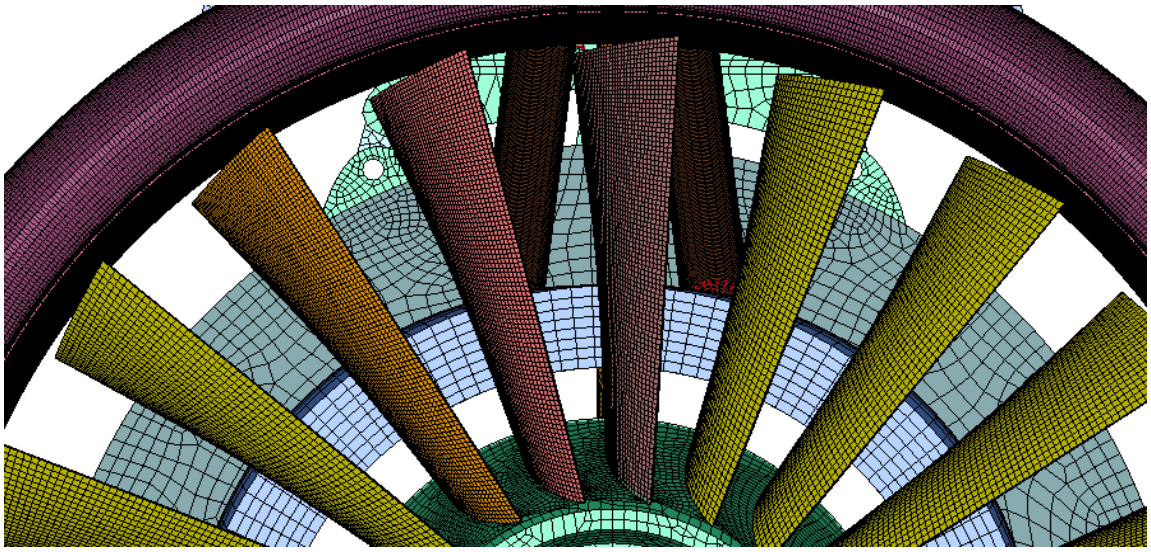

Figure 53. Mesh Details for the Fan Blades (brick elements)

Figure 54. Mesh Details for the Fan Containment Case (brick elements)

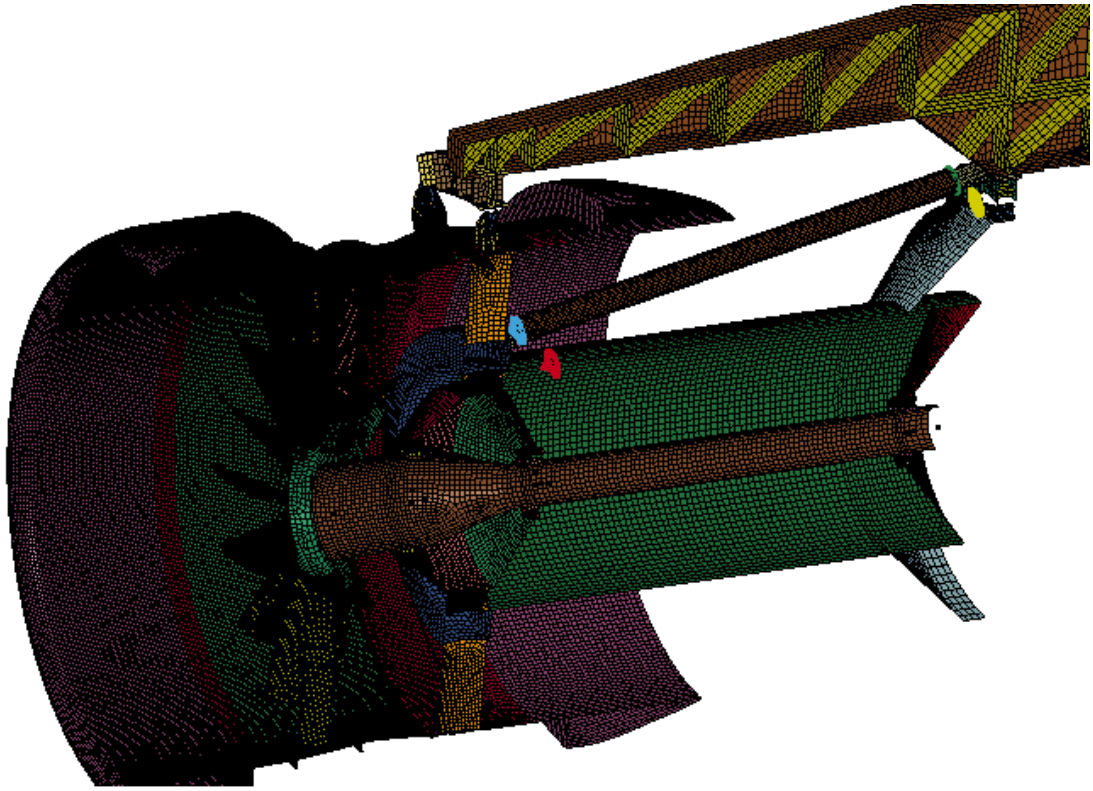

Figure 55. Half-Section Cut View of the Rig Model Mesh

In phase 2, the modeling of connections between components is important to ensure connection kinematics and force flow through components under FBO loading are accurately represented in the full-fan rig FE model. The following connections between major components were modeled in detail in the LS-DYNA full-fan rig FE model:

- Thrust link to thrust yoke
- Thrust link to aft mount yoke
- Fan strut to containment case connection points
- Front mount mounting lug to front mount connection link
- Aft mount mounting lug to aft mount connection link

The thrust link to thrust yoke and thrust link to aft mount yoke connections were modeled using a spherical joint card. Figure 56 shows these two thrust link connection points. The spherical joint connects two concentrally located nodes. These two nodes were then connected to their corresponding nodes on the thrust link and thrust yoke using nodal rigid body cards. This type of connection models the spherical pivots in the real hardware and ensures that the thrust links carry only axial forces and are not subjected to bending moments during the FBO event.

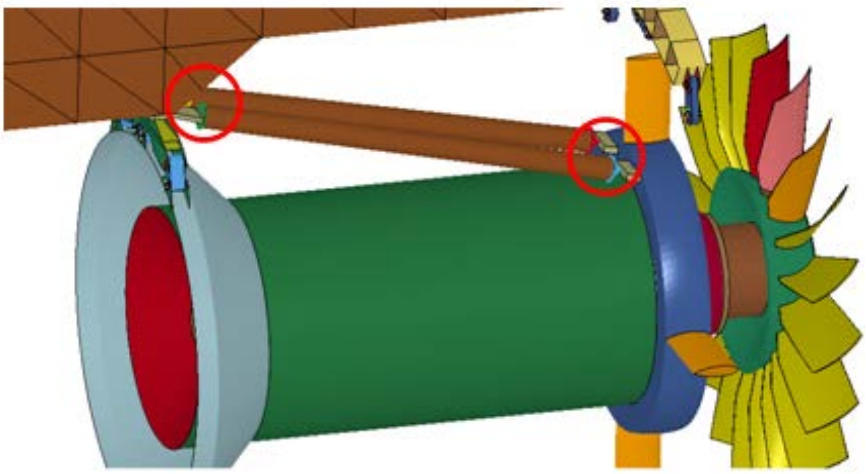

Figure 56. Thrust Link Connection Points

Figures 57–59 show details for the spherical joint connections between the thrust links and aft mount. Nodal rigid bodies and central nodes that attach the spherical joint to the adjoining components can be seen in these figures. Similarly, figure 60 show details regarding the thrust link to thrust yoke spherical joint connections.

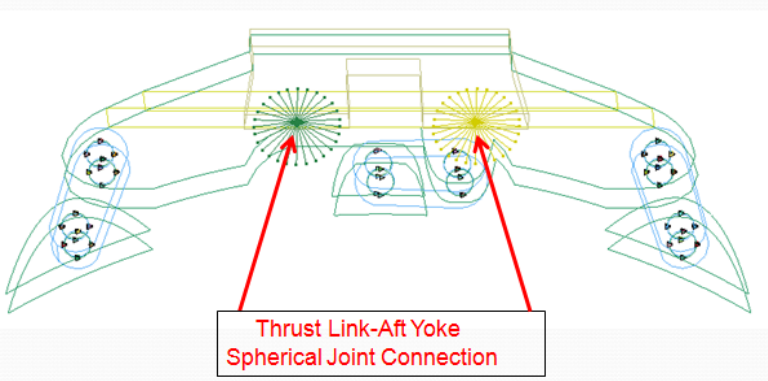

Figure 57. Connection Points of Aft Mount

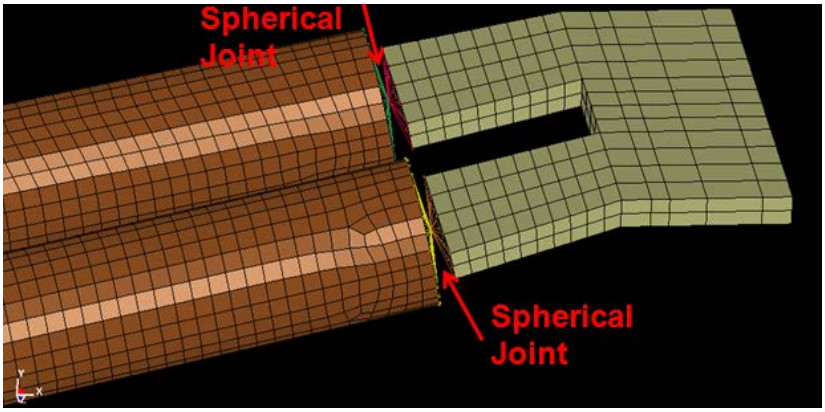

Figure 58. Thrust Link to Aft Mount Yoke Spherical Joint

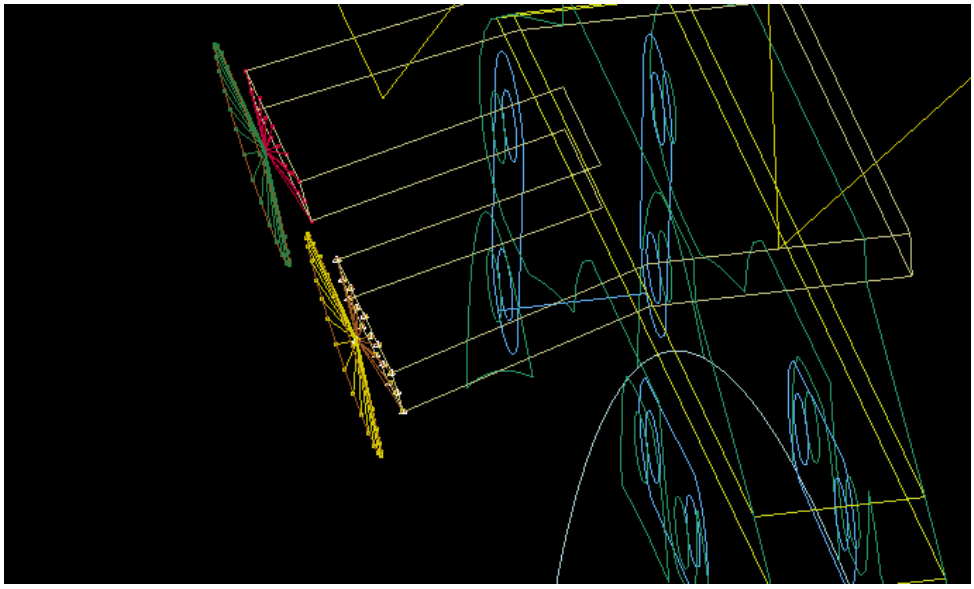

Figure 59. Thrust Link to Aft Mount Yoke Spherical Joint Details

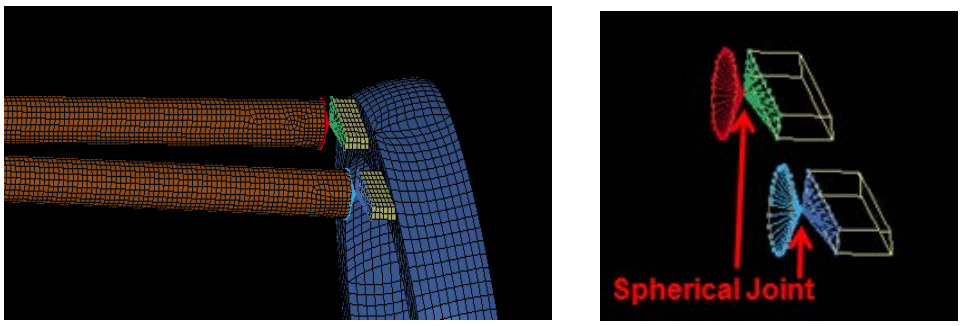

Figure 60. Thrust Link to Thrust Yoke Spherical Joint Details

The fan frame (fan case strut) to fan containment case connection is important in terms of coupled displacement behavior of the core case and bearing supports (fan shaft reaction loads) relative to the containment case. This coupled response impacts the post-containment interactions between the other blades and the fan case. The modeling approach used here was a continuous mesh between the fan frame struts and fan case interfaces. At connection points, two components share the same interface node set (see figures 61 and 62).

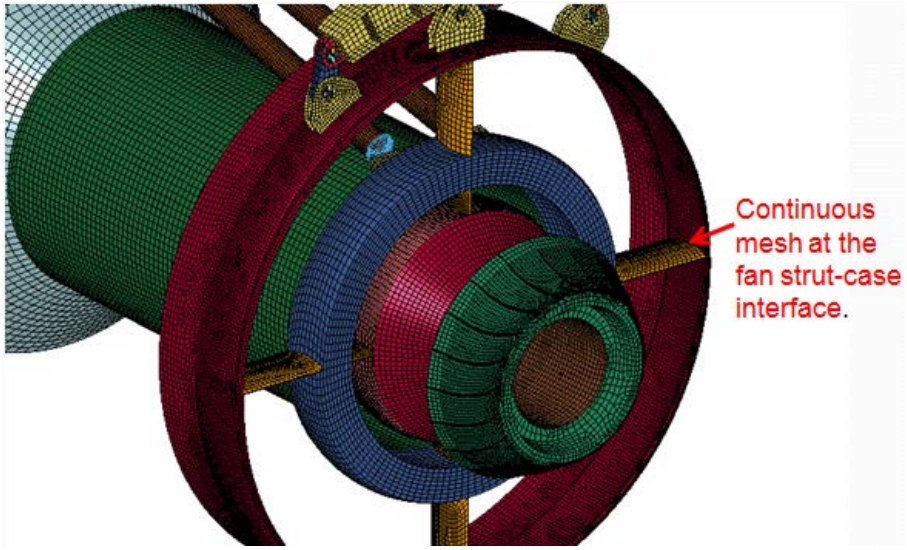

Figure 61. Fan Strut to Containment Case Connection

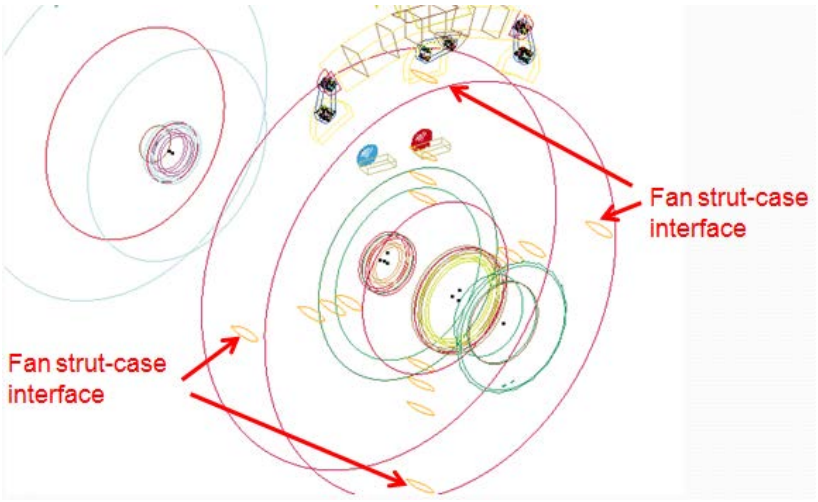

Figure 62. Fan Strut to Containment Case Interface

The fan case mounting lug to front mount connection link (see figure 63) and turbine frame mounting lug to aft mount link connections (see figure 64) were modeled using a nodal coupling card for the nodes at the bracket-hole to link-hole interface. The pins and associated clearance that would be in a real mount were not modeled and lug-link connections were assumed to be zero displacement. For each of the right and left lug-to-link interfaces, four nodes were selected representing the quarter-circle hole locations on each lug/link, and these were zero displacement coupled (see figures 65 and 66). The center (redundant) links on the forward and aft mounts were similarly coupled, but only using two opposing locations at each lug/link interface (see figures 65 and 66).

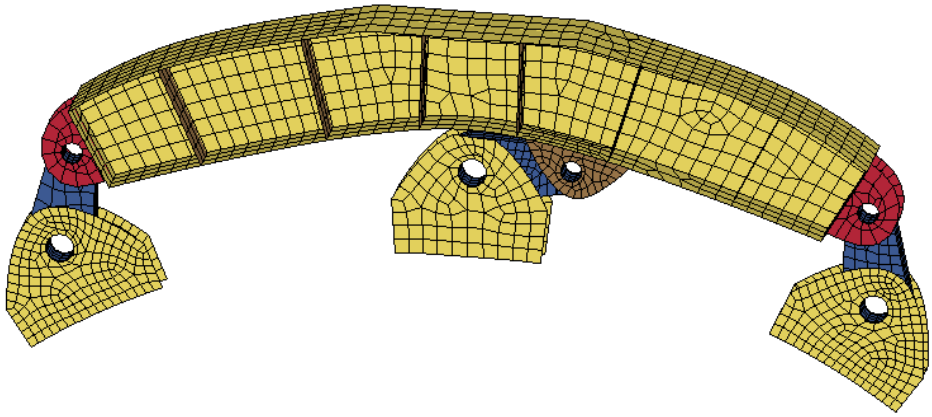

Figure 63. Forward Mount

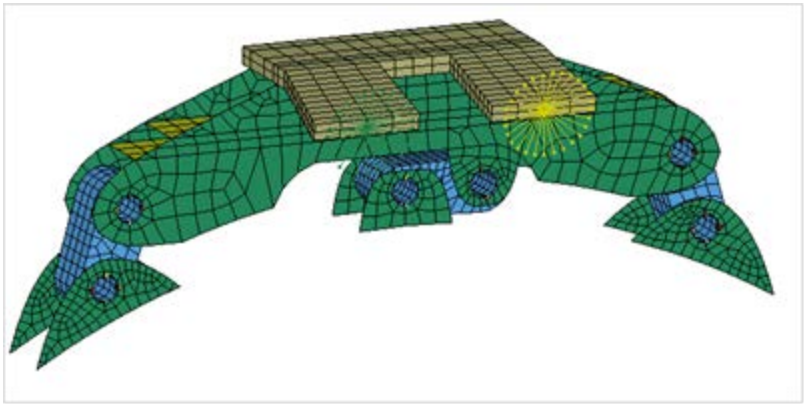

Figure 64. Aft Mount

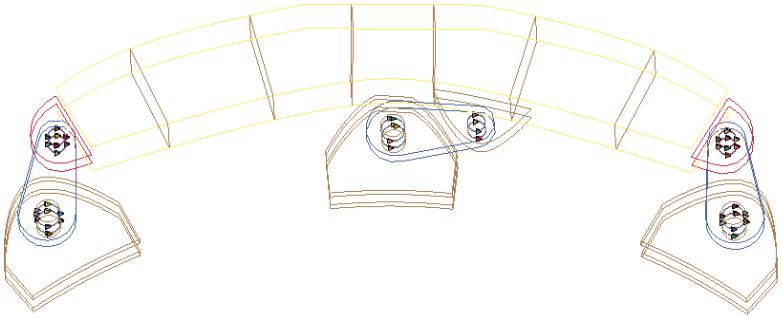

Figure 65. Connection Points of Forward Mount

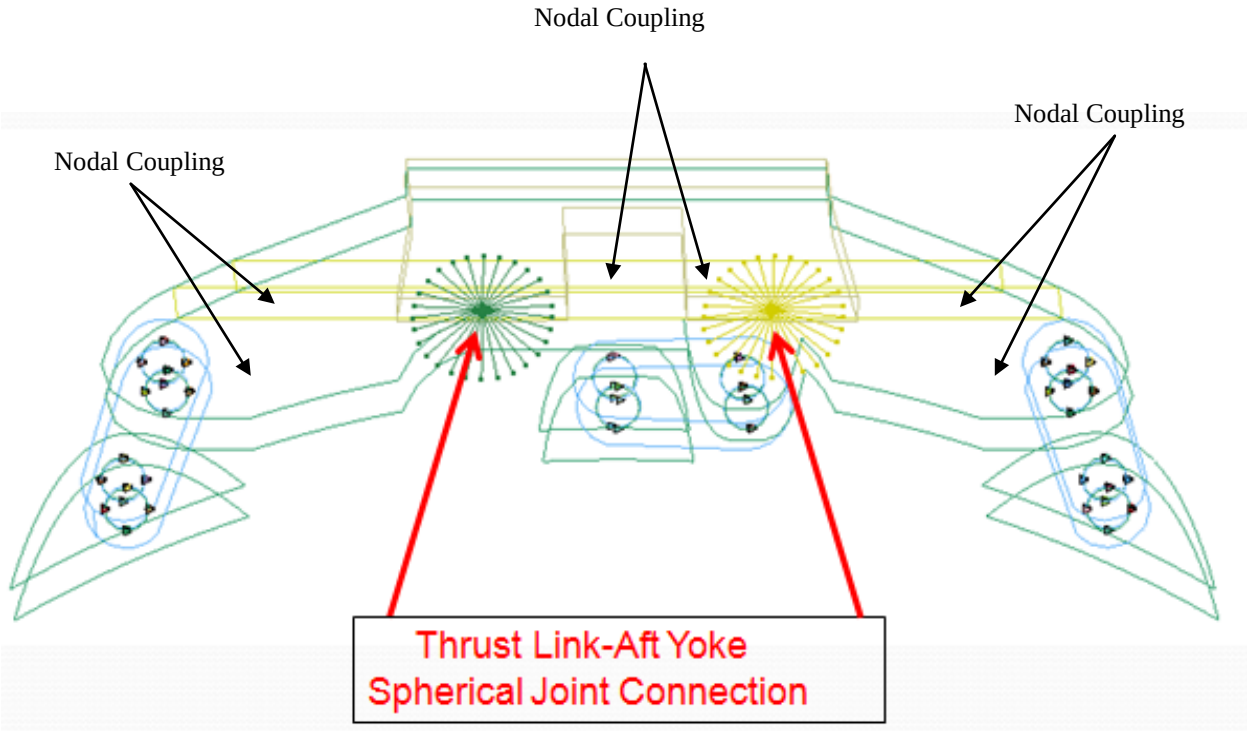

Figure 66. Connection Points of the Aft Mount to Spherical Joint and Nodal Coupling

Because of the high strain rates that occur in an FBO event, strain-rate-dependent material properties were necessary in these simulations. The Johnson-Cook material model was selected for both the fan blades and casing so the model could account for strain-rate-dependent plasticity and failure. Plasticity and failure data for each of the materials used in the rig model were taken from publications available in the open literature. Lawrence Livermore National Library (LLNL) [6, 7] published data for the deformation behavior of Ti-6Al-4V titanium and 2024-T3/T351 aluminum collected during their investigation of material characterization performed to support modeling of turbine engine uncontainment events. Buyuk, Loikkanen, and Kan [8] evaluated the effect of Johnson-Cook damage parameters for 2024-T3/T351 aluminum during studies they conducted to understand impact loading of gas turbine engine containment and fragment-shielding structures. Table 3 compares the Johnson-Cook parameters from these studies. It was found that the Johnson-Cook material models for Al 2024-T351 LLNL-2 and LLNL-3 have the same plasticity properties, but different damage properties (see table 18). The fracture locus at a nominal strain rate of 1/s for Ti-6Al-4V titanium and 2024-T3/T351 aluminum is shown in figures 67 and 68, respectively. A piecewise linear plasticity material model was generated for the SS-304 rotor shaft using material properties based on NASA Glenn Research Center test data. Tables 19 and 20 show the relevant properties for SS-304 and Inconel-718 material models.

Table 18. Johnson-Cook Parameters for Ti 6Al-4V and Al 2024-T3/351

Parameter	Notation	Ti 6Al-4V	Al-2024 LLNL2	Al-2024 LLNL3
Strength Parameters				
Density (lb/in.^{3})	ρ	0.160043	0.100434	0.100434
Poisson ratio	υ	0.31	0.33	0.33
Modulus of elasticity (psi)	E	1.6E+7	1.06E+7	1.06E+7
Static yield limit (psi)	A	159,246	53,517	53,517
Strain hardening modulus (psi)	B	158,376	99,202	99,202
Strain hardening exponent	n	0.93	0.73	0.73
Strain rate coefficient	C	0.014	0.0083	0.0083
Thermal softening exponent	m	1.1	1.7	1.7
Reference temperature (^{o}F)	T_{room}	69.5	69.5	69.5
Melting temperature (^{o}F)	T_{melt}	2920	935	935
Specific heat (in.^{2}/s^2 ^{o}F)	c_p	505,000	754,000	754,000
Damage Parameters				
D_1		-0.09	0.112	0.31
D_2		0.25	0.123	0.045
D_3		-0.5	-1.5	-1.7
D_4		0.014	0.007	0.005
D_5		3.87	0	0

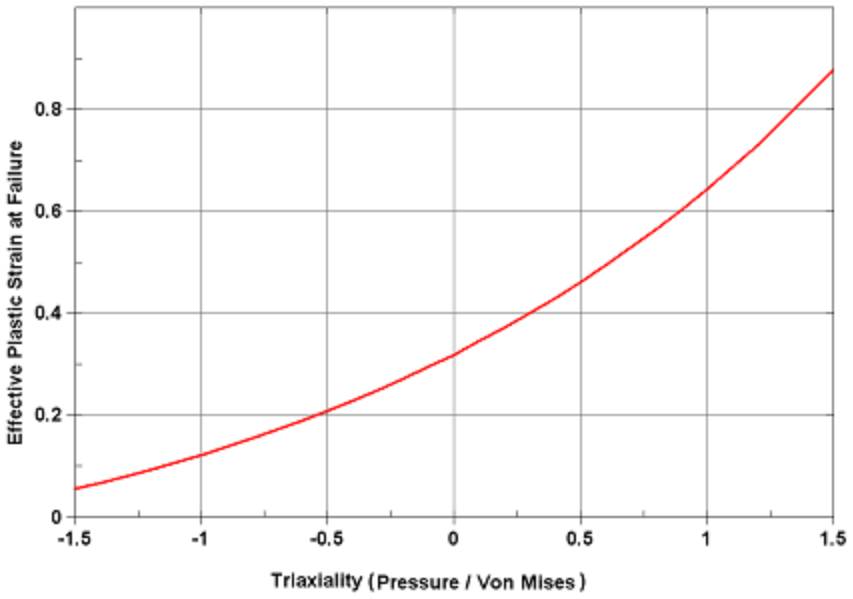

Figure 67. Fracture Locus of Ti 6Al-4V at Nominal Strain Rate of 1/s

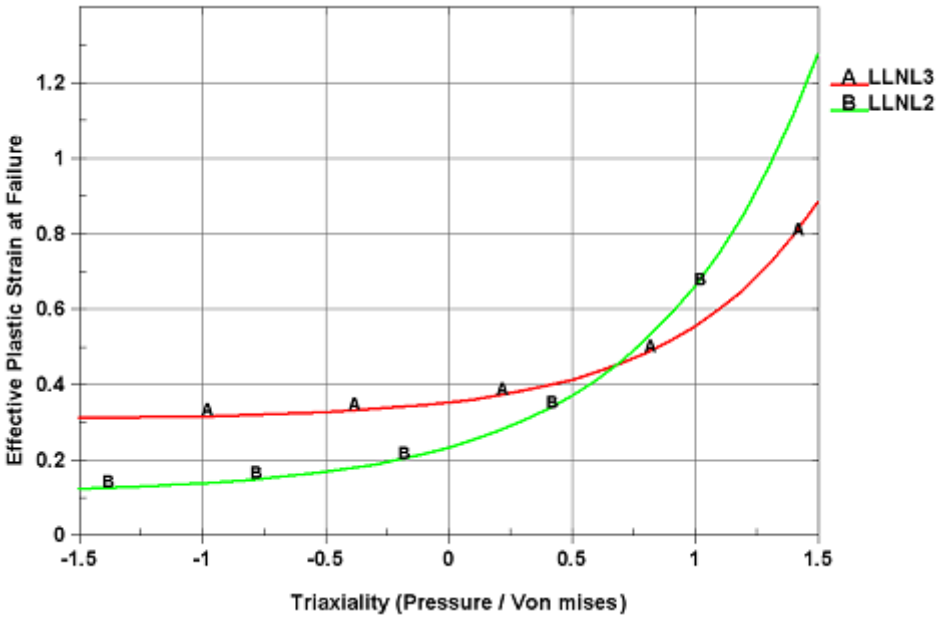

Figure 68. Difference in Fracture Locus of Al 2024–T3/T351 Nominal Strain Rate of 1/s

Table 19. The SS-304 Material Properties

Parameter	Notation	SS 304
Density (lb/in.^{3})	ρ	0.289
Poisson ratio	υ	0.305
Modulus of elasticity (psi)	E	2.8E+7
Static yield limit (psi)		49,200

SS = stainless steel

Table 20. Inconel 718 Materials Properties

Material	Youngs modulus (E)	Density	Poison ratio
Inconel 718	2.90E+07	7.72E-04	0.284

Significant problems can arise when modeling complex geometry if the model details are not faithfully represented in an FE model. If inappropriate simplifying assumptions are included, then the nonlinear dynamic behavior of some components may be degraded and the solution will not represent realistic results.

In phase 1, the three-blade rig model has the fan rotor isolated from the fan case to minimize post-release dynamic interaction between the fan and casing. The phase 1 model does not contain fan case to bearing supporting structure or any of the normal engine structural connections between the primary rig and ground. The stiffness of the bearing support structure was assumed infinite and there was no interaction between the fan case and shaft bearings during the FBO event simulations. This simplifying assumption was acceptable for the three-blade rig model because the purpose of the three-blade rig model was to assess the initial release/containment event. Because the bearing load/fan rub interaction does not occur until later in a full-engine event, the simplification does not detract from use of a three-blade rig model for assessing the initial containment event. In the phase 2 full-fan rig model, the structural connections between the fan shaft bearings and the fan case are modeled and the full 20-blade fan is included so that the model can accurately represent the initial release through post-containment fan-casing interaction.

Fan aerodynamic pressure and thermal effects were not considered because rig tests are run in an evacuated chamber under partial vacuum to reduce the drive horsepower required to spin the fan; therefore, these effects are minimized. During a normal full-engine FBO event, the blade release through initial containment occurs before the FBO-induced flow disruption can cause the engine to surge and stall; therefore, aerodynamic and surge/stall flow dynamics do not play a role in initial containment in either test. Because of this timing, loads associated with surge and stall may be considered part of the rundown and continued rotation phase following an FBO event.

The fan rig model was designed with an integrated bladed fan disk so that it would not be necessary to model the dovetail complexities contained in slotted disk fan designs. Furthermore, since the disk was intentionally designed without bladed disk modes in the operating speed range, the disk was further simplified by modeling it as a rigid part using the PART INERTIA card in LS-DYNA. In this modeling assumption, the mass, CG, and inertia properties of the disk are represented to ensure proper gross dynamic response, but flexibility is ignored because it has little contribution to the overall disk response.

In keeping with the FAA requirements for fan blade containment testing (14 CFR part 33.94), the fan blade was assumed to fail at 15% of the blade span above the disk (the rule allows up to 20%). In a traditional bladed disk design, the blade would be released at the dovetail and include the blade platform; however, there is no dovetail or platform with the blisk design, so the blade is expected to fail above the root radius in the flow path.

3. BLADE CONTAINMENT ANALYSIS—THREE-BLADE MODEL (PHASE 1)

3.1 SIMULATION OF THE FAN BLADE-OUT EVENT

All FE simulations were carried out with version 971R4 of LS-DYNA running the massively parallel processing (MPP) double-precision solver. The computations were performed on an SGI Propack 4 supercomputing platform using the Linux® operating system. Computational time for one complete revolution of the system was approximately 18 hours using 16 CPUs and the LS-DYNA MPP double-precision solver. The LS-DYNA energy data, which is printed in the glstat files, provides a useful check on an analysis to determine the correctness and stability of the numerical simulations. Figure 69 shows the total energy of the system was constant throughout the simulation. Internal energy, which includes strain energy due to elastic and plastic deformation, increases during the structural deformation of components. Sliding interface energy shows contact energy in the system. When friction is included in a contact definition, positive contact energy is to be expected. Sliding interface energy was positive throughout the analysis (see figure 69).

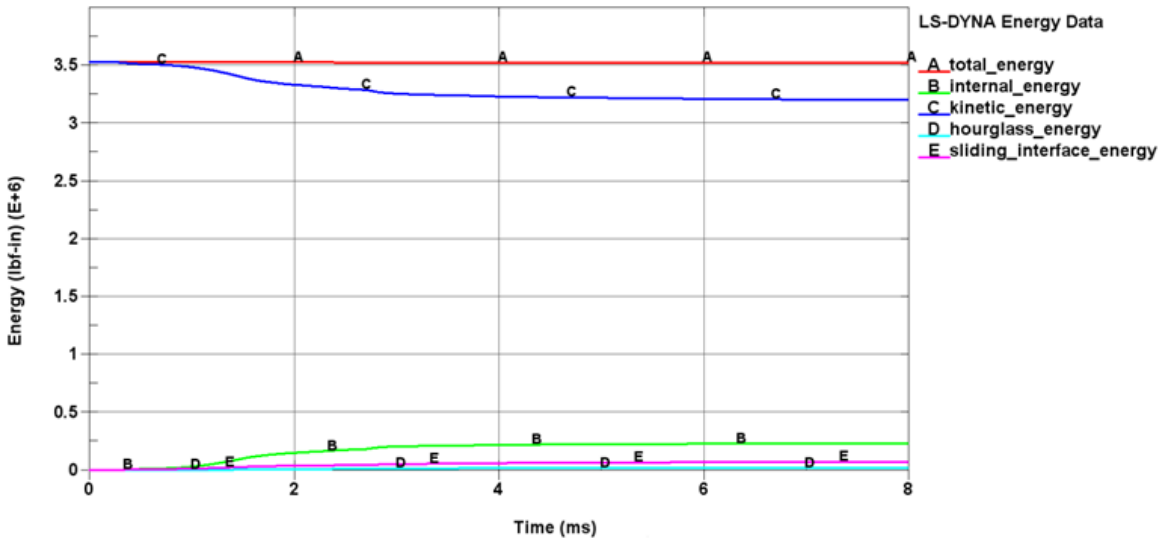

Figure 69. LS-DYNA Energy Data

Hourglass energy is the indicator of nonphysical deformation modes associated with reduced integration elements. Hourglass energy on the order of less than 10% of the maximum strain energy is a commonly accepted upper limit for numerical stability. The hourglass energies of the released blade and containment case were within allowable limits (see figure 70).

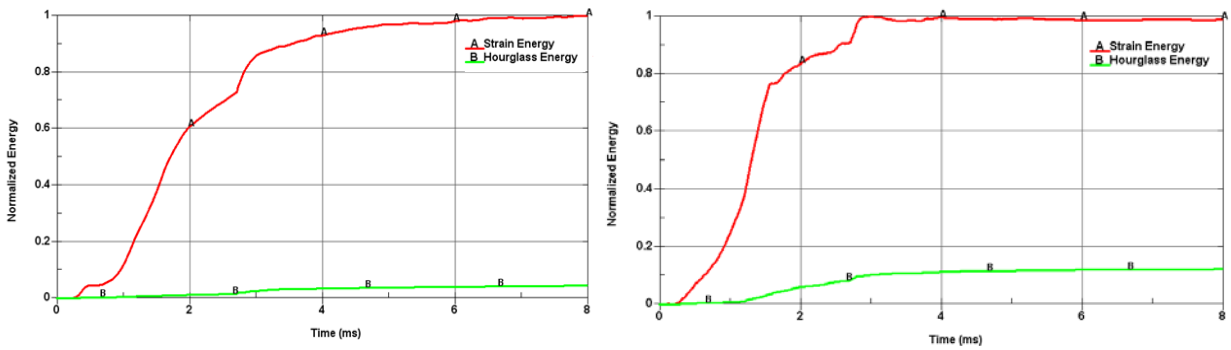

(a) (b)

Figure 70. Normalized Hourglass Energies for the (a) Containment Case and the (b) Released Blade (normalized with respect to maximum strain energy)

3.1.1 Distinct Phases of the Blade–Case Interaction

The following distinct phases of blade-case interaction during an FBO event were predicted for the three-blade fan rig model using LS-DYNA. Figure 71 shows snapshots from the analysis.

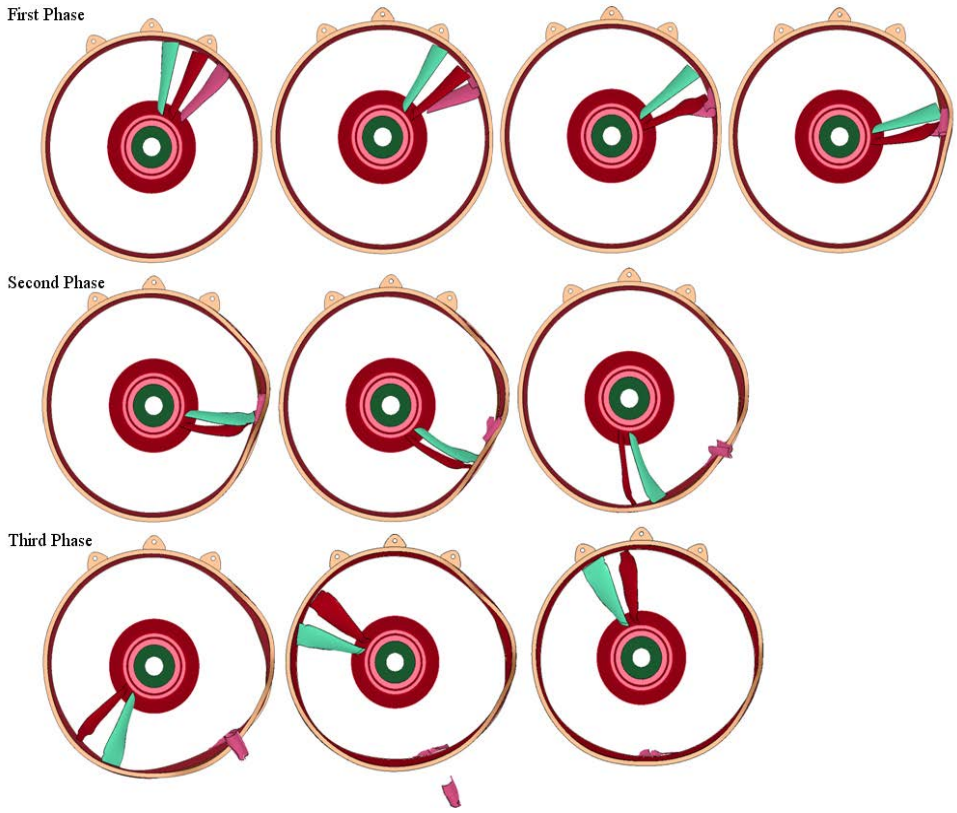

Figure 71. Distinct Phases of the Blade–Case Interaction
(view is forward looking aft; fan rotation is clockwise)

3.1.1.1 First Phase

The tip of the released blade hits the case approximately 12–15 degrees circumferentially from the release location and skates approximately 30 degrees on the case inner surface. While skating, the top 1/3 span of the released blade is bent and broken. The resulting tip fragment moves forward towards the inlet. The contact forces applied to the blade by the casing are responsible for fragmenting the blade tip and turning the translational velocity vector of the released blade CG to a combination of tangential and normal to the case. The remaining 2/3 of the released blade is caught between the fan case and tip of the trailing blade (near the root of the released airfoil fragment). The 2/3 span of the released blade airfoil hits the inner shell at an oblique angle and, depending on the containment case thickness, may punch a hole in the case. Figure 72 shows the released blade breakup and fragmentation in LS-DYNA.

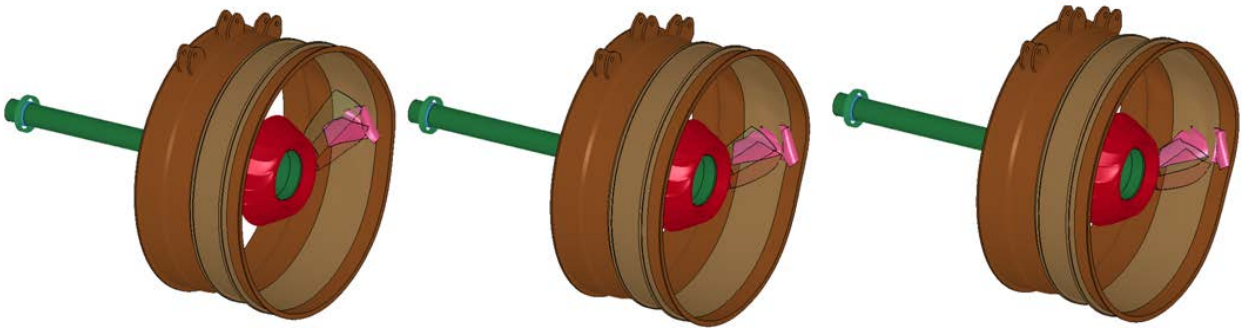

Figure 72. Blade Breakup and Fragmentation

3.1.1.2 Second Phase

The released blade root fragment is pushed by the first trailing blade pressure surface, feeding additional kinetic energy into the released blade. The root fragment of the released blade then impacts the inner surface of the case at its aft end, with a hammering impact. Meanwhile, the heavy side of the fan rotor (opposite the release blade) starts to move off-center because of the unbalanced force generated as a result of the initial blade loss.

3.1.1.3 Third Phase

After the blade root impact event, the trailing blade tips make contact with the inner surface of the casing and begin to rub on the fan case. Meanwhile, the tip fragment moves toward the inlet while the root fragment slides aft. During this phase, the fragments gradually lose much of their remaining kinetic energy.

3.1.1.4 Energy Analysis

During the event simulation, the total energy of all components was tracked to determine how much of the released blade kinetic energy was transferred while impacting various engine components and to assess the rate at which energy is dissipated through the system. Figure 73 shows the kinetic energy of the released blade and strain energies in the containment case, trailing blade #1, and trailing blade #2. The figure clearly shows that the major percentage of released blade kinetic energy is transferred into deforming the containment case. It also shows that the released blade gains kinetic energy as it is hit by the trailing blades. In figure 74, the strain energy in the containment case is plotted to understand the deformation of the casing as it is hit by the released blade and its fragments. It is clearly shown that major deformation of the fan case begins as the released blade impacts the case. The rate at which strain energy increases in the fan casing declines after the first quarter revolution, at which time the released blade has fragmented into two pieces. Later, when the root fragment impacts the case, the strain energy in the casing increases significantly. After that, the fan case continues to deform due to the trail blade tips impacting the fragments and rubbing the case, and the continued sliding of the fragments inside the casing. The fan case strain energy reaches its maximum level at approximately three quarters of a revolution following the initial blade release.

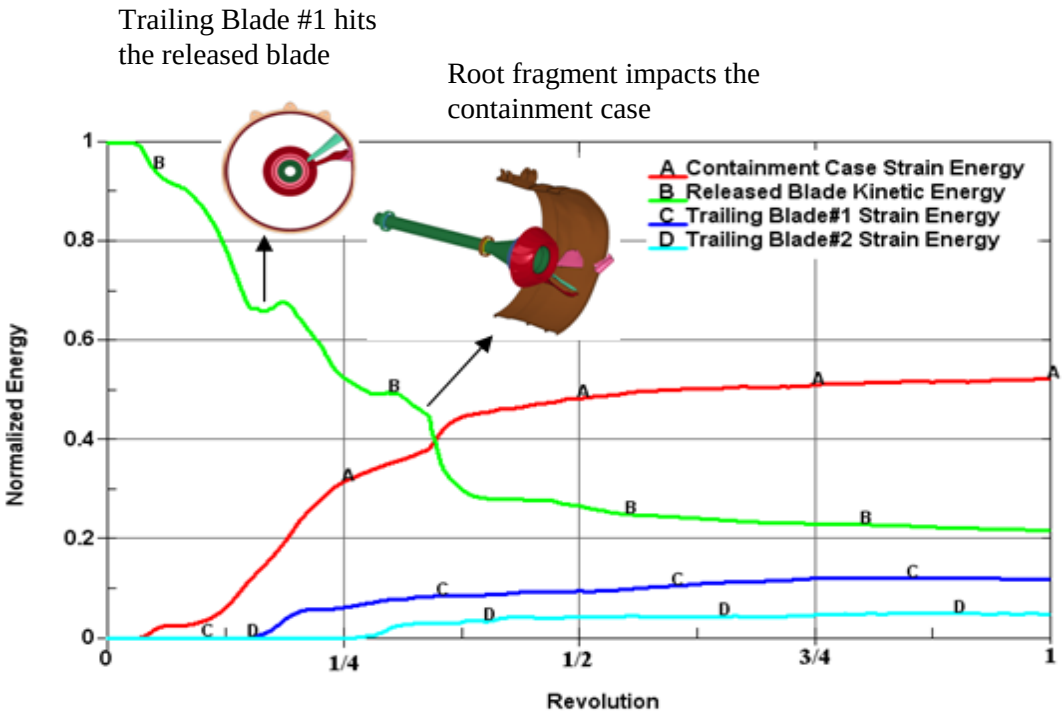

Figure 73. Normalized Kinetic Energy of the Released Blade and Normalized Strain Energy of the Containment Case, Trailing Blade #1, and Trailing Blade #2 (normalized with respect to initial kinetic energy of the released blade)

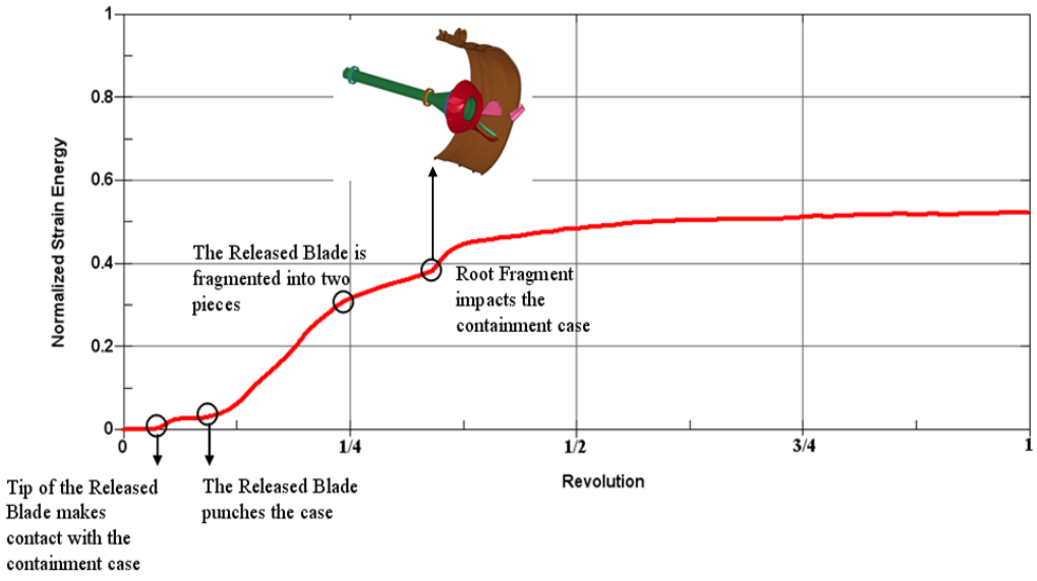

Figure 74. Normalized Strain Energy of the Containment Case (normalized with respect to initial kinetic energy of the released blade)

3.1.1.5 Velocity Analysis

Just before blade release, the velocity vector of the blade CG is fully tangential (Vtangential=V_0 and Vradial=0). Immediately following release, the blade CG moves tangentially while continuing to rotate about its CG at the prerelease fan rotational velocity. In the analysis, the blade CG is tracked relative to the fan's original CG, so the tangential blade trajectory has tangential as well as radial components (CG is moving radially away from the fan CG as the blade moves tangential to its original path).

During blade–case interaction, the velocity vector of the released blade's CG changes because of contact forces applied on the blade by the casing. These forces are responsible for fragmenting the blade tip and turning the velocity vector of the released blade CG from primarily tangential to a combination of tangential and normal to the case. Figure 75 shows the predicted time histories for the released blade CG radial (Vradial) and tangential (Vtangential) velocity components. With release of the blade, the radial velocity component increases linearly (kinematics of tracking the blade CG relative to the rotating coordinate system at the fan's CG). Analysis results demonstrate that the released blade reached the containment case in 0.3 ms. After that, the tangential velocity (Vtangential) decreases because of friction between the case and the released blade, and radial velocity increased linearly. At 1.2 ms, trailing blade #1 contacts the curled tip of the released blade and both components of velocity decrease. At 2 ms, the released blade breaks into two fragments with a corresponding sharp drop in tangential and radial velocity components. Around 2.2 ms, trailing blade #1 and trailing blade #2 hit the root fragment and feed additional kinetic energy to the fragment, therefore increasing the fragment's tangential velocity. At this time, the fragment's radial velocity has dropped to one tenth of the prerelease tangential velocity and is traveling in the opposite direction (Vradial = -0.1V_0). After the root fragment impacts the fan case, the tangential and radial velocity components decrease gradually over the remainder of the analysis.

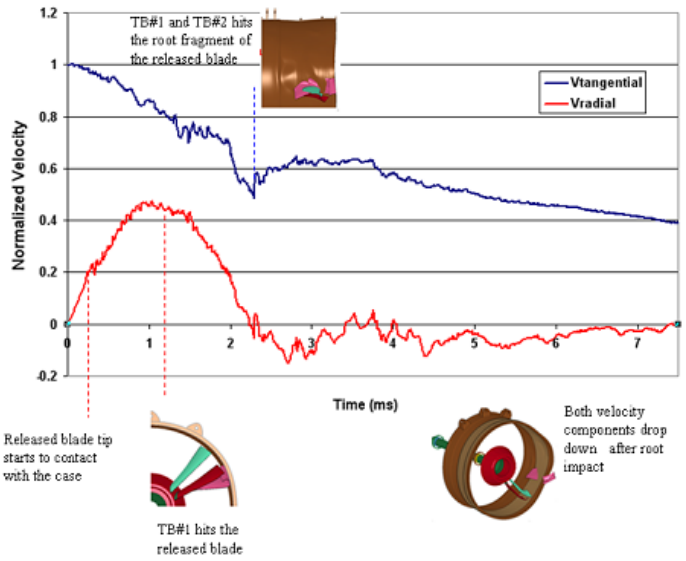

Figure 75. Velocity of the Released Blade Initial CG During Interaction With the Case (normalized with respect to initial velocity of the released blade)

3.1.2 Case Damage and Blade Breakup

To validate the case damage and blade breakup, results were compared to impact studies available in the public literature. Before proceeding, it must be noted that an engine fan blade-out event is a nonideal projectile impact, whereas most studies available in the literature focus on more ideal impact conditions. Goldsmith [9] reviewed a number of oblique impact tests and corresponding theoretical solutions. These results provide insight into the impact failure mechanism of engine containment structures. Containment of rotorblade fragments were also studied by Sarkar and Atluri [10] using the explicit dynamic nonlinear FE code LS-DYNA. Hagg and Sankey [11] conducted a number of tests to identify the failure stages in the containment case due to disc burst fragments. Lundin and Mueller [12] conducted a series of impact tests using titanium fan blade fragments fired against aluminum 2024 flat-panel targets to characterize uncontained engine events. Recently, failure response studies of aircraft engine containment panels impacted by titanium blade fragments were conducted by Wierzbicki and Teng [13]. As all these studies indicate, developing a better understanding of the impact failure mechanism would help improve the design of effective containment systems. In the typical FBO event, the containment case is the target material; ductility of the target material is an important parameter necessary to understand whether the casing may fail. However, the ductility of a material strongly depends on its stress state [14], so the projectile shape and orientation, projectile velocity, and target geometry are all important to determine the state of stress at impact. A fracture locus formulated in the space of the effective plastic strain to fracture and the stress triaxiality can be used to accurately describe material ductility [15, 16] during a nonlinear impact event. Stress triaxiality is defined by the ratio of the pressure (hydrostatic stress) to the equivalent Von Mises stress.

During an FBO event, the released blade impacts the fan case, losing velocity as it and the containment case deform. The released blade then increases velocity when impacted by the first trailing blade. Released blade velocity and kinetic energy are then lost as the release blade fragments and continues to make contact with the fan case and trailing blades. The impact force imparted by the released blade on the case deforms the containment structure, making a visible plastic bulge in the fan case. Analysis results predicted two main damage zones on the fan casing (see figure 76). The fan case experienced initial damage where the blade tip impacted the case and more significant secondary damage where the blade root impacted the case. The fan case was most highly stressed and experienced the greatest plastic deformation at the location of the second impact where the released blade root impacts the initial damage zone. It is important to understand the changing stress state during this plastic deformation to evaluate whether failure might occur during impact. To investigate this, the principal stresses and stress triaxiality of the most stressed elements in the fan case were determined in the time interval during which plastic deformation occurred. The maximum conditions were found to occur on the outer surface of the fan case where a state of biaxial tension was predicted with a minimum principal stress near zero, and maximum and second principal stresses simultaneously increasing in tension (see figure 77). The stress triaxiality plot for this element (see figure 78) shows triaxiality ranging between -0.6 and -0.7, which confirms the biaxial tension stress state during the plastic deformation.

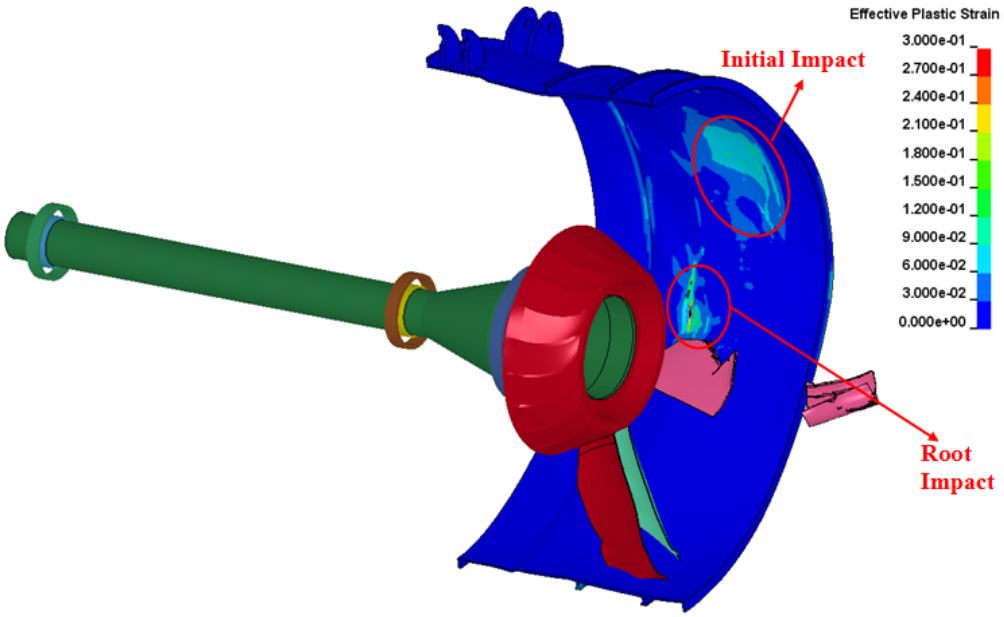

Figure 76. Main Damage Zones of the Containment Case

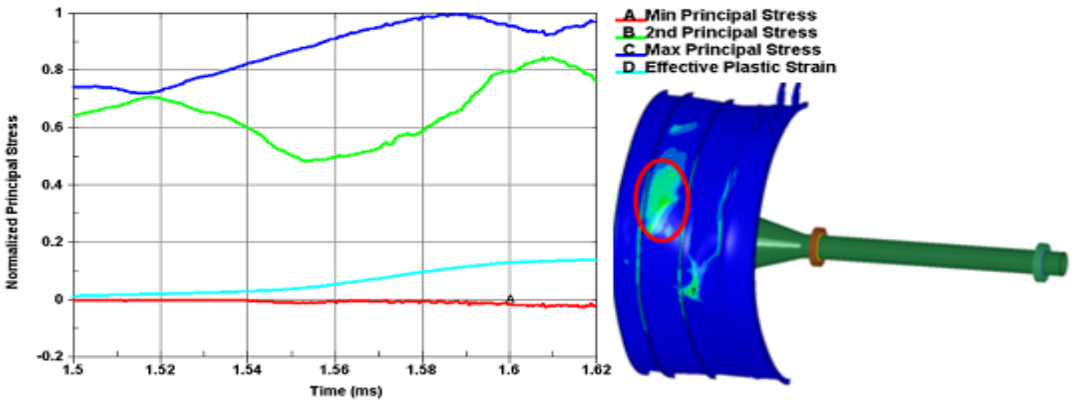

Figure 77. Normalized Principal Stresses of the Most Stressed Element on the Footprint of Initial Impact (outer surface of the containment case)

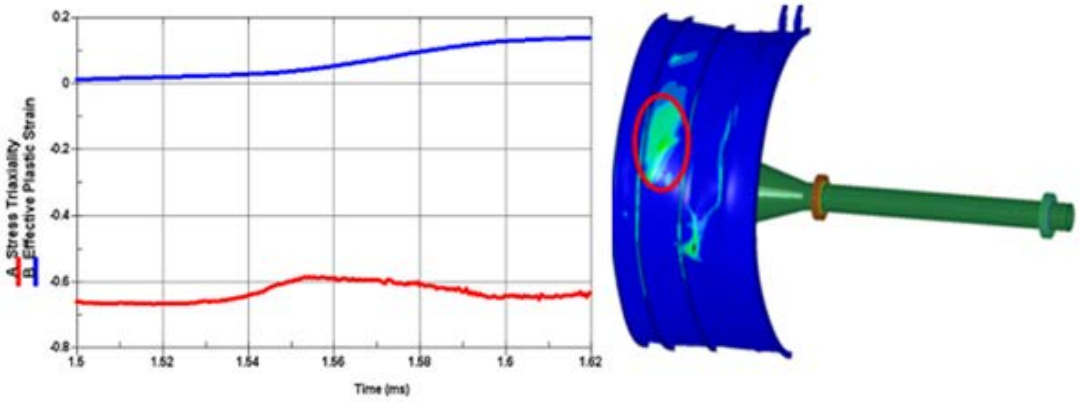

Figure 78. Stress Triaxiality of the Most Stressed Element on the Footprint of Initial Impact (outer surface of the containment case)

Secondary damage occurred in the root impact region where the sharp edge of the root fragment hit the casing. The sharp edge impacted with minimum yaw and created an intense shear stress over a small region of the fan casing. Figures 79 and 80 show damage to the containment case inner and outer surfaces at the footprint of the root impact. The sharp edge of the root fragment gouged the case inner surface and caused element failures (see figure 79). Significant plastic denting of the fan casing also resulted in element failures on the outer surface of the fan case. One of the failed elements on the outer surface was selected and the stress state during plastic deformation was investigated using principal stresses and stress triaxiality plots. Figure 81 shows that a state of biaxial tension was determined with the minimum principal stress near zero, and maximum and second principal stresses increasing in tension during plastic deformation. Stress triaxiality plots of the same element in figure 82 show the triaxiality to range between -0.6 and -0.7, which confirms the biaxial tension stress state during the plastic deformation. This indicates that the same stress state occurred on the outer surface of the fan casing, both at the initial impact zone and at the root impact zone.

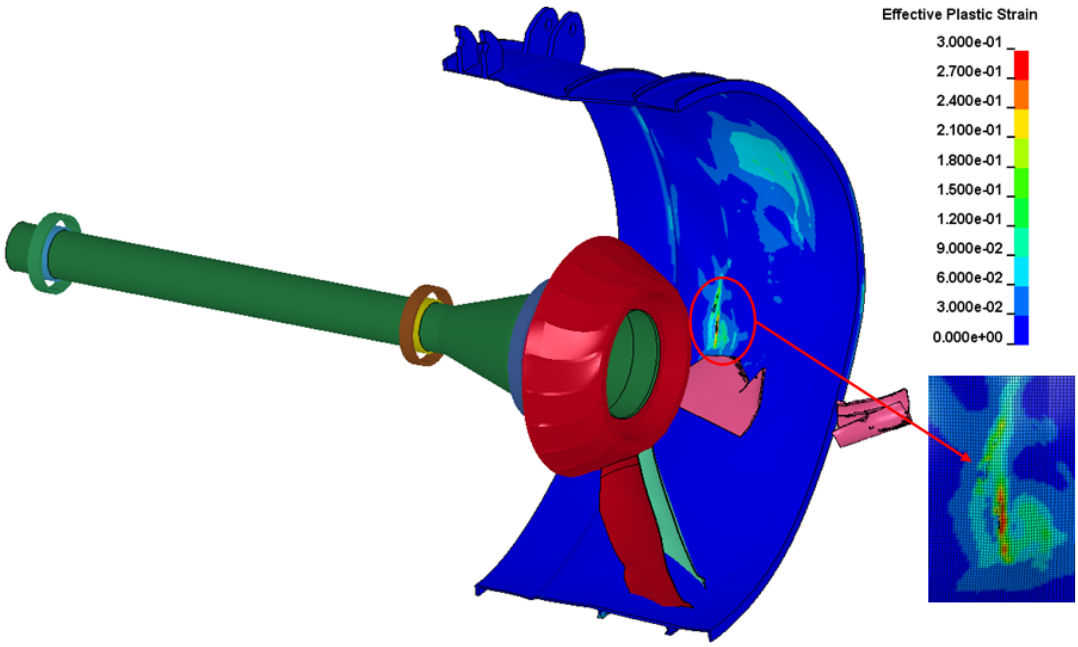

Figure 79. Damage of the Containment Case Inner Surface at the Footprint of the Root Impact

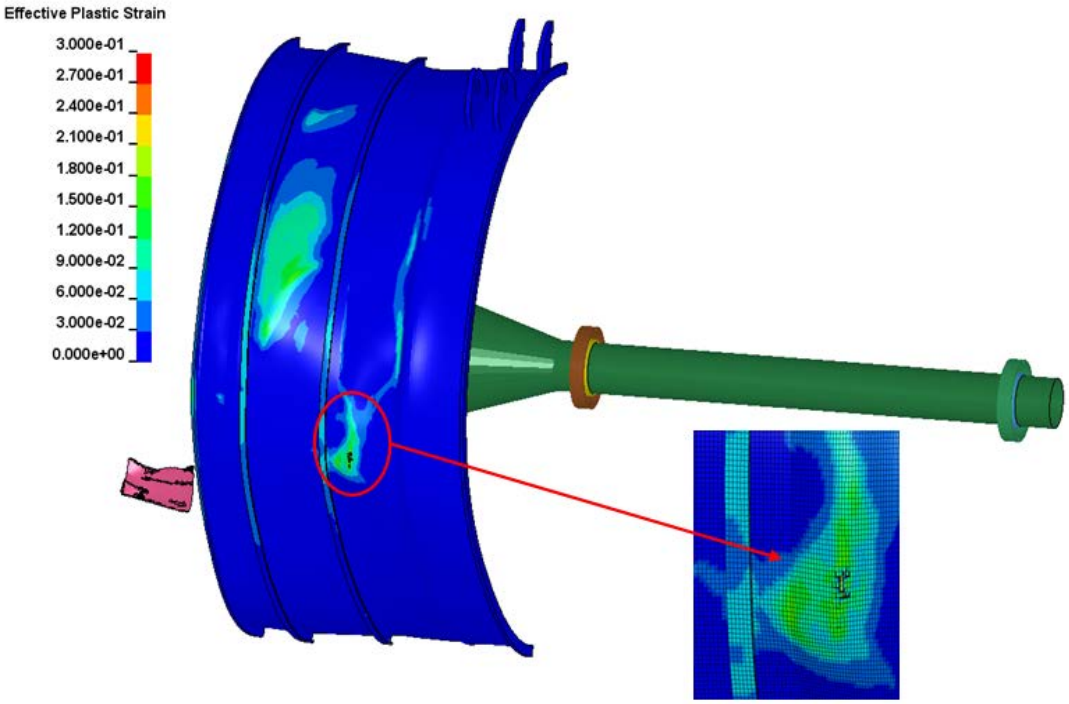

Figure 80. Damage of the Containment Case Outer Surface at the Footprint of the Root Impact

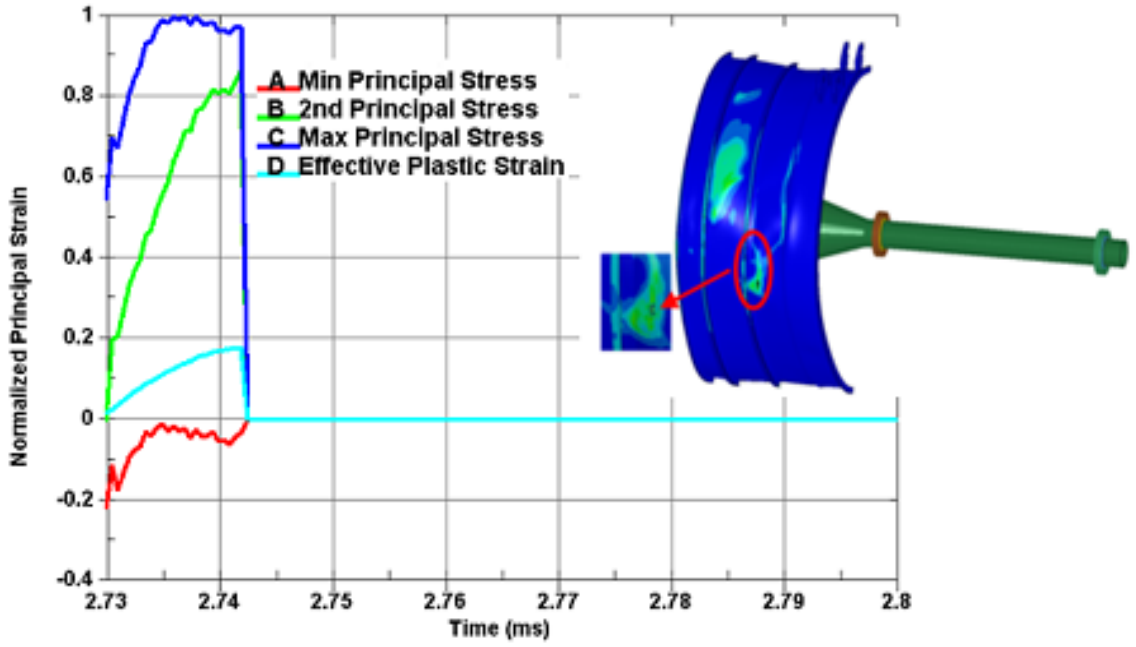

Figure 81. Normalized Principal Stresses of the Failed Element on the Footprint of Initial Impact (outer surface of the containment case)

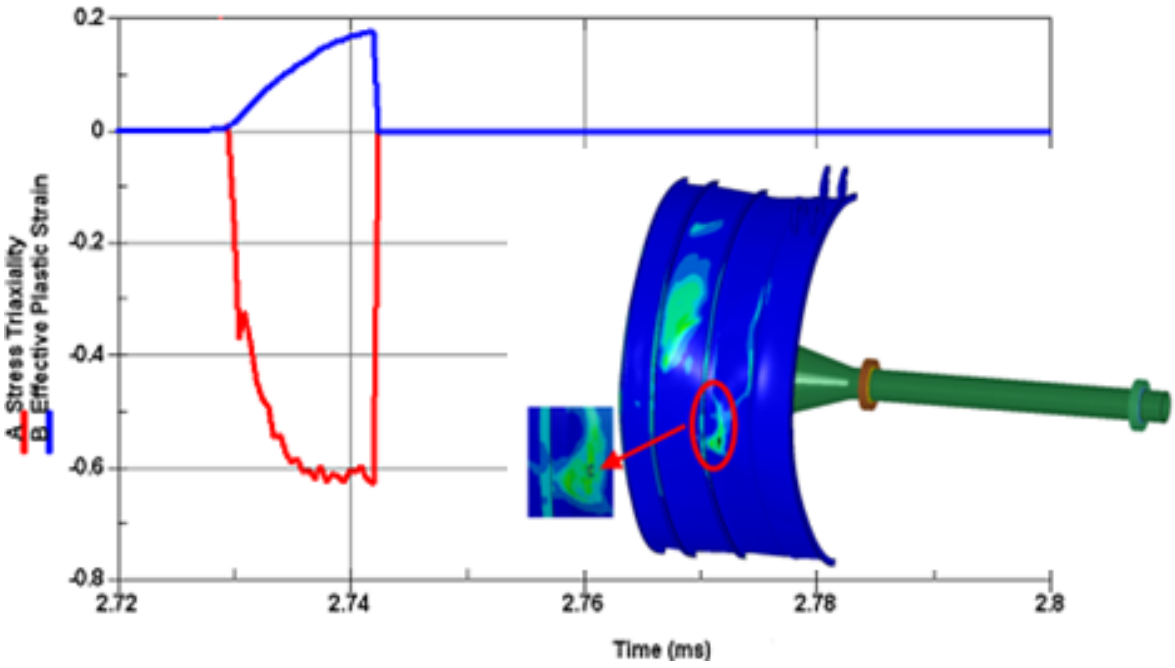

Figure 82. Stress Triaxiality of the Failed Element on the Outer Case Footprint of Initial Impact

Effective plastic strains in the most stressed elements during the initial and root impacts were compared in figure 83 to investigate strain rate effects. It was determined that plastic strain rates were 2500/s and 21,000/s for the initial tip and later root impact events respectively. It was

concluded that the root impact plastic strain rate was approximately eight times the initial impact plastic strain rate.

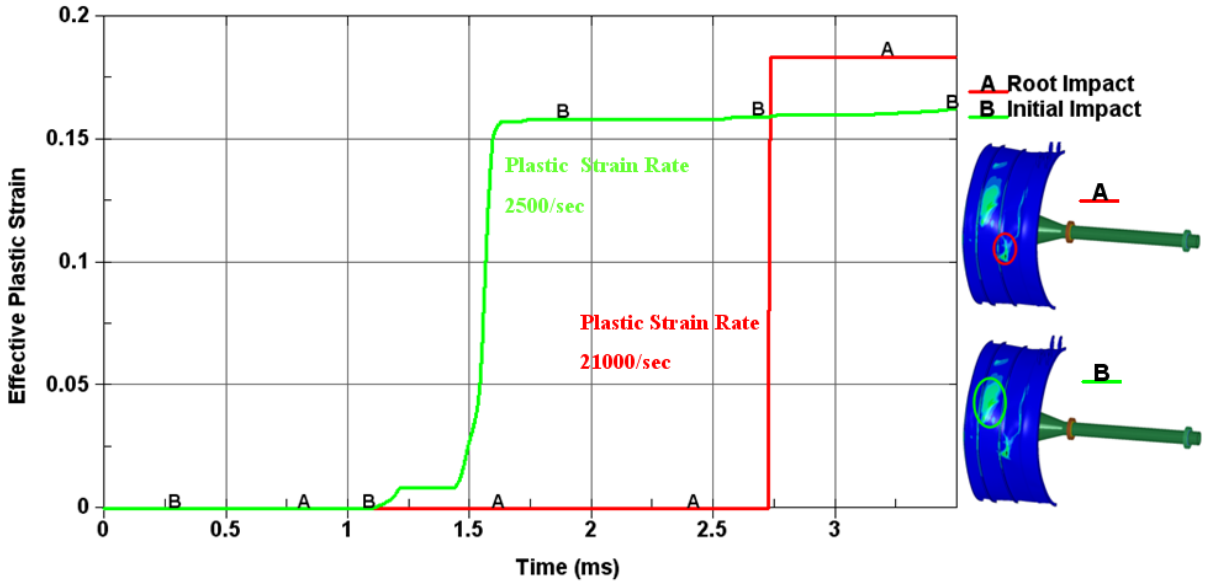

Figure 83. Comparison of the Effective Plastic Strains in the Fan Casing Impact Zones

Damage during the root impact was compared using different casing models with four and six elements through the containment thickness. Figure 84 shows that the maximum strain energy of the fan casing was 3% higher with six elements as compared to four elements through the thickness. The four-element model was determined to be stiffer and also estimated a lower effective plastic strain on the outer surface during the root impact (see figure 85).

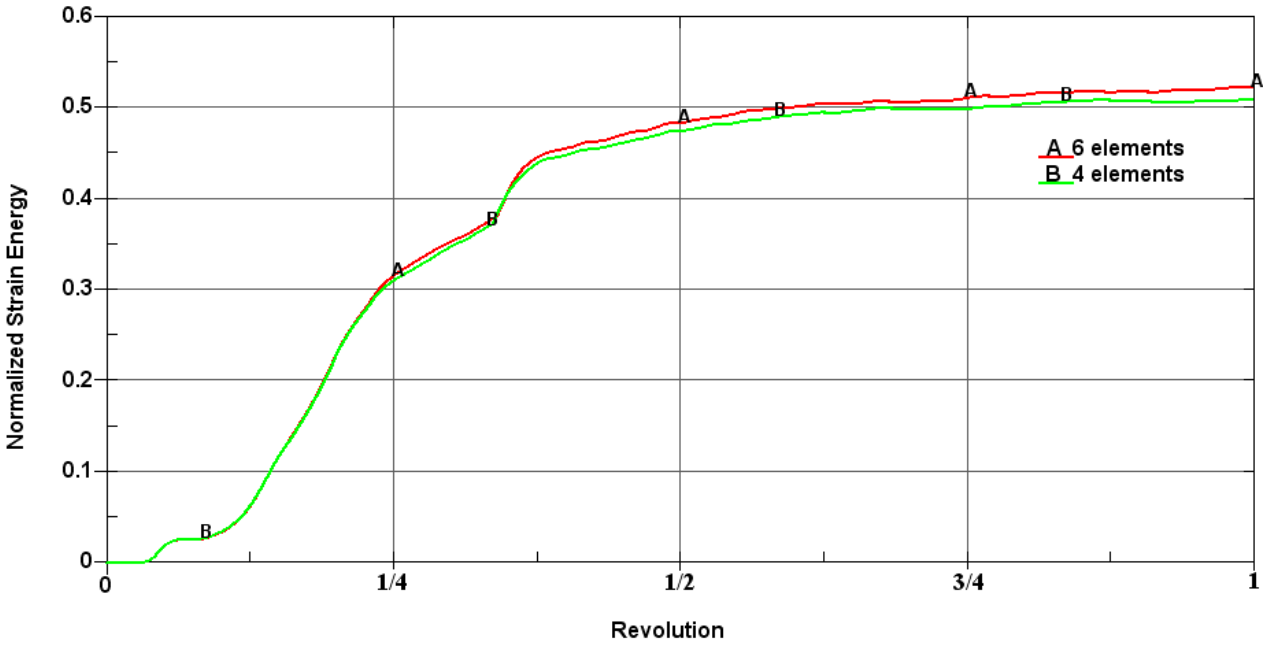

Figure 84. Effect of Through-the-Thickness Element Number on the Containment Case Normalized Strain Energy

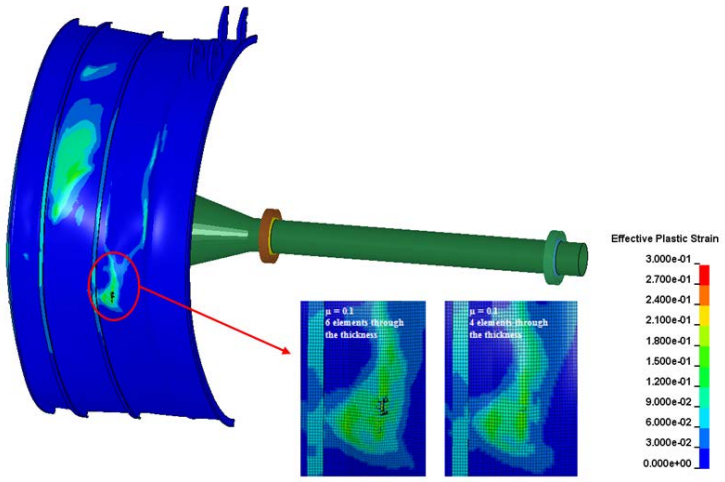

Figure 85. Effect of Through-the-Thickness Element Number on the Root Impact Footprint of the Fan Casing Outer Surface

Another parametric study was conducted to understand the effect of the Johnson-Cook material model damage parameters on predicted fan-casing damage. The LLNL-2 and LLNL-3 material models were developed from tests conducted on two different thickness target plates, so the intent was to assess whether there was an effect on the ability to predict containment case response. For consistency in the comparison, the two material models were compared using the containment case model with six elements through the thickness. As shown in figure 86, no outer surface element failure was predicted for the root impact dent when using LLNL-3, but outer surface elements failures were predicted for the same condition when using LLNL-2. This

result was expected because the LLNL-2 set has lower effective plastic strain at failure for the biaxial tension state as compared to the LLNL-3 set.

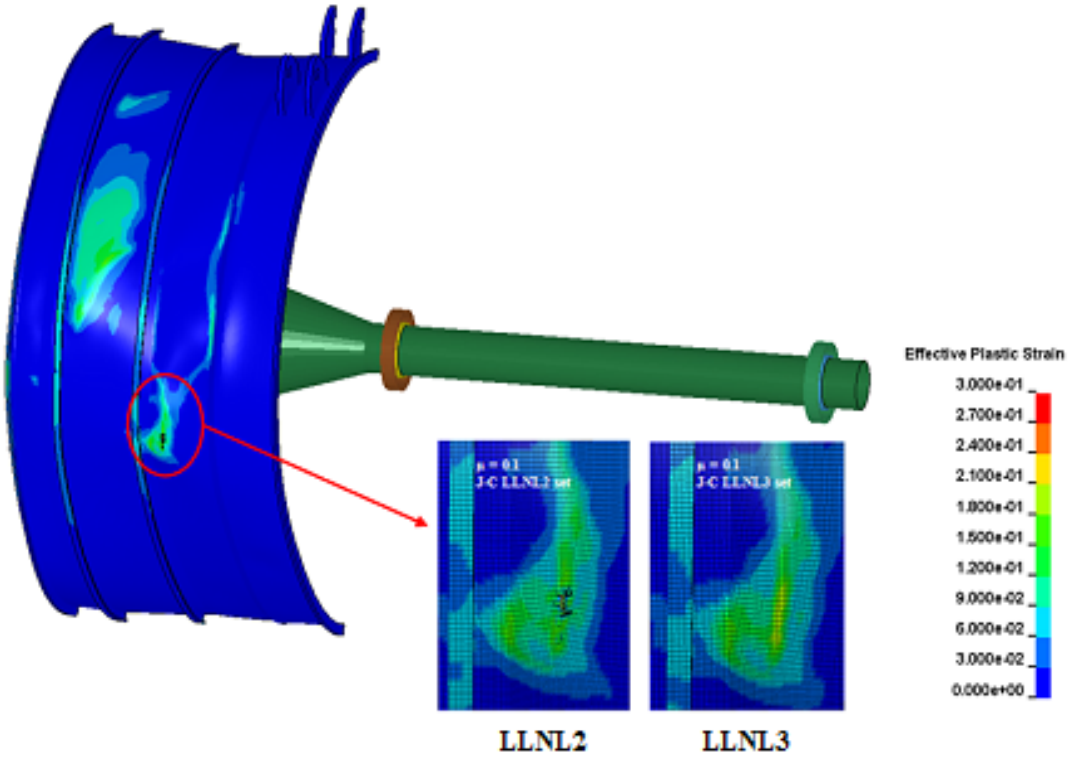

Figure 86. Effect of Johnson-Cook Damage Parameters on the Root Impact Footprint of the Fan Casing Outer Surface

The typical blade-release event includes several distinct stages: the release, release blade tip impact against the case, blade tip skating along the case (includes case and blade deformation), trail blade impact with the release blade, fragmentation of the release blade, impact of the blade root against the fan case, tumbling of blade fragments, and potential secondary trail blade impacts with fragments. Three different mesh configurations were investigated to evaluate the effect of mesh size on released blade fragmentation. For the first case, the in-plane element size was fixed to 0.1″ and three elements were used through the thickness. For the second case, the model was modified to use four elements through the thickness. For the third model, the in-plane element size was reduced to 0.075″ in the blade breakup zone and four elements were used through the thickness (see figure 87). As shown in figure 88, the first two models predicted partial tearing in the same proximity, but neither model predicted the blade would fragment into two pieces. The third model predicted primary damage to occur in the same physical location and also predicted that the blade would fragment, liberating the upper 1/3 panel (see figures 88 and 89).

(a) (b)

Figure 87. Mesh Details of the Released Blade: (a) In-Plane Element Size 0.1″ x 0.1″ and (b) Modified In-Plane Element Size in Blade Breakup Zone, 0.075″ x 0.075″

Figure 88. Effect of Element Size on the Blade Breakup

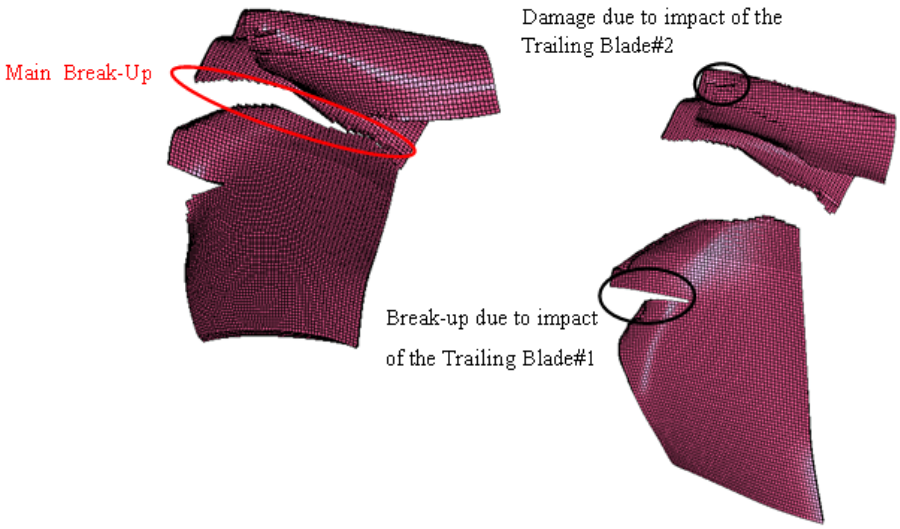

Figure 89. Details of the Released Blade Breakup Zones

Next, two different material models were exercised to understand the effect of material failure modeling on the released blade breakup. The material models were the rate-dependent Piecewise Linear Plasticity model with constant effective plastic strain at failure and the Johnson-Cook material model where failure strain was dependent on stress triaxiality and strain rate. For the rate-dependent Piecewise Linear Plasticity model, failure strain values 0.2, 0.18 and 0.15 were investigated. The in-plane element size 0.075″ was used in the blade break up zone, and four elements were used through the thickness. These models predicted differences in the main blade breakup and fragmentation (tip and root fragment), although failure due to trailing blade impact was captured well in all cases (see figure 90). The rate-dependent Piecewise Linear Plasticity model with failure strain 0.2 was able to capture the main damage zone at the outer third (tip) of the blade span as the Johnson-Cook model predicted, but no fragmentation occurred in this model because the failure strain was constant and set to 0.2. The release blade fragmentation was captured at the outer third (tip) of the blade span using the rate-dependent Piecewise Linear Plasticity model with a constant effective plastic strain at failure of 0.18. In this case, blade breakup and fragmentation were similar to the Johnson-Cook model. It was also determined that when effective plastic strain at failure was lowered to 0.15, the fragmentation zone shifted to the outer one-sixth (tip) of the released blade span.

Figure 90. Effect of Material Model on the Blade Breakup

After verifying that LS-DYNA was correctly predicting the basic sequence of events from blade release through fragmentation of the outer third of the blade, a more detailed investigation was undertaken to study the variables that affect the accurate prediction of this nonlinear plastic deformation event. During initial contact between the blade and case, the blade begins to deflect and plastic curling occurs at the blade tip. Next, plastic bending occurs in the main breakup zone while the blade is plastically deforming the fan casing. Material failure in the main breakup zone starts on the tensile side of the plastically bent section. To ensure a good prediction, it is critical to understand the stress state in this zone so that you can accurately evaluate the associated failure condition. To accomplish this, the analyst needs to evaluate the principal strains and stress triaxiality of what may become the failed elements in this zone, starting from the time when plastic deformation initiates. As shown in figure 91, a state of plane strain tension was predicted based on the second principal strain being near zero ($\varepsilon_2=0$) while maximum and minimum principal strains are equal in magnitude, but having opposite signs ($\varepsilon_1 = -\varepsilon_3$). The stress triaxiality plot of the same element in figure 92 shows that stress triaxiality during plastic deformation varies between -0.55 and -0.6. This behavior was observed in the stress triaxiality plots for all the elements that failed in this zone; therefore, it confirms that a state of plain strain tension existed at the initiation of material failure in the main breakup zone.

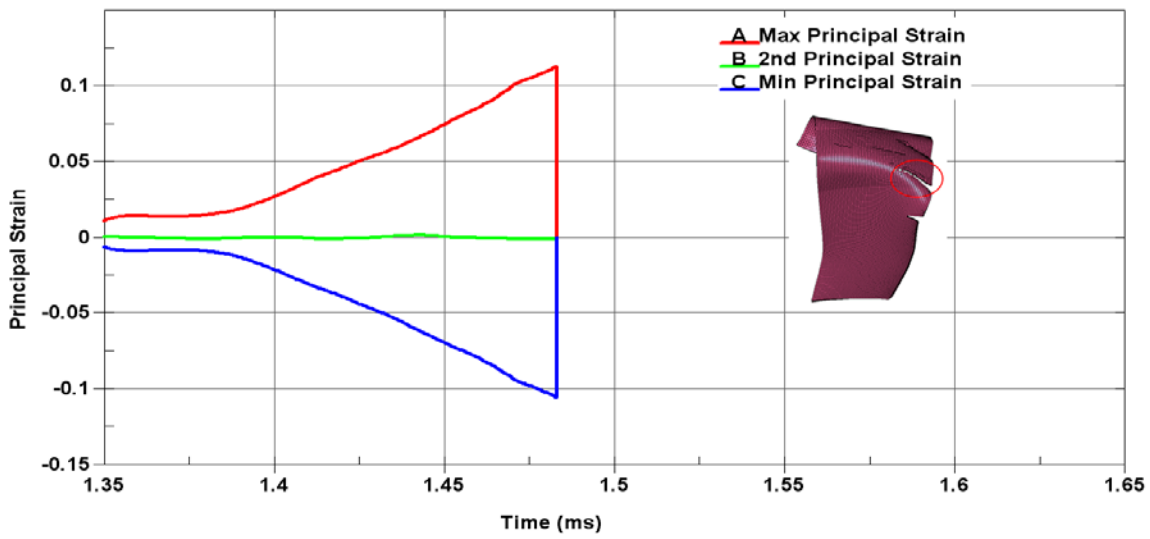

Figure 91. Principal Strains at the Blade Breakup Zone

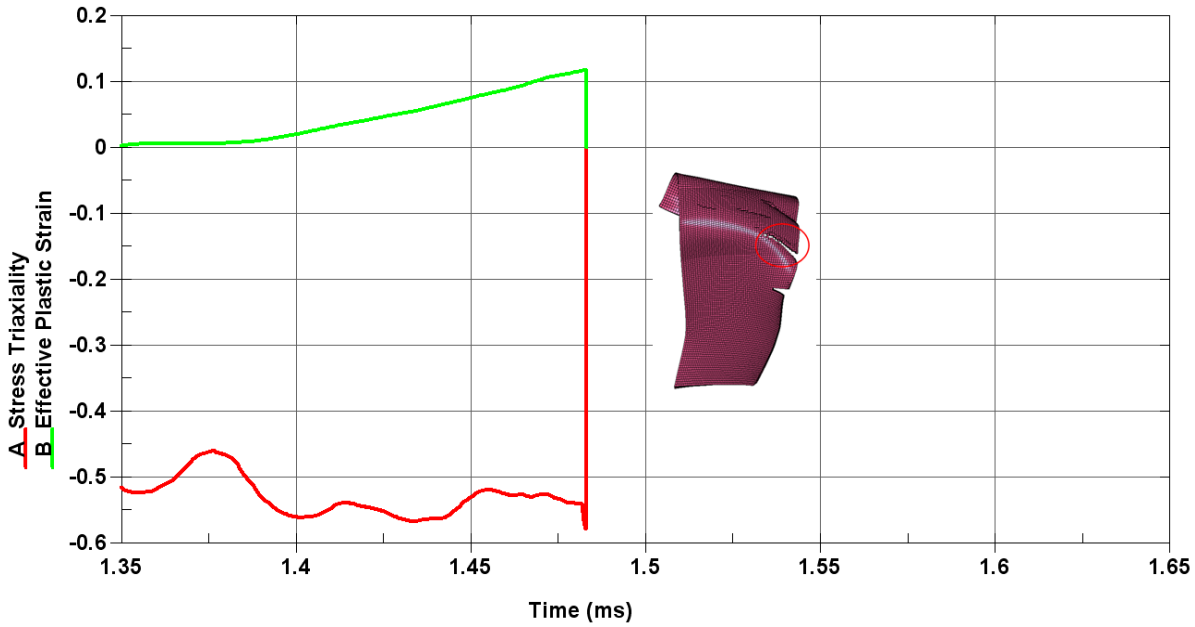

Figure 92. Stress Triaxiality at the Blade Breakup Zone

3.1.3 Effect of Friction Coefficient on the Blade–Case Interaction

When the release blade impacts the case, its tangential velocity wants to make it skate along the case surface. The coefficient of friction between the blade tip and case is one of the important variables that affect initial blade tip curl, subsequent blade breakup, and case damage during containment analysis. Therefore, sensitivity of the FBO simulation results to the blade-case friction coefficient needs to be addressed. In this work, the classical isotropic coulomb friction model with constant coefficient was prescribed in LS-DYNA and three different cases were

evaluated to address the effect of the friction coefficient (μ) in the containment analysis, as follows:

- Case 1: μ = 0.0
- Case 2: μ = 0.1
- Case 3: μ = 0.2

Figures 93 and 94 show the released blade kinetic energy plotted against the containment case strain energy and released blade strain energy, respectively, for each of the three friction coefficient cases. Also provided on each plot is the frictional energy loss due to the released blade-containment case interaction. The energy values are normalized with respect to the initial kinetic energy of the released blade for each friction case. Increasing the blade-case interaction friction coefficient decreases the kinetic energy in the released blade as compared to the frictionless case. At the end of the first revolution, the kinetic energy for the frictionless case was 35% of the initial release blade kinetic energy. When friction was added, the kinetic energy of the release blade after one revolution was 21% and 12% of the initial kinetic energy for friction cases 2 (μ = 0.1) and 3 (μ = 0.2), respectively. Figures 93 and 94 also show that strain energy in the containment case is 59% of the initial kinetic energy of the released blade at the end of one revolution for the frictionless case, and this decreases to 53% and 49% for friction cases 2 (μ = 0.1) and 3 (μ = 0.2). For all friction cases, the release blade fracture location was at a 2/3 span. The primary difference observed among the friction cases was in the damage to the tip fragment (outer 1/3 span of the released blade). During the first stage of the blade-case interaction, curling occurs at the tip of the released blade when it contacts the case. The extent of tip curling was observed to increase as the friction coefficient increased (frictionless case exhibited the least curing, case three the most). The resulting difference in curling changed the contact area of the tip fragment leading to differences in the damage of the released blade tip fragment. This fact was supported by the released blade strain energy plot in figure 94. In this figure, it was shown that the strain energy of the released blade in the first quarter revolution was slightly higher when friction was included in the analysis.

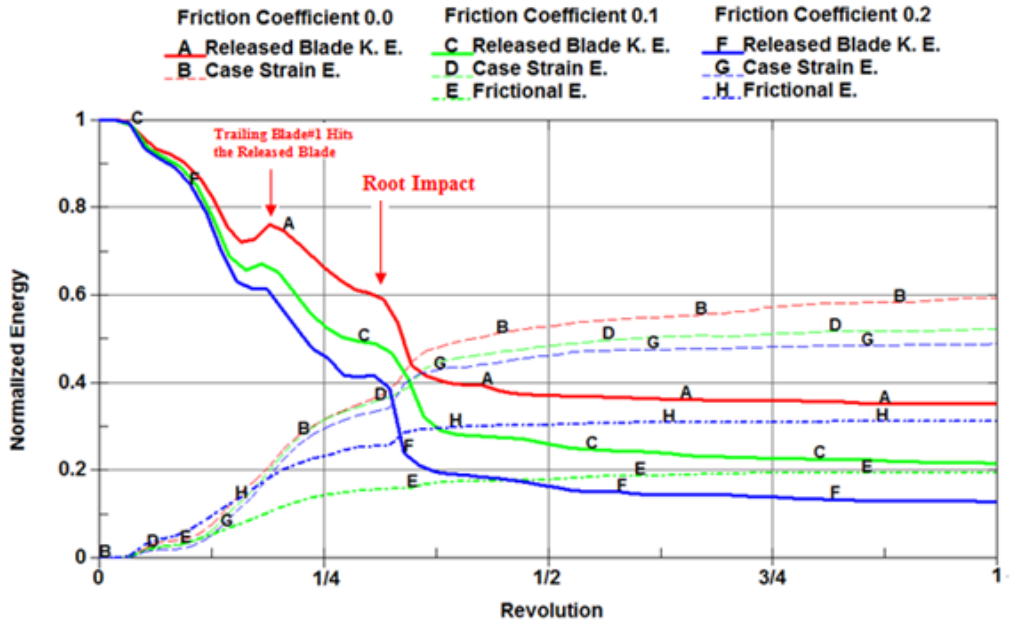

Figure 93. Effect of Friction Coefficient on the Containment Case Strain Energy and Released Blade Kinetic Energy (normalized with respect to initial kinetic energy of the released blade)

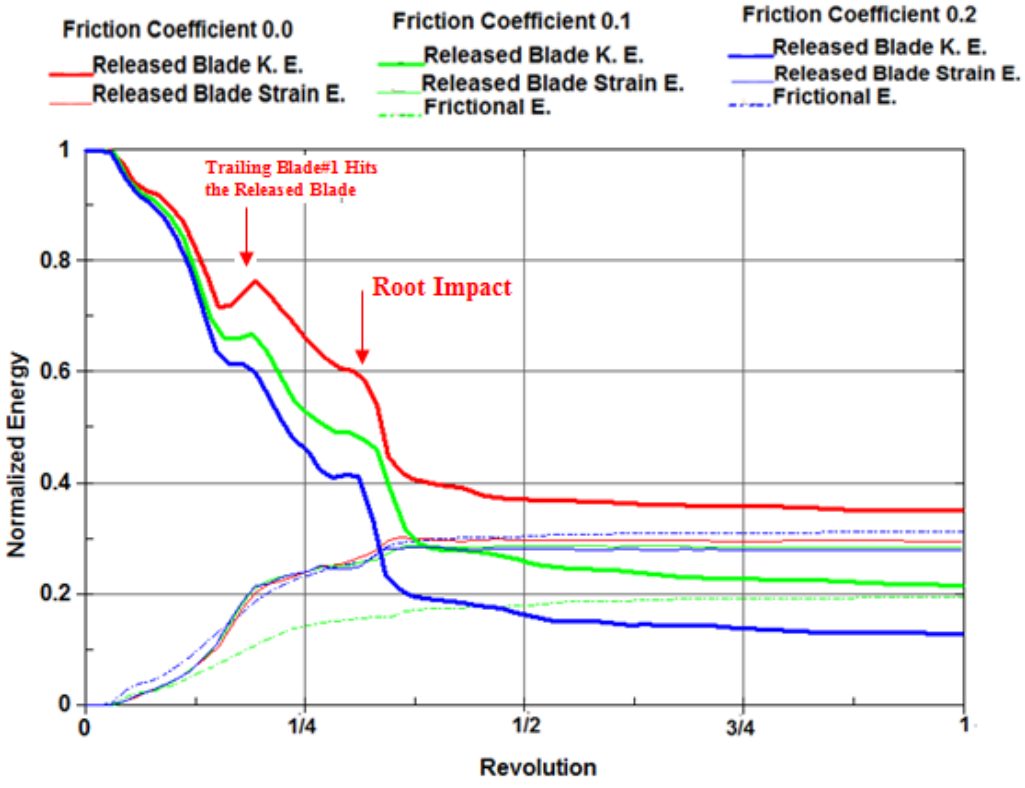

Figure 94. Effect of Friction Coefficient on the Released Blade Strain Energy and Kinetic Energy (normalized with respect to initial kinetic energy of the released blade)

It was also found that the friction coefficient not only affected kinetic energy of the released blade, but also changed its orientation and impact angle during interaction with the case. As shown in figure 95, obliquity of the 2/3 span of the released blade varied with the friction coefficient at the initial impact where main blade breakup occurred. Despite having the lowest final release blade kinetic energy of the three friction cases considered, friction case 3 ($\mu = 0.2$) was the only condition for which the initial blade impact punctured the containment case. This result appears to indicate that the obliquity angle during impact of the fragment is an important factor in determining whether the fan casing will be penetrated. A similar effect was observed for the root fragment hammering impact in the frictionless case. As shown in figure 96, the impact angle of the root fragment presents the sharp edge of the blade to the casing during the frictionless case, while in the friction cases, the blade presents a more blunt contact geometry.

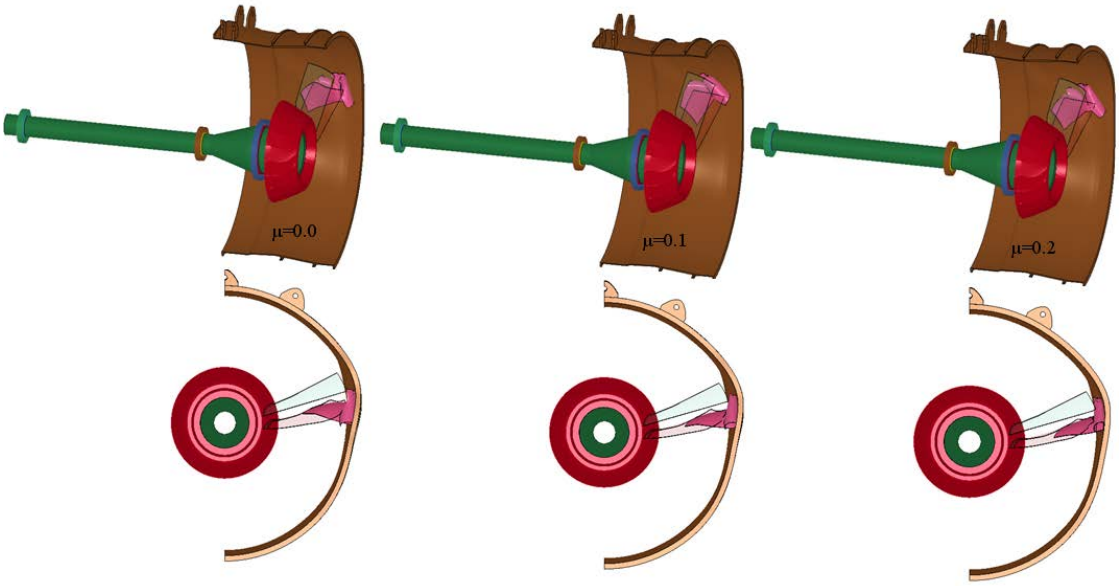

Figure 95. Effect of Friction Coefficient on the Released Blade Impact Angle
(case deflections are scaled for visualization)

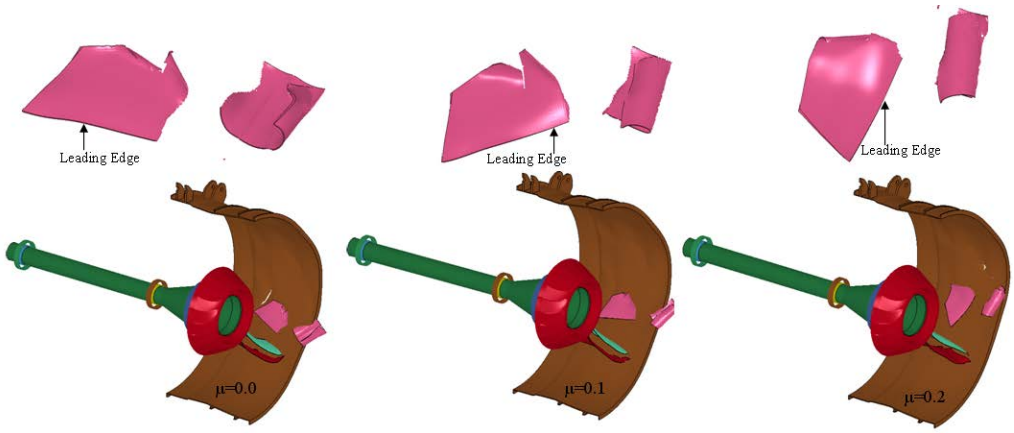

Figure 96. Effect of Friction Coefficient on the Blade Breakup and Case Damage

Local perforations occurred on the fan casing at case 1 and case 3 because of root hammering impact and initial impact of the 2/3 span of the released blade, respectively. A parametric study was conducted to understand the effect of Johnson-Cook material model parameters on these two cases. The LLNL-2 and LLNL-3 material set comparison was done using the containment case model with six elements through the thickness. As shown in figures 97 and 98, no local perforation and element failure predicted with the LLNL-3 material set in contrast to damage with the LLNL-2 set; this is attributed to the higher effective plastic strain at failure values in LLNL-3 compared to LLNL-2 for stress states experienced during impact on the fan casing.

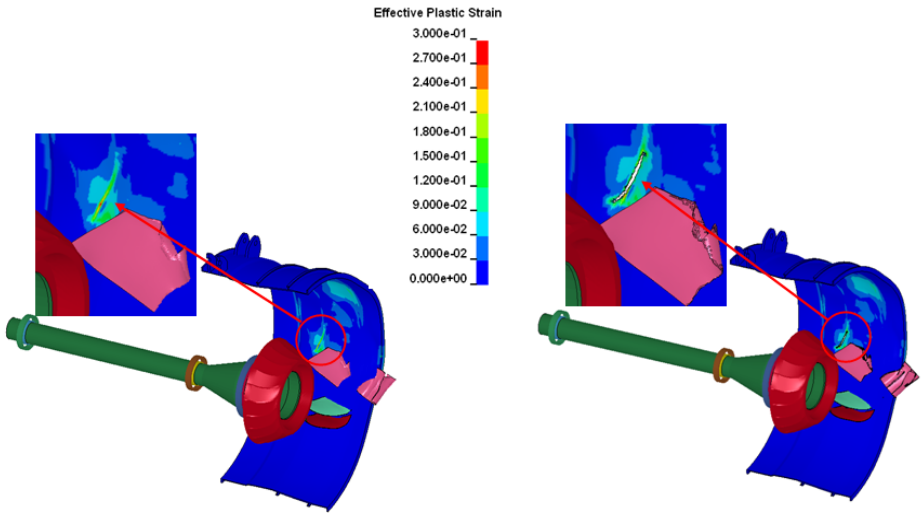

(a) (b)

Figure 97. Effect of Johnson-Cook Damage Parameters (a) LLNL-3 and (b) LLNL-2 on the Containment Case Damage for Case 1 ($\mu = 0.0$)

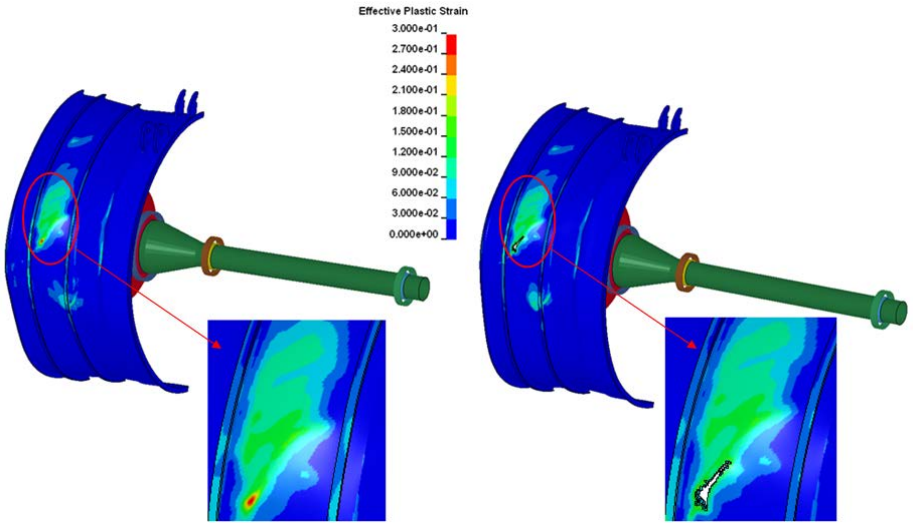

(a) (b)

Figure 98. Effect of Johnson-Cook Damage Parameters (a) LLNL-3 and (b) LLNL-2 on the Containment Case Damage for Case 3 (μ = 0.2)

4. FBO ANALYSIS—FULL MODEL

4.1 SIMULATION OF THE FAN BLADE-OUT EVENT—FULL-FAN RIG MODEL (PHASE 2)

All FE simulations were completed with version 971R4 of LS-DYNA MPP double-precision solver. The computations were performed on an IA64 supercomputing platform using the Linux operating system. Table 21 shows computational times for a three-revolution simulation of the rotor using different modeling schemes and computational platforms.

Table 21. Full-Fan Rig Model LS-DYNA Run Chart

Model	DYNA release version	Platform Operating System	Number of CPU	Run time (3 rev)
Casing-shell elements, dynamic relaxation model	Ls971sR4	IA64 System Linux 2.4.21	12	33 hours
Casing-brick elements, dynamic relaxation model	Ls971sR4	IA64 System Linux 2.4.21	12	140 hours
Casing-shell elements, initial stress model*	Ls971sR4	SGI system IRIX64 6.5	8	208 hours
Casing-brick elements, initial stress model*	Ls971sR4	IA64 System Linux 2.4.21	12	122 hours
Casing-shell elements, dynamic relaxation model	mpp971dR4.2.1	IA64 System Linux 2.4.21	10	23 hours
Casing-brick elements, dynamic relaxation model	mpp971dR4.2.1	IA64 System Linux 2.4.21	10	120 hours
Casing-shell elements, initial stress model*	mpp971dR4.2.1	IA64 System Linux 2.4.21	24	10 hours
Casing-brick elements, initial stress model*	mpp971dR4.2.1	IA64 System Linux 2.4.21	24	38 hours

The LS-DYNA energy data, which is printed in the glstat files, provides a useful check on an analysis to determine the correctness and stability of the numerical simulations. As shown in figure 99, total energy of the system was constant throughout the simulation. Internal energy, which includes strain energy due to elastic and plastic deformation, increases during the structural deformation of components. Sliding interface energy shows contact energy in the system. When friction is included in a contact definition, positive contact energy is to be expected. Sliding interface energy was positive throughout the analysis (see figure 99).

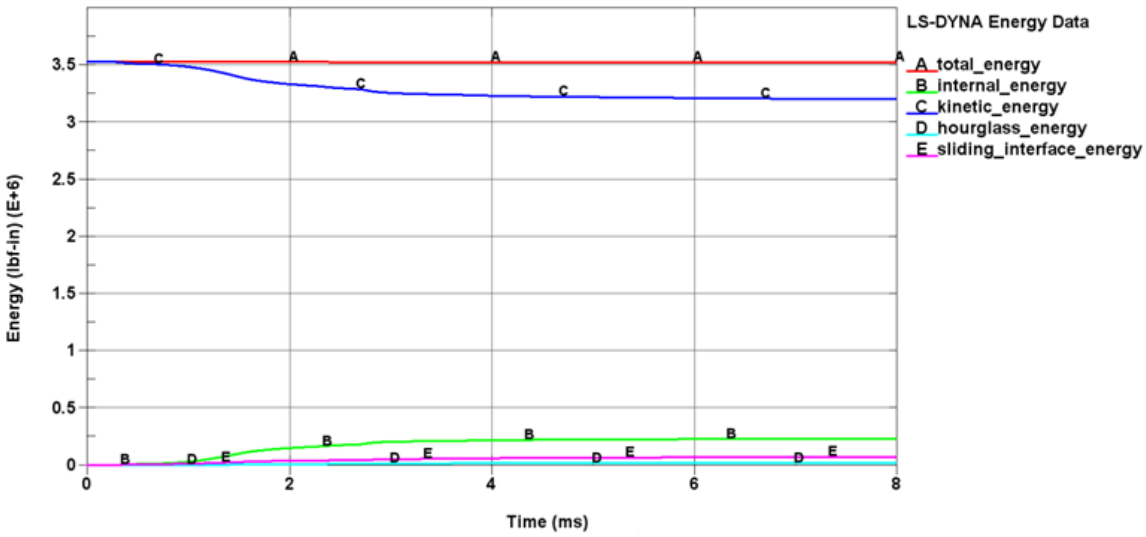

Figure 99. The LS-DYNA Energy Data

Hourglass energy is the indicator of nonphysical deformation modes associated with reduced integration elements. Hourglass energy on the order of less than 10% of the maximum strain energy is a commonly accepted upper limit for numerical stability. Figure 100 shows the hourglass energies of the released blade and containment case were within allowable limits.

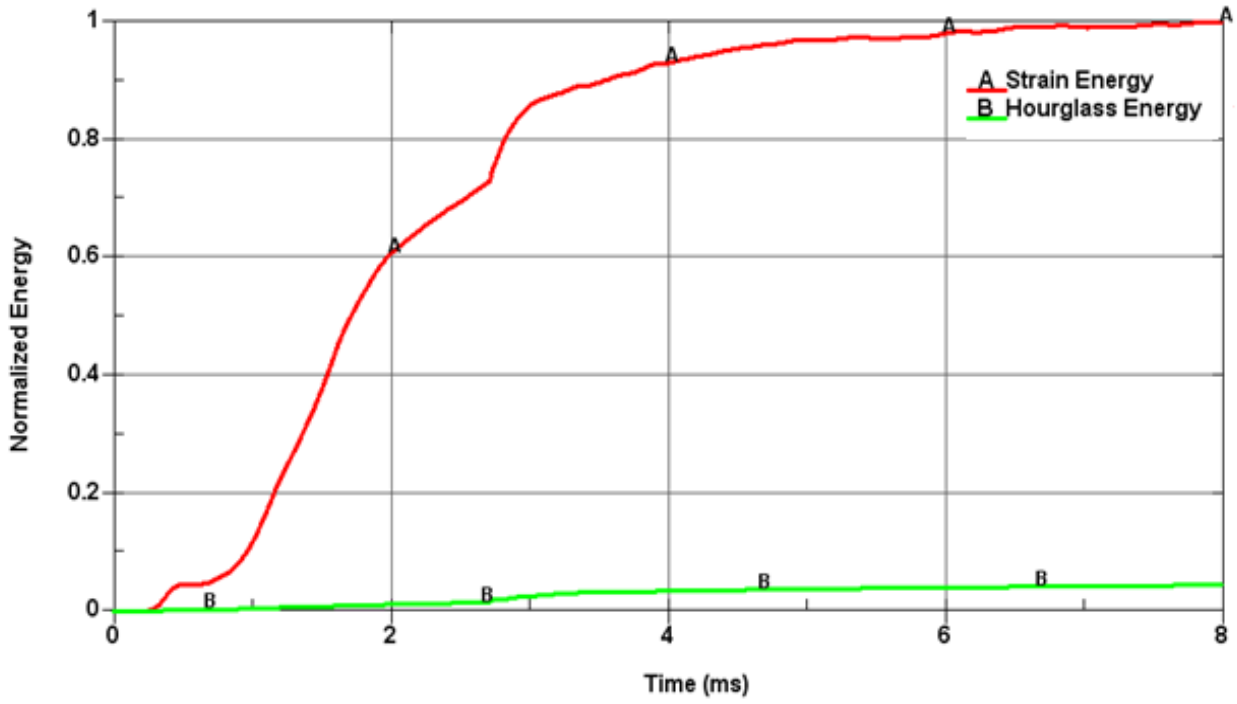

(a)

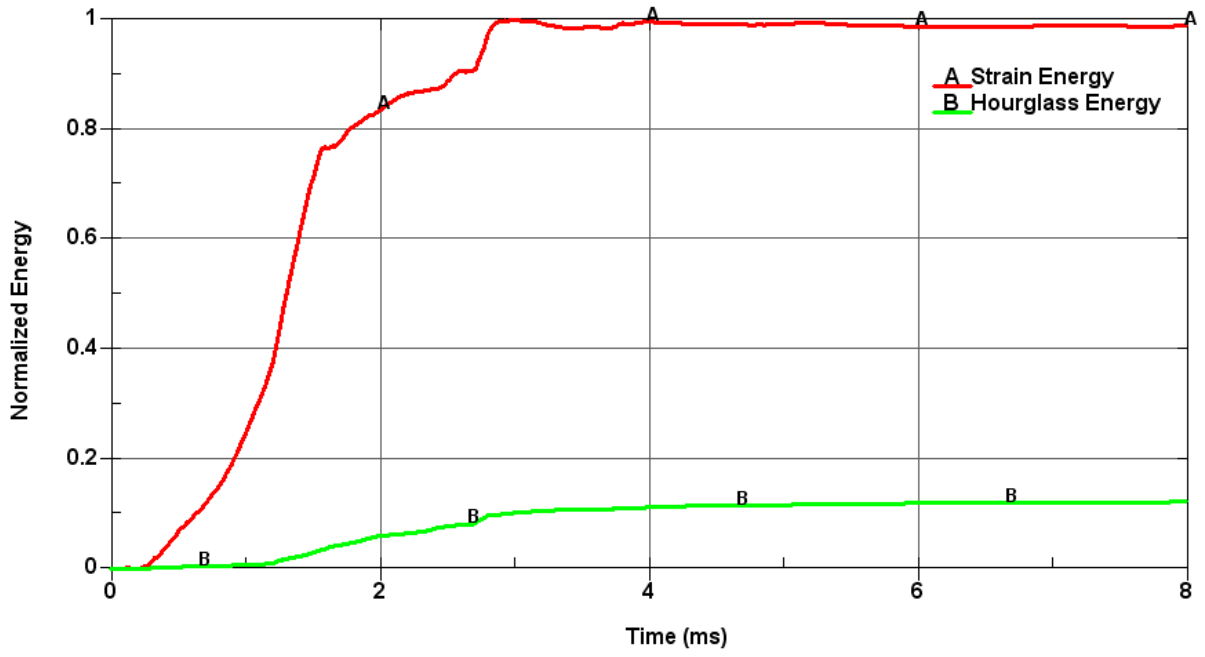

(b)

Figure 100. Normalized (with respect to maximum strain energy) Hourglass Energies for the (a) Containment Case and the (b) Released Blade

4.2 DISTINCT PHASES OF THE BLADE–CASE INTERACTION OF FULL-FAN RIG MODEL

An FBO simulation using the full-fan rig model was run for three revolutions following blade release. In typical engine FBO studies, analyses are conducted at various release clock angles to understand the effect of release angle location on system dynamic response. In this study, the blade was released at the 1 o'clock position (forward looking aft). The release angle for the analysis can be changed by adjusting the erosion time of the release blade root elements. At redline speed, one revolution of the fan occurs in 7.66 ms, so incrementing the erosion time in appropriate fractions of the time it takes to make one revolution allows the analyst to time the release at any clock angle. In the first phase of containment, the initial tip impact of the released blade occurs, followed at 1.8 ms by bending of the outer third of the released blade and bulging of the main containment zone of the fan case. Immediately following, trailing blade #1 collides with the released blade root section and increases kinetic energy in the released blade. At 2.2 ms, trailing blade #2 comes into contact with trailing blade #1 and the released blade's tip buckles. At 2.9 ms, the released blade's root section makes a hammering impact on the containment case and damages the containment zone at a higher strain rate as compared to the initial impact. During these events, the CG of the fan rotor-disk system shifts to the side opposite the released blade, causing the fan to rub on the case. Because of the blade tip rubs, the maximum stress points in the rubbed blades shifts to the blade tip from root. This shift in blade stress and loading conditions occurs between 2.9 ms and 8 ms (see figures 101 and 102).

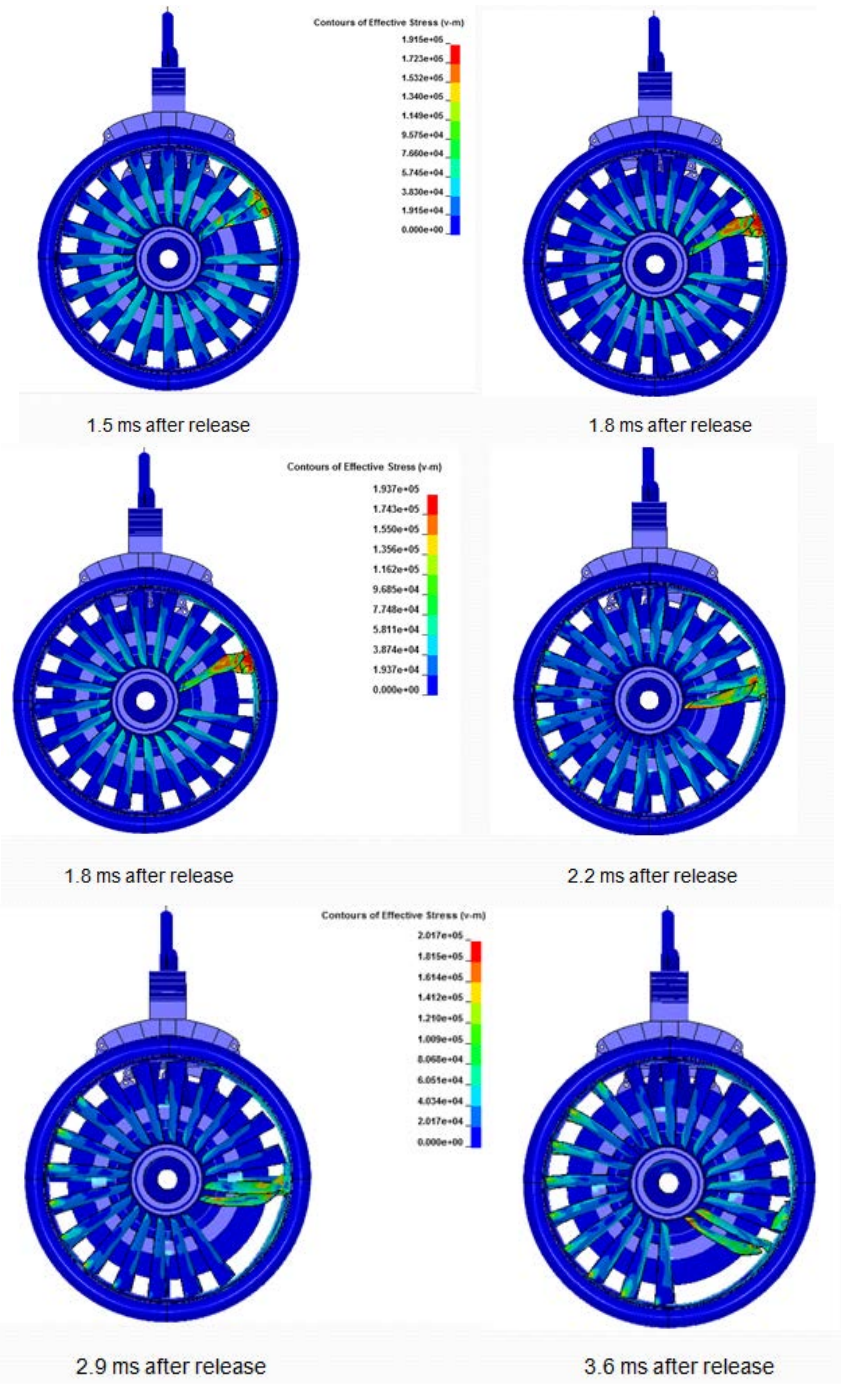

Figure 101. Phases of the Fan Blade–Case Interaction

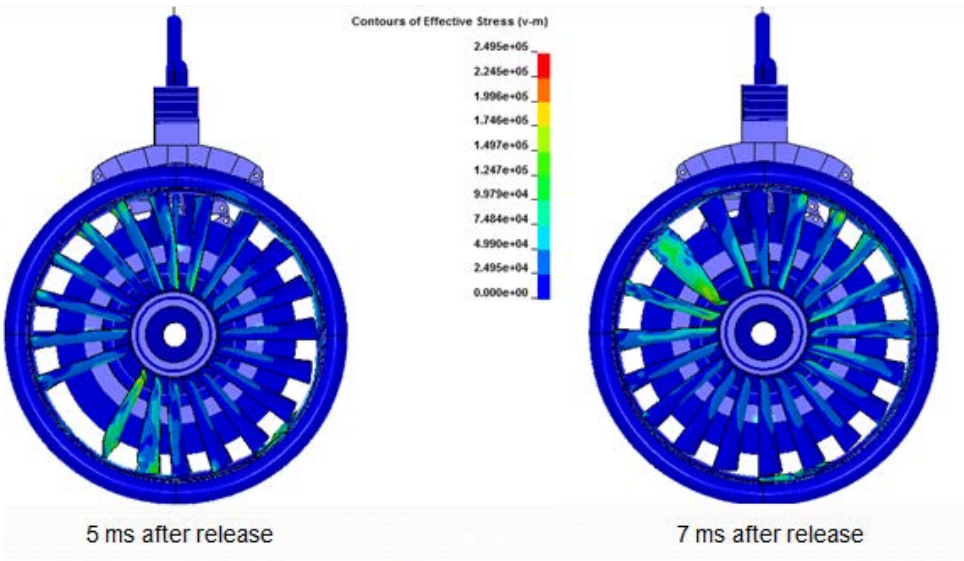

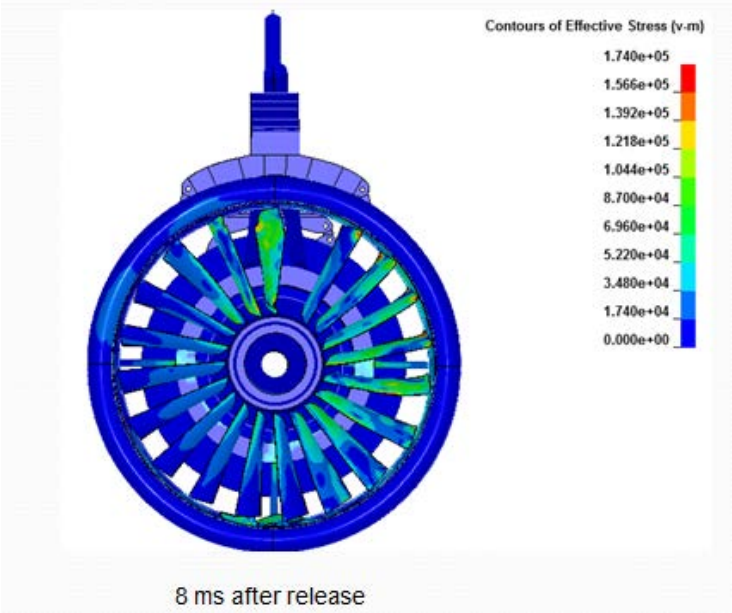

Figure 102. Phases of the Fan Blade–Case Interaction

4.3 CONTAINMENT CASE DAMAGE

Damage to the metallic containment case often occurs in three distinct zones or stages. The first damage zone is local damage at the site where the released blade tip impacts the case, as shown by the small outdent in figure 103.

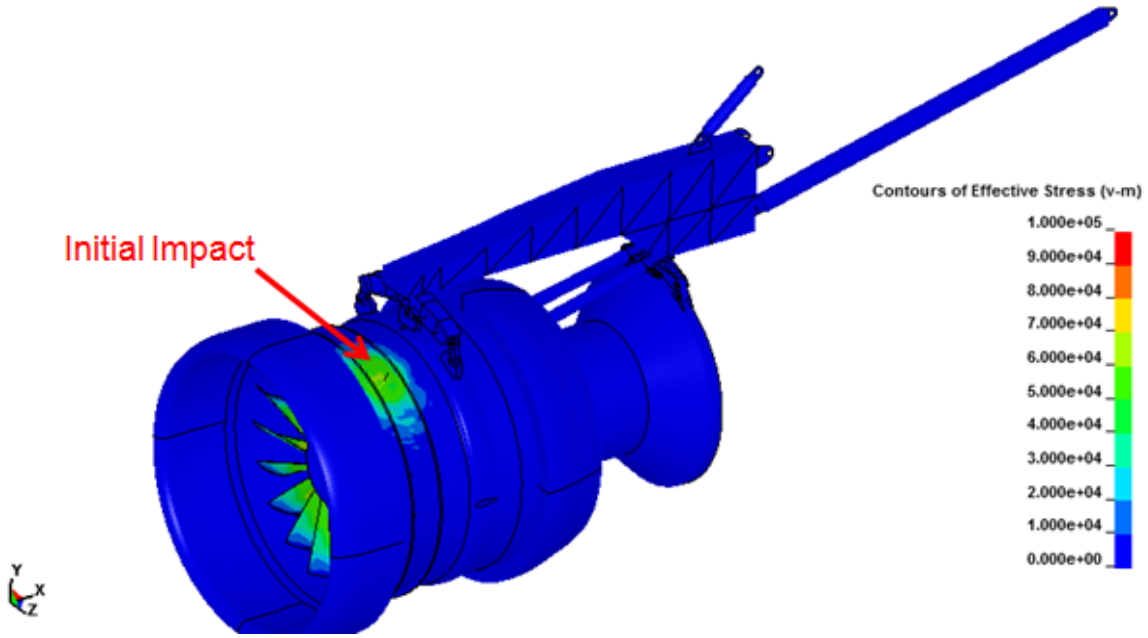

Figure 103. Containment Case Damage at 1.2 ms

The second damage zone is expansion around the first zone with creation of a bulge where the released blade's tip curls and buckles after hitting the containment case (see figure 104). The third damage zone is caused by the hammering impact of the released blade's root. This typically causes the most significant damage to the containment case (see figures 105 and 106).

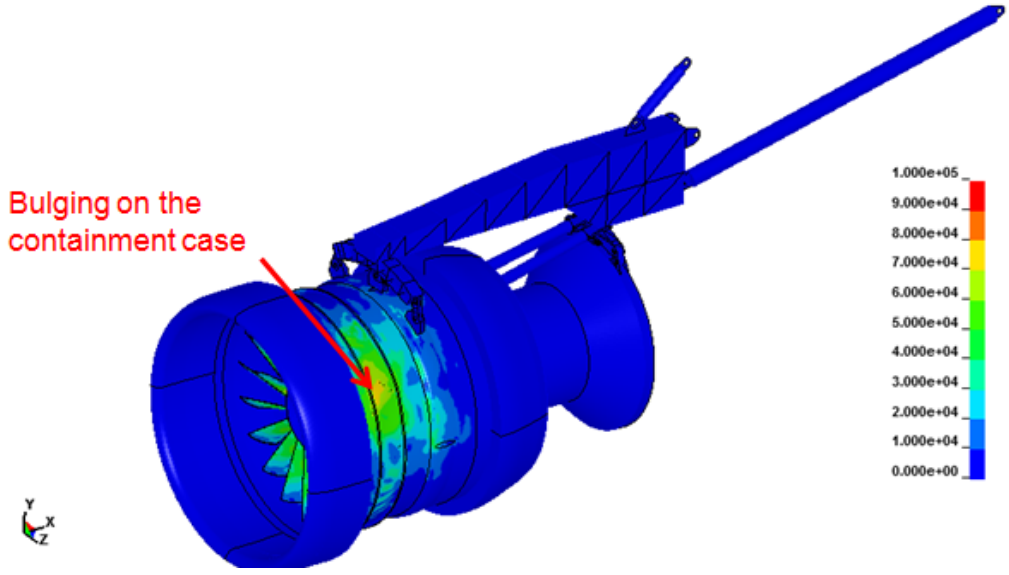

Figure 104. Containment Case Damage at 2.0 ms

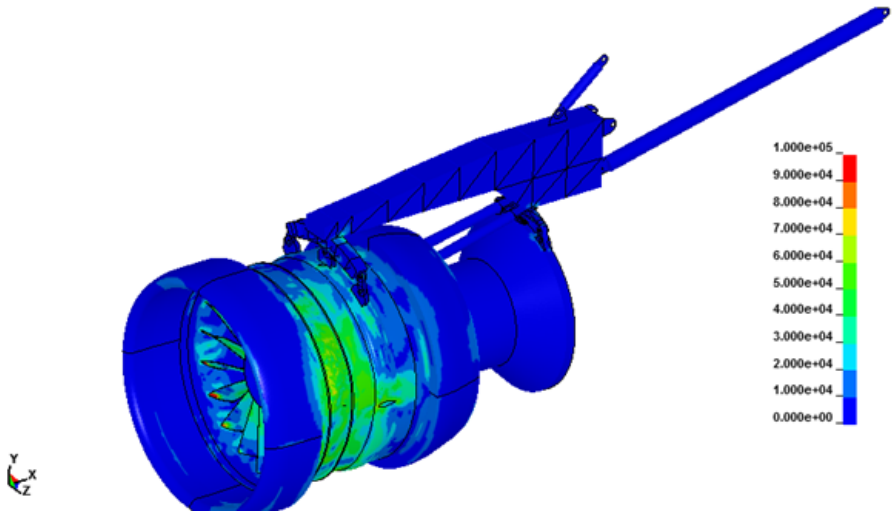

Figure 105. Stresses Scaled to Highlight Containment Case Damage at 3.5 ms

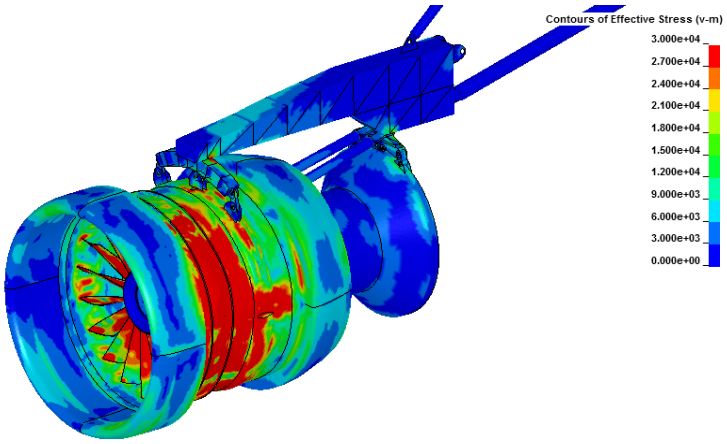

Figure 106. Stresses Scaled to Highlight Strut and Containment Case Damage at 3.5 ms

During the three damage phases described, the forward and aft mounts are also highly stressed as the FBO dynamic forces on the containment case and also through the fan shaft bearings are transmitted through the engine and installation (see figures 107 and 108).

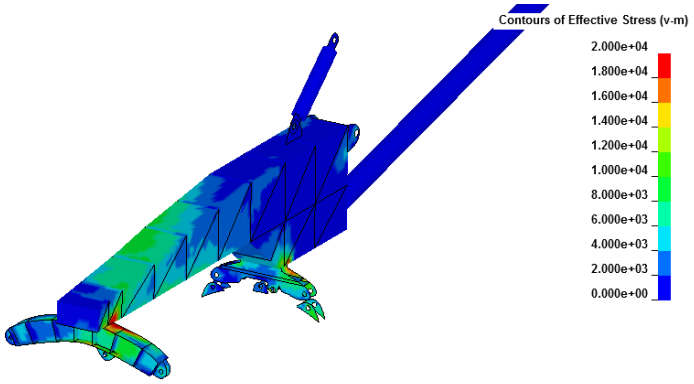

Figure 107. Strut, Forward, and Aft Mount Damage at 3.5 ms

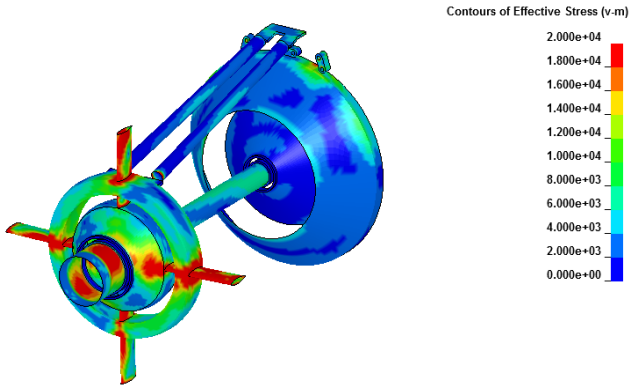

Figure 108. Fan Struts, Bearing Supports, and Fan Shaft Damage at 3.5 ms

5. CONCLUSIONS AND RECOMMENDATIONS

In phase 1 of this study, a three-blade generic fan rig model was constructed in the LS-DYNA explicit finite element code for simulating the initial blade release through blade containment phases of a fan blade-off (FBO) event. To ensure the LS-DYNA model was assembled correctly, independent checkout models were constructed in DYROBES and ANSYS. Comparison cases for shaft dynamics were run between LS-DYNA and DYROBES and for bladed fan disk dynamics between LS-DYNA and ANSYS. Parallel comparisons between ANSYS and DYROBES were run when the analysis capabilities overlapped. Construction and comparison of these independent models ensured that the LS-DYNA model was constructed accurately and contained dynamic characteristics consistent with what an engine manufacturer might use for preliminary design studies for assessing new fan blade and containment concepts.

The typical blade release event includes several distinct stages: blade release, impact of the release blade tip against the containment case, blade tip skating along the case (includes case and blade deformation), trail blade impact with the release blade, fragmentation of the release blade, impact of the blade root against the fan case, and tumbling of blade fragments. During an FBO event, the fan case experiences initial damage where the blade tip impacts the case and more

significant secondary damage where the blade root impacts the case. The fan blade typically fragments with the outer third (tip) of the blade traveling forward and the lower 2/3 of the blade (root) moving aft of the centerline of fan rotation. During the event, additional energy is introduced to the released blade when it is impacted by the trailing blade.

With the assumptions and simplifications incorporated in this model, it is capable of capturing the relevant physics of the initial blade-out event from release through demonstration of primary containment. Simulation results are consistent with industry-reported results of full-engine FBO and fan rig tests. Compared to FBO studies available in the literature [1], similar blade breakup patterns and containment case damage zones were also shown. Comparing damage zones on the fan containment case, it was determined that the case experienced higher effective plastic strains and plastic strain rates at the final root impact than at the initial tip impact location. In both impact zones, the outer surface of the containment case experienced a biaxial tension state of stress with a compression-shear state of stress state occurring at the inner surface.

The material failure model for the blade has a significant influence on blade deformation, fragmentation, and kinetic energy. To evaluate the effect of the material failure model on blade fragmentation, two material models are compared: rate-dependent Piecewise Linear Plasticity with constant plastic strain to failure and the Johnson-Cook damage model, in which plastic strain to failure is dependent on stress triaxiality and strain rate dependency. It was shown that both the constant plastic strain to failure and Johnson-Cook models require event-dependent tuning to produce similar results. It was also shown that both element size and the material failure model played critical roles in correctly predicting blade breakup. At least four elements through the thickness of the released blade were required to be able to accurately capture the blade breakup pattern. Both the Piecewise Linear Plasticity model, with constant effective plastic strain at failure, and the Johnson-Cook material model were evaluated in terms of blade breakup prediction capability. It was found that the failure strain value needed to be tuned based on mesh size, stress state, and strain rate experienced in the impact event when a constant effective plastic strain-at-failure model was used. Damage with the Johnson-Cook material model was based on a cumulative damage law in which effective plastic strain at failure is defined as a function of strain rate, stress state, and thermal softening. Blade breakup was also sensitive to in-plane element size when the Johnson-Cook material model was used with four elements through the thickness of the blade. Stress state at the main breakup zone of the released blade was evaluated and plain strain tension state was predicted for the initially failed elements at the tensional side of the plastically bent section. Based on these findings, it was concluded that a material failure model must be required to cover the effective plastic strain at failure in the plane strain tension state in order to be able to accurately predict blade breakup.

Fan blade-tip friction has a very important influence on accurate prediction of blade-tip and case-impact deformation, blade fragmentation, blade-tip sliding on the fan case, and the kinetic energy of fragments. Analysis results also show that friction affects blade fragment orientation and impact obliquity angle when fragments impact the case. These findings indicate that fan case damage may shift from nonperforation to local perforation at the initial-impact or root-impact locations as a function of friction. Therefore, when performing an FBO analysis, it is necessary

to address the sensitivity of the containment analysis to the blade-case interaction friction coefficient.

Two available sets of Johnson-Cook damage model parameters for AL2024—Lawrence Livermore National Laboratory (LLNL)-2 and LLNL-3—were compared to assess the influence of material model tuning on the ability to predict containment-case damage. It is known that the LLNL-2 set has a lower effective plastic strain at failure for biaxial and uniaxial tension, shear, and uniaxial compression when compared to the LLNL-3 set. Analysis results showed that, although the released blade was contained in all cases, the LLNL-2 set was able to predict local material failure on the fan casing, whereas no material failure was predicted with the LLNL-3 set. It was determined that failure in the biaxial tension and compression-shear states has to be covered with a single set of damage model parameters to be able to predict material failures in the inner and outer surfaces of the containment case in a typical FBO event. The two LLNL data sets predict different damage on the containment case and each set works for different failure modes if the failure modes depend on the obliquity of fragment, plate thickness, and fragment velocity. The current damage material law in Johnson-Cook does not allow adjusting material model damage parameters dynamically; therefore, it is concluded that development of a new material law that can meet the needs for change and transition in the failure mode is necessary [11].

A new material model, MAT224, has been developed to cover the transition of failure modes in different stress states by considering the stress triaxiality and lode angle parameters for each element at each time step. It is recommended that additional work be performed to assess how MAT224 predicts failure modes for the containment analysis cases presented in this report and that a follow-on comparison between MAT224 and the Johnson-Cook material models be conducted.

In phase 2 of this effort, a full-fan rig model was developed by adding appropriate flexible structure to the phase 1 model. These additions included the fan frame connecting the fan case to the core case; a core case; front and rear mounts; strut; and a fully bladed fan rotor. The resulting model is capable of representing the full-bladed fan rotor interaction with the containment structure. Blade tip rubbing and post-containment interaction of the engine system were simulated using the full-fan rig model. This model is able to identify FBO initial and post-containment force time histories at the bearings, key structural joints, mount links, and strut ground locations using cross-section forces cards in LS-DYNA. For the next stage of the rig model development and verification, it is recommended that a rub strip model be added to the containment case so that damage to the rub strip material and its effects on damping and structural response of the system can be evaluated. Different blade-release clock positions can be analyzed and the resulting force flow and system responses compared to identify worst-case conditions. Running multiple release angles is important because it allows the analyst to determine which load case is critical for each component without having to run multiple tests. This model does not have sufficient detail to analyze bolt and prestress (bolt torque) effects; however, it can be used to predict the free-body interface forces at joints, and these forces can then be used to drive a more detailed joint model to assess bolts and prestress effects.

Finally, although not attempted in this study, the model is capable of modeling sustained rubs (e.g., high imbalance, thermal closure, subsynchronous excitation, or other drivers) for which the frequency of rubbing has its own important impact on system dynamic response. This can be studied for the effect of sustained rub vibration-driven fatigue.

6. REFERENCES

1. Sinha, S.K. and Dorbala, S., "Dynamic Loads in the Fan Containment Structure of a Turbofan Engine," *Journal of Aerospace Engineering*, Vol. 22, No. 3, 2009, pp. 260–269.

2. Heidari, M., Carlson, L.D., Sinha, S., and Sadeghi, R., "An Efficient Multi-Disciplinary Simulation of Engine Fan-Blade Out Event Using MD Nastran,"Paper No. AIAA 2008–2333, *49th AIAA/ASME/ASCE/AHS/ASC Structures, Structural Dynamics and Materials Conference*, April 7–10, 2008.

3. Shmotin, Y.N., Gabov, D.V., Ryabov, A.A., Kukanov, S.S., and Rechkin, V.N., "Numerical Analysis of Aircraft Engine Fan Blade-Out," Paper No. AIAA 2006–4620, *42nd AIAA/ASME/SAE/ASEE Joint Propulsion Conference*, July 9–12, 2006.

4. Cosme, N., Chevrolet, J., Bonini, J., and Peseux, B., "Prediction of Engine Loads and Damages Due to Fan Blade Off Event," Paper No. AIAA 2022–1666, *43rd AIAA/ASME/ASCE/AHS/ASC Structures, Structural Dynamics and Materials Conference*, April 22–25, 2002.

5. Carney, K.S., Lawrence, C., and Carney, D.V., "Aircraft Engine Blade-Out Dynamics," *7th International LS-DYNA Users Conference*, 2002.

6. Lesuer, D., "Experimental Investigation of Material Models for Ti-6Al-4V and 2024-T3," FAA Report DOT/FAA/AR-00/25, September 2000.

7. Kay, G., "Failure Modeling of Titanium 6Al-4V and Aluminum 2024–T3 With the Johnson-Cook Material Model," FAA Report DOT/FAA/AR-03/57, September 2003.

8. Buyuk, M., Loikkanen, M.J., and Kan, C.D., "Explicit Finite Element Analysis of Aluminum 2024-T3/T351 Aluminum Material Under Impact Loading for Airplane Engine Containment and Fragment Shielding," FAA Report DOT/FAA/AR-08/36, September 2008.

9. Goldsmith, W., "Review: Non-Ideal Projectile Impact on Targets," *International Journal of Impact Engineering*, Vol. 22, 1999, pp. 95–395.

10. Sarkar, S., and Atluri, S.N., "Effects of Multiple Blade Interaction on the Containment of Blade Fragments During Rotor Failure," *Finite Element Analysis and Design*, Vol.23 (2), 1996, pp. 211–233.

11. Hagg, A.C. and Sankey, G.O., "The Containment of Disk Bust Fragments by Cylindrical Shells," *Journal of Engineering for Power*, ASME 96, 1974, pp. 114–123.

12. Lundin, S.J., and Mueller, R.B, "Advanced Aircraft Materials, Engine Debris Penetration Testing," FAA Report DOT/FAA/AR-03/37, 2003.

13. Teng, X. and Wierzbicki, T., "Gouging and Fracture of Engine Containment Structure Under Fragment Impact," *Journal of Aerospace Engineering*, Vol. 21, No. 3, July 2008, pp. 174–186.

14. Bridgeman, P.W., "Studies in Large Plastic Flow and Fracture," Harvard University Press, Cambridge, 1964.

15. Johnson, G.R., and Cook, W.H., "Fracture Characteristics of Three Metals Subjected to Various Strains, Strain Rates, Temperatures and Pressures," *Engineering Fracture Mechanics*, Vol. 21, 1985, pp. 31–48.

16. Wierzbicki, T., Bao, Y., and Bai, Y., "A New Experimental Technique for Constructing a Fracture Envelope of Metals Under Multi-Axial Loading" *Proceedings of the 2005 SEM Annual Conference and Exposition on Experimental and Applied Mechanics*, 2005.